Investigation of surface reactions by means of scanning probe techniques and electron spectroscopies

Zsolt Majzik

A Thesis submitted for the degree of Doctor of Philosophy

Supervisor: Prof. Dr. András Berkó and Prof. Dr. Vladimír Cháb

Doctoral School of Chemistry

Department of Physical Chemistry and Materials Science
Faculty of Science and Informatics
University of Szeged
Szeged
2012

Abbreviations

AES	**A**uger **E**lectron **S**pectroscopy
AFM	**A**tomic **F**orce **M**icroscopy
ARUPS	**A**ngle **R**esolved **U**ltraviolet **P**hotoelectron **S**pectroscopy
DAS	**D**imer-**A**datom-**S**tacking fault
DFT	**D**ensity **F**unctional **T**heory
DOS	**D**ensity **o**f **S**tates
ESCA	**E**lectron **S**pectroscopy for **C**hemical **A**nalyses
HOMO	**H**ighest **O**ccupied **M**olecular **O**rbital
HREELS	**H**igh **R**esolution **E**lectron **E**nergy **L**oss **S**pectroscopy
LUMO	**L**owest **U**noccupied **M**olecular **O**rbital
PES	**P**hoto**E**lectron **S**pectroscopy
PDOS	**P**rojected **D**ensity **o**f **S**tates
SEM	**S**canning **E**lectron **M**icroscope
SFM	**S**canning **F**orce **M**icroscopy
SMSI	**S**trong **M**etal-**S**upport **I**nteraction
SPM	**S**canning **P**robe **M**icroscopy
SRPES	**S**ynchrotron **R**adiation **P**hotoelectron **S**pectroscopy
STM	**S**canning **T**unneling **M**icroscopy
SMSI	**S**trong **M**etal-**S**upport **I**nteraction
TPD	**T**emperature-**P**rogrammed **D**esorption
TDS	**T**ermal-**D**esorption **S**ectroscopy
UHV	**U**ltra-**H**igh **V**acuum
UPS	**U**ltraviolet **P**hotoelectron **S**pectroscopy

Acknowledgements

In the past five years I performed my Ph.D. work as a student of two marvelous research groups: *a*) Reaction Kinetics and Surface Chemistry Research Group of the Hungarian Academy of Sciences at the University of Szeged and *b*) Institute of Physics, the Academy of Sciences of the Czech Republic, Prague. It is a pleasure to express my gratitude to Prof. Dr. András Erdőhelyi and Prof. Dr. János Kiss and to those who made this thesis possible and to thank those who gave support during the course of my studies.

First of all, I would like to thank my two supervisors Prof. Dr. András Berkó and Dr. Vladimír Cháb, for providing excellent support, inspiration and guidance throughout my PhD studies. Even though Dr. Pavel Jelínek was not officially my supervisor, his time and his extremely vulnerable comments and suggestions are also what have made this thesis possible. The senior scientists and post-docs with whom I have worked on several projects have additionally served as guides for me. The willingness of Dr. Martin Švec, Dr. Martin Setvín and Martin Vondraček to always help out in the lab and synchrotron is tremendously acknowledged. I am grateful to Dr. László Deák and Dr. László Óvári for the fruitful discussions and for their scientific advises. Dr. Pingo Mutombo and Dr. Martin Ondráček provided excellent support on computational calculations and they made valuable comments from the theoretical perspectives. I greatly appreciate the help of Dr. Arnold Farkas and Dr. Tamás Bánsági during my measurements. Lastly, I heartily value the help throughout my Ph.D. journey and friendship of Balázs Nándor and Dr. Cesar Pascual Gonzalez.

I have throughout my Ph.D. studies also collaborated with people outside of the two institutions mentioned above. It is an honor for me to have been able to spend weeks in the laboratory of Prof. Dr. Franz Gießibl at the University of Regensburg, Germany. Learning from the father of the qPlus technique and from his excellent colleagues provided me better understanding of non-contact atomic force microscopy (nc-AFM) and inspiration. I owe my deepest gratitude to Prof. Dr. Seizo Morita at Osaka University, Japan to let me stay couple weeks with his group that is undoubtedly one of the best research group within the field of nc-AFM. It was my great pleasure to work with Prof. Dr. Alastair B. McLean from Queen's University, Kingston, Ontario, Canada and with his students: Dr. Jay Weymouth (who is now a postdoc at the University of Regensburg) and Benedict Drevniok. I am thankful for the very good collaboration with Dr. Wojciech Kamiński at University of Wroczław, Poland, who made an excellent theoretical support during our measurements. I would like to show my gratitude to Prof. Dr. Bruno Domenichini and to Dr. Mikhail Petukhov at University of Bourgogne, Dijon, France for making it possible that I

could stay and perform some experiments in their laboratory. Finally, I am grateful to Kevin C. Prince and to his team at the Elettra synchrotron, Trieste, Italy for their time and effort to make our progresses possible at the Material Science beamline.

Last but not the least, this thesis would not be possible without endless support from my parents, to whom I dedicate this thesis. Also thanks to Olasz Mónika who is always beside me at all times as a part of my soul.

List of publications

Publications relevant to this thesis:

i. Z. Majzik, N. Balázs, and A. Berkó. Ordered SMSI decoration layer on Rh nanoparticles grown on TiO_2(1 1 0) surface. *Journal of Physical Chemistry C*, 115:9535–9544, 2011, IF: 4.805.

ii. Z. Majzik, N. Balázs, and A. Berkó. Thermally activated reconstruction of TiO_2(1 1 0)–1×1 surface in the presence of potassium: an STM study. *Catalysis Today*, 181:89–94, 2012, IF:3.407.

iii. Z. Majzik, W. Kamiński, A. J. Weymouth, M. Vondráček, V. Zobač, M. Švec, A. Berkó, A. B. McLean, K. C. Prince, P. Jelinek, and V. Cháb. An investigation of ethylene attachment to Si(1 1 1)–7×7 in the restatom-adatom bridging geometry: electronic and vibrational properties. *Journal of Physical Chemistry C*, 115:21791–21799, 2011, IF:4.805.

iv. Z. Majzik, M. Setvín, A. Bettac, A. Feltz, V. Cháb, and P. Jelinek. Simultaneous current, force and dissipation measurements on the Si(1 1 1)–7×7 surface with an optimized qPlus AFM/STM technique. *Beilstein Journal of Nanotechnology*, 3:249–259, 2012, IF:0.789.

Other publications:

i. J. Berger, M. Švec, M. Muller, M. Ledinský, A. Fejfar, P. Jelínek, and Z. Majzik. Characterization of the mechanical properties of qPlus sensor using different methods. *Beilstein Journal of Nanotechnology*, 2012, IF:0.789 (Submitted).

ii. A. Berkó, Z. Majzik, and A. Kiss. Low temperature CO oxidation on differently prepared TiO_2(1 1 0) supported Au catalysts. *Journal of Physics: Conference Series*, 61:110, 2007, IF: Not rated.

iii. Z. Majzik, N. Balázs, L. Robin, M. Petukhov, B. Domenichini, S. Bourgeois, and A. Berkó. Tunneling induced decomposition of $Mo(CO)_6$ onto TiO_2(1 1 0) surface. *Vaccum*, 86:623–626, 2012, IF:1.317.

iv. P. Mutombo, N. Balázs, Z. Majzik, A. Berkó, and V. Cháb. Theoretical study of the adsorption of rhodium on a TiO_2(1 1 0)–1×1 surface. *Applied Surface Science*, 258:4478–4482, 2012, IF:2.103.

v. L. Óvári, A. Berkó, N. Balázs, Z. Majzik, and J. Kiss. Formation of Au-Rh core-shell nanoparticles on TiO_2(1 1 0) surface studied by STM and LEIS. *Langmuir*, 26:2167–2175, 2010, IF:4.268.

vi. L. Ovari, L. Bugyi, Z. Majzik, A. Berkó, and J. Kiss. Surface Structure and Composition of Au-Rh Bimetallic Nanoclusters on TiO_2(1 1 0): A LEIS and STM Study. *Journal of Physical Chemistry C*, 112:18011–18016, 2008, IF:3.396.

vii. M. Setvín, J. Javorský, Z. Majzik, P. Sobotík, P. Kocán, and I. Ošt'ádal. Competition between thermally activated and tip-induced hopping of indium atoms on Si(1 0 0). *Physical Review B*, 85:081403, 2012, IF:3.691.

viii. M. Setvin, P. Mutombo, M. Ondracek, Z. Majzik, M. Švec, V. Cháb, I. Ost'adal, P. Sobotik, and P. Jelinek. Chemical identification of single atoms in heterogeneous III-IV chains on Si(1 0 0) surface by means of NC-AFM and DFT calculations. *ACS Nano*, 6:6969–6976, 2012, IF:10.774.

Presentations at international conferences

1. Z. Majzik, A. J. Weymouth, M. Vondráček, M. Švec, K. C. Prince, A. B. McLean and V. Cháb: The thermal conversion of ethylene/Si(1 1 1)–7×7 → SiC studied with photoemission and STM. **ECOSS 26**, Parma, Italy – 2009, *Oral*

2. M. Setvín, Z. Majzik, V. Cháb, P. Jelínek: Simultaneous STM and NC-AFM measurements on silicon surfaces. **NC-AFM 13**, Kanazawa, Japan – 2010, *Poster*

3. Z. Majzik, N. Balázs and A. Berkó: Atomically resolved STM detection and tunneling current spectroscopy of wagon-wheel-like decoration layer on Rh nanocrystallites supported on TiO_2(1 1 0). **IVC 18, ICN+T**, Beijing, China – 2010, *Poster*

4. Z. Majzik, W. Kaminski, M. Vondráček, M. Švec, A. Berkó, V. Cháb, P. Jelínek: Discrimination of single ethylene molecules adsorbed on the Si(1 1 1)–7×7 surface by means of Atomic Force Microscopy. **ECOSS 28**, Wrocław, Poland – 2011, *Oral*

5. Z. Majzik, W. Kaminski, M. Vondráček, V. Cháb, P. Jelínek: Experimental and theoretical investigation of the adsorption of ethylene on Si(1 1 1)–7×7 surface. **AAFMT**, Karsruhe, Germany – 2011, *Poster*

6. Z. Majzik, W. Kaminski, M. Vondráček, V. Cháb, P. Jelínek: Experimental and theoretical investigation of the adsorption of ethylene on Si(1 1 1)–7×7 surface. **ICFSI 13**, Prague, Czech Republic – 2011, *Oral*

7. Z. Majzik, W. Kaminski, B. Drevniok, A.B. McLean, V. Cháb, P. Jelínek: Molecular recognition of single molecules adsorbed on the Si(1 1 1)–7×7 surface by means of NC-AFM. **NC-AFM 14**, Lindau, Germany – 2011, *Oral*

8. M. R. Tchalala, M. Švec, Z. Majzik, H. Enriquez, A. Kara, A. Mayne, G. Dujardin, P. Jelínek, H. Oughaddou: Simultaneous AFM/STM measurements of silicene grown on metal surfaces. **NC-AFM 15**,Č eský Krumlov, Czech Republic – 2012, *Poster*

9. Z. Majzik, M. Ondráček, J. Berger and P. Jelínek: Relation between the apparent height barrier, the chemical force and the local contact potential difference in atomic scale. **NC-AFM 15**,Č eský Krumlov, Czech Republic – 2012, *Oral*

10. Z. Majzik, O. Krejci, W. Kaminski, B. Drevniok, M. Setvín, A.B. McLean, V. Cháb, P. Jelínek: Molecular identification of surface adsorbates using NC-AFM. **ICN+T**, Paris, France – 2012, *Oral*

11. Z. Majzik, M. Ondráček, J. Berger and P. Jelínek: Understanding the influence of the tunneling current and the chemical force on the contrast formation in KP-AFM. **AVS 59**, Tampa, FL, USA – 2012, *Oral*

Contents

"For if we allow that human life is always guided by reason, we destroy the premise that life is possible at all."

Leo Tolstoy, War and Peace

1 Introduction

The development of surface science as a specific field of chemistry and physics had a strong connection with the rapid and versatile evolution of heterogeneous catalysis [1]. This latter field served as one of the most important cornerstones of modern industry. The strategic steps in the history of the surface science were unequivocally accompanied by introducing new experimental techniques that can characterize the atomic and molecular composition of adsorbate/surface systems. Furthermore, the discovery and rapid spread of scanning probe microscopies (SPM), which allowed real-space atomically resolved imaging of surfaces and made atomic and molecular recognition possible, had an extraordinary impact on our level of understanding of surface chemistry [2, 3].
For a proper usage, these revolutionarily new techniques required ultrahigh vacuum (UHV) systems in which the base pressure falls even below 10^{-8} Pa. SPM operation under UHV conditions opened up the possibility to study atomically clean surfaces and to comprehend isolated surface processes such as phase transitions, single molecule adsorption and manipulation, growth and nucleation of nanoclusters. The strong enthusiasm about new surface phenomena triggered the start of producing and studying more and more two-dimensional (2D) systems. These model materials are important not just from catalytic point of view but also for development of state-of-the-art nanoelectronic devices.

In this work the main interest is directed towards the investigation of the adsorption of metals and molecules on oxide and semiconductor surfaces. Among the huge variety of suitable oxide supports, as a model material, $TiO_2(1\,1\,0)$ was chosen to investigate in detail the adsorption of metals. This topic derives from the fact that the metal/TiO_2 systems have already made, and will

continue to have, an impact on the development of catalysts of high performance, moreover, that of solar and hydrogen fuel cell fabrication [4].

By deposition of potassium and investigation of thermal treatments, we characterized the morphological effects of a typical alkali additive used widely in the heterogeneous catalysis. Interesting results will be presented in connection of decorated/encapsulated Rh nanoparticles supported on $TiO_2(1\,1\,0)$ surface by atomic scale scanning tunneling microscopy (STM) studies. In this latter topic, there is an internationally strong activity for the better understanding of the formation of oxide ultrathin films on noble metal nanocrystallites supported on reducible oxides (the phenomenon called decoration and/or strong metal-support interaction, SMSI) [4, 5].

The SiC surface has a strong technological significance in production of electronic devices and catalysts [6, 7]. Ethylene can act as a source of carbon for the production of SiC. In accordance to this, by a complex surface investigation (involving many techniques) it will be shown how the scanning atom probe techniques can contribute to the elucidation of the proper adsorption mechanism of C_2H_4 molecule on $Si(1\,1\,1)$–7×7 substrate. In addition, it will be made obvious that in contrast with STM, AFM can successfully be used to identify the adsorbed molecule on the surface (molecular identification). While SPM technologies can provide crucial information about surface structure, they provide only limited information about the chemical composition, bonding configuration of the surface/adsorbate system. In order to have more complete picture about surface processes, electron spectroscopies were also utilized.

Opening a new horizon for surface investigations, the recent development of the qPlus AFM technique enabled simultaneous acquisition of interaction forces and tunneling current [8]. However, this setup requires special attention to avoid so-called cross-talk effect between the current signal and the deflection channels. The basics of the cross-talk phenomena will be introduced in details and several methods for its elimination will be also discussed.

"Human science fragments everything in order to understand it, kills everything in order to examine it."

Leo Tolstoy, War and Peace

2

Background of applied experimental techniques

2.1 Scanning Probe Microscopy

2.1.1 Scanning Tunneling Microscopy

Operation

The scanning tunneling microscope (STM) was invented by Binning and Rohrer. Additionally, Ch. Gerber, and E. Weibel contributed to the implementation of the technique [9–11]. The basic operation principle of STM is actually very simple and Figure 2.1 shows its mandatory elements. It consists a probe tip, usually made of W of Pt-Ir alloy, attached to piezoelectric transducers (perpendicularly mounted in x, y and z direction) or a piezoelectric tube scanner that can perform the same operation. An applied voltage to one of these transducers causes expansion or contraction in lateral direction due to piezo electric effect. The xy scanning is maintained by applying a sawtooth voltage on the x and a voltage ramp on the y piezo [12].

With a precision corse positioner and with the help of the z piezo, the tip can be approached toward to the sample (as close as a few Å). Nowadays piezo motors are commonly used as a corse drive but even a simple micro screw can perform this operation.

If the tip-sample distance is sufficiently low, the electron wave-functions of the tip-apex atom overlap with the electron wavefunctions in the sample surface, a finite tunneling conductance is generated. Due to the applied bias voltage between the tip and the sample, tunneling current is generated. By convention for the polarity of the bias voltage, the tip is virtually grounded and

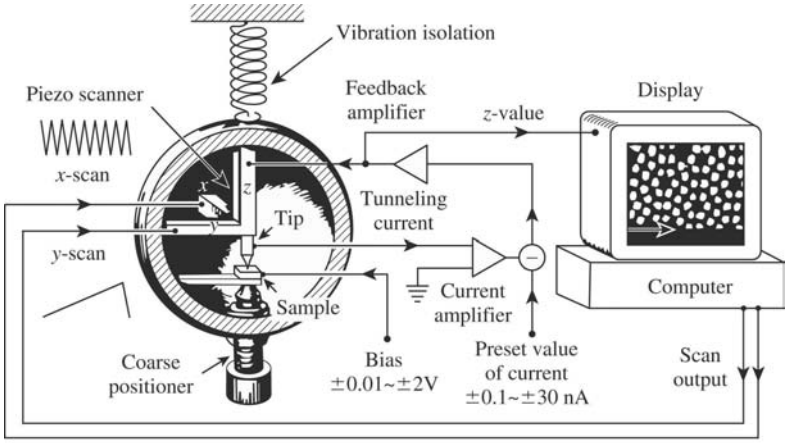

Figure 2.1: Basic operation of the scanning tunneling microscope. With the corse positioner the tip can be brought in tho the tunneling regime. The applied bias voltage between the tip and the sample induce tunneling current. The computer generates the scanning signal for the piezo transducers. The constant tunneling current is maintained by the feedback system of the z piezo. The change in the z voltage represents the imaging signal. (Image is taken from ref. [12])

the bias voltage V is the sample voltage [12]. In the case of a positive voltage, the electrons are tunneling from the occupied states of the tip into the empty states of the sample, therefore the produced image is called an empty state image. In the case of reversed polarity, electrons are tunneling from the occupied (filled) states of the sample to the empty states of the tip, this kind of images are filled state images.

The tunneling current is fed into a current to voltage converter (current amplifier or IVC) and it is converted to voltage that is compared with the reference value. Due to the very low probability of tunneling, usually the current is in the range of nA, therefore the conversion factor needs to be around 1 nA/V. The difference voltage between the actual tunneling current and the reference value is amplified to z piezo. The current amplifier is also an inverting amplifier (shift the phase of the input signal by 180°). This inverting amplifier forms a negative feedback: if the absolute value of the tunneling current is larger than the reference value, the voltage applied to the z piezo tends to withdraw the tip from the sample surface, and *vice versa*. Therefore with some error raising from the speed of the feedback system, the chosen set point for the tunneling current is kept constant. As the tip scans over the xy plane the tunneling current is maintained to be constant and the changes in the z position is recorded by the computer as a topographic image of the surface. An image can be obtained also by keeping the tip sample position constant (needs atomically flat surfaces) and the computer records the tunneling current over the xy plane, as a result a current image is recorded. Properties of the tunneling current amplifier will be discussed in more details in Section 4.1.2.

In order to obtain stable atomic resolution, a good vibration isolation is needed. The frist STM was designed with superconducting levitation of the tunneling unit for vibration isolation, which made the construction to be very complicated and the operation needed always expensive liquid He [9, 10]. In later designs, stack of metal plates separated by viton (a UHV-compatible rubber spacer) or a double-stage spring system with eddy-current damping were used and these isolation systems till serve well for todays microscopes [13]. An eddy-current damper consists a copper block under the influence of magnetic field of a permanent magnet. The motion of the magnet and the copper block in one direction causes an acting force in the opposite direction, thus the vibration (motion) is damped. This kind of isolation systems are superior to any other systems but they are large. On one hand, the benefit of the viton system is that, the instrument can be relatively small (pocket size STMs), on the other hand the resonant frequency of the system is around 10 Hz, hence extra isolation is needed (optical table) to filter out low frequencies (below 50 Hz) [14].

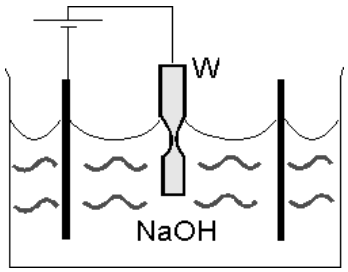

cathode	$6\,H_2O + 6e^- \longrightarrow 3\,H_2(g) + 6\,OH^-$	SRP = − 2.48 V
anode	$W(s) + 8\,OH^- \longrightarrow WO_4^{2-} + 4\,H_2O + 6e^-$	SOP = + 1.05 V
	$W(s) + 2\,OH^- + 2\,H_2O \longrightarrow WO_4^{2-} + 4\,H_2O + 3\,H_2(g)$	E° = − 1.43 V

Figure 2.2: Schematic view of the tip etching process and undergoing electrochemical reactions

Essentially for achieving atomic resolution the scanning probe must be very sharp. Very sharp tungsten tip can be made by simply electrochemical etching. In this process, the tungsten wire usually immersed to the solution of sodium/potassium hydroxide (the concentration is usually somewhere between 1 or 2 mol/dm^3). Then a potential is applied between the tip and the counter electrode while the etching current is monitored. In principle any voltage value can be used between 4 and 12 V (or for some applications even higher to gain extra reaction speed). Typically the minimum current can be set from which the etching process is terminated. The set point is adjusted just below the current, where the bottom part of the wire drops down (see Figure 2.2).

As it was already mentioned before, Pt/Ir alloys are also popular tip materials. Iridium is used to provide stiffness. Owing to being inert, Pt/Ir tips are valuable especially for ambient/liquid STM applications and also for UHV-STM. Unfortunately, it is rather difficult to produce suitably sharp tips. On one hand, in most of the cases hazardous acids (like concentrated H_2SO_4) are used for post polishing and sharpening the tip that is etched in the solution of calcium or potassium chloride. On the other hand, making with appropriate safety considerations, tip with an apex radius of only tens of Å can be routinely prepared [15]. Also one can note that due to the low reactivity of Pt/Ir compared to tungsten, these tips can provide better and more stable resolution. However, tungsten tips are more uniformly shaped and may perform better on corrugated surfaces.

$$k = \frac{AE}{l} \tag{2.1}$$

During the preparation of an STM tip several consideration must be made. The shape of the tip plays very important rule not just for getting atomic resolution but also for obtaining stable scanning. Although, the tungsten has a Young's modulus of 400 GPa, by considering equation 2.1 for the axial stiffness (where k is the stiffness, A is the cross section, E is the Young's modulus and l is the length of the tip), it can be easily seen that a long and narrow tip can have relatively small stiffness hence it can suffer from vibrations [16]. There are several parameters affecting the etching process: the cell potential, the shape of the meniscus, the concentration of electrolyte and the length of W wire immersed to the solution. Finding the optimal attaching parameters are the first key to achieve astonishing results.

2.1.2 Atomic Force Microscopy

The invention of the scanning tunneling microscope (STM) was evidently one of the most admirable step among developments of microscopes. On the other hand, the working mechanism of STM is based on electrical conductance which is strongly limiting the list of observable surfaces to electrically conductive materials. Insulators can not be measured by this technique, apart from very thin insulating layers, where the tunneling through the layer can produce significantly large current (to be detected by the current amplifier). For bulk insulators the equivalent method had to be found.

After having successfully imaged the Si(1 1 1)–7×7 surface on atomic scale, the attention rapidly moved to various surfaces such as different silicon facets, metal surfaces and graphite. The latter

one took special attention because of being inert, therefore it was possible to perform measurements on it without the necessity of having ultra high vacuum conditions. Atomically clean graphite surface can be obtained in air by simply removing the upper most layer with using a scotch tape (nobody was interested in the remaining graphite part on the tape at that time [17]). The graphite surface produced surprisingly giant corrugation among measurements with scanning tunneling microscope and was explained by elastic deformations induced by the interatomic forces between tip and surface [18]. Probably this was the first observation of interaction forces that are used for imaging in the atomic force microscope (AFM).

The concept of AFM is raising from the idea that a probe (nanofinger) can sense individual atoms by interaction forces (see Figure 2.3). The working phenomena is like a vinyl player where a sharp tip (usually diamond) is following the structure of the recorded music. The first microscope was built by G. Binnig, C.F. Quate and C. Gerber in 1986 [19]. That consisted a soft cantilever (spring) with a tip on it that was brought close to the surface (into gentle contact) and scanned over in the same way as in the case of an STM. The small deflection caused by tip sample forces of the spring was monitored by an STM tip approached to the lever. The lateral resolution of the first prototype was about 30 Å and the vertical was already less than 1 Å [19]. In later designs the complicated deflection measurement with an STM tip was replaced by an optical beam deflection [20] system or by an optical interferometer [21].

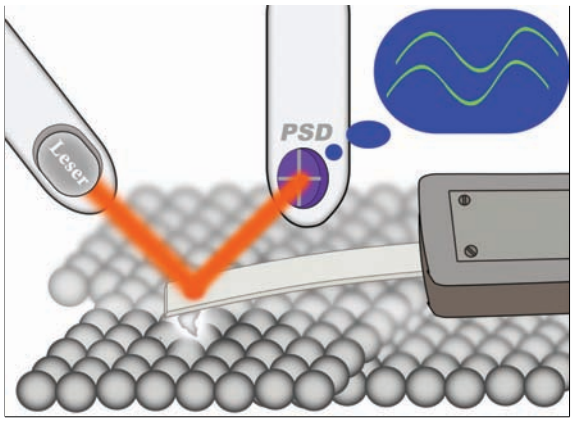

Figure 2.3: Basic configuration of an atomic force microscope: the interaction forces lead to the defection of the cantilever that is optically monitored.

The main drawback of the previously mentioned contact mode operation is the presence of strong tip-sample interaction, which makes scanning destructive for both tip and sample and reliable interpretation of the atomic contrast becomes very difficult. To overcome of these limitations frequency modulation non-contact (NC-)AFM technique was introduced by Albrecht and

coworkers [22]. Beside FM modulation there is an other type of scanning mode, called amplitude modulation (AM), however the present discussion will be limited to FM because only FM mode was used for experimental scans in this work. By applying this method Giessibl demonstrated the possibility of achieving true atomic resolution on the prototypical Si(111)–7x7 surface [23]. Among others, this seminal work initiated fast progressing on FM-AFM technique in the last decade [24, 25].

Frequency Modulation (FM-)AFM

In FM-AFM mode, a sensor (in most cantilever) brought to oscillation with a constant oscillation amplitude a. The cantilever has f_0 resonant frequency, k stiffness and it has m^* effective mass (that includes the tip as well). Decreasing the tip-sample distance $k_{ts} = -\partial F_{ts}/\partial z$ force gradient appears between the tip and the sample. As a result of the acting force(s) the value of f_o is changed by Δf. From this we can write:

$$\begin{aligned} \Delta f &= f - f_0 \\ f &= f_0 - \Delta f \\ f &= \frac{1}{2\pi}\sqrt{\frac{k + k_{ts}}{m^*}} \\ \Delta f &= \frac{f_0}{2k} k_{ts}. \end{aligned} \tag{2.2}$$

The force gradient k_{ts} is not constant during the oscillation cycle and the relationship between the frequency shift and force becomes less trivial. The relationship was first calculated by Giessibl using Hamilton–Jacobi perturbation theory [26]. The resulting equation is

$$\Delta f(z_b) = \frac{f_0^2}{ka} \int_0^{1/f_0} F_{ts}(z_b + a\cos(2\pi f_0 t))\cos(2\pi f_0 t)\mathrm{d}t \tag{2.3}$$

where z_b is the vertical base position of the cantilever [27]. In experiment, the frequency shift is recorded as a function of the tip–sample separation and it is quite convenient to have a direct method for calculating the interaction force directly from the measured frequency shifts ($\Delta f(z)$).

This needs the inversion of Equation 2.3. One algorithm was shown by Giessibl [27]. That is

$$\begin{pmatrix} \Delta f_1 \\ \Delta f_2 \\ \dots \\ \Delta f_N \end{pmatrix} = \begin{pmatrix} w'_{11} & 0 & \dots & 0 \\ w'_{21} & w'_{22} & \dots & 0 \\ \dots & \dots & \dots & \dots \\ w'_{N1} & w'_{N2} & \dots & w'_{NN} \end{pmatrix} \begin{pmatrix} F_{ts1} \\ F_{ts2} \\ \dots \\ F_{tsN} \end{pmatrix}, \tag{2.4}$$

here the elements of the $W' = (w_{ij})$ matrix needs to be pre-calculated. That can be done as

$$w'_{if} = \begin{cases} f_0 \frac{1}{2k} \frac{2}{\pi A} \int_{1-[2(i-j+1)]/[(2\alpha+1)]}^{1-[2(i-j)]/[(2\alpha+1)]} \frac{\tau}{\sqrt{1-\tau^2}} \mathrm{d}\tau & \text{for } 0 \leq i-j \leq 2\alpha, \\ 0 & \text{else} \end{cases} \tag{2.5}$$

where α is an integer expressing the amplitude a in terms of the z step with Δ ($\alpha = \mathrm{round}(a/\Delta)$ and $F_{tsi} = F_{ts}(z_{i+\alpha})$ [27]. In order to get the the conversion from frequency shift to interaction force the inverse of the matrix W' needs to be calculated ($W'^{-1} = (w_{ij})^{-1}$) and

$$\begin{pmatrix} F_{ts1} \\ F_{ts2} \\ \dots \\ F_{tsN} \end{pmatrix} = \begin{pmatrix} w'^{-1}_{11} & 0 & \dots & 0 \\ w'^{-1}_{21} & w'^{-1}_{22} & \dots & 0 \\ \dots & \dots & \dots & \dots \\ w'^{-1}_{N1} & w'^{-1}_{N2} & \dots & w'^{-1}_{NN} \end{pmatrix} \begin{pmatrix} \Delta f_1 \\ \Delta f_2 \\ \dots \\ \Delta f_N \end{pmatrix}. \tag{2.6}$$

This inversion can be easily performed with todays computers even for very large datasets.

Shortly after the method shown above had been introduced, a second solution for the inversion of Equation 2.3 was presented by Sader et. al. [28] and this method is well spread today among the AFM community. The equation is

$$F(z) = 2k \int_0^\infty \left(1 + \frac{a^{1/2}}{8\sqrt{\pi(t-z)}}\right) \Omega(t) - \frac{a^{3/2}}{\sqrt{2(t-z)}} \frac{\mathrm{d}\Omega(t)}{\mathrm{d}t} dt, \tag{2.7}$$

where $\Omega(z) = \Delta\omega(z)/\omega_{res}$ (ω is the angular frequency, $\omega = 2\pi f$).

Note that both method treats the oscillation amplitude a as a constant, therefore keeping a constant during data accusation is one of the most important key-concept of the FM-AFM technique. Throughout this work the latter, Sader method is used for force calculations. However, for comparison both methods were implemented into a simple software and generally they produce exactly the same results. Even though a slight difference can be observed from time to time due to differences in numerical approaches.

In order to obtain atomic resolution by AFM, short range forces needs to be imaged. When the tip is far from the surface the electronic orbitals of the tip apex atom do not overlap with the orbitals of the surface atom beneath. When these two atoms are brought closer and closer to each other overlapping will occur. If empty orbitals are present, energy can be gained by incorporation of valence electrons into these orbitals leading to an attractive interaction (force). This chemical bond length usually scales to a order of few Å or even less. By further reducing the separation the attractive component reaches its saturation (maxima) and Pauli repulsion becomes more and more dominating. The potential energy can be represented with the Morse potential (for a diatomic system). The V_{Morse} is written in form:

$$V_{Morse} = E_{bond}(-2e^{-\kappa(z-\sigma)} + e^{-2\kappa(z-\sigma)}) \tag{2.8}$$

and the force ($F(x) = -\mathrm{d}E/\mathrm{d}z$) acting between the two atoms is just

$$F_{Morse} = -2\kappa E_{bond}(-e^{\kappa(z-\sigma)} - e^{-2\kappa(z-\sigma)}) \tag{2.9}$$

From this we can see that the short range chemical interaction depends exponentially on the tip–sample separation $F_{SR}(z) = F_0 e^{-2\kappa_F z}$ (as the tunneling current). Theoretically, the optimal signal-to-noise ratio (SNR) is achieved at the value of the oscillation amplitude comparable with the characteristic decay length (κ_F) of the forces responsible for imaging ($A_{opt} \approx 1.545/\kappa_F$ based on the calculations in reference [16]).Thus, the optimal oscillation amplitude should be in the order of few Å or even less. Beyond, an additional benefit of the small oscillation amplitudes is the reduction of the sensitivity to long-range force contributions. Also the large amplitude operation significantly decreases the measured value of the time averaged current and subsequently reduces the sensitivity of the tunneling current detection. Therefore the application of small amplitudes in simultaneous AFM/STM experiments seems to be natural choice.

At the beginning, mainly silicon–based cantilevers oscillating with large amplitudes (tens of nanometers) were used, because they possess the important oscillation stability [29–31]. The key factor is to achieve atomic resolution with the proper choice of several parameters, for example the spring constant and the oscillation amplitude (see Table I in [32]). Consequently, a new kind of sensor was introduced based on a quartz resonator into the field of FM-AFM. So far the most popular and reasonable way to reach the desired small amplitudes is replacing the micro-fabricated (Si) cantilevers by stiff, piezoelectric quartz tuning forks similar to those used

as frequency etalons in watches. The configuration when one of the prongs is attached to a solid substrate and the free prong acts as a cantilever with the capability of self-sensing, is called qPlus, named by Giessibl [8]. One of the largest benefits of this design is that it has nearly the optimal stiffness for operating FM-AFM with low amplitudes but keeping the force sensitivity high enough [16]. Not surprisingly, qPlus design presented high potential for outstanding atomic scale imaging from its early stages [33]. In addition, the parts of the qPlus sensor are large enough for assembling of the sensor simply by hand. Note that using length extensional resonator is another interesting alternative to the qPlus configuration [34, 35]. The comparison of their performance is still an opened issue in the community [16].

Unfortunately, in the case of quartz based sensors with self-sensing, the presence of the tunneling current may introduce an undesired interference (cross-talk) between the current and the deflection channel. Therefore special attention has to be paid to minimize the impact of this phenomena to a negligible level. Albers *et al.* [36] already mentioned a kind of coupling of tunneling current and used, as a solution, a separate wire for current measurement. In Section 4.1.2 the origin of the coupling between the deflection and the tunneling current channel will be investigated in more details.

2.2 Electron spectroscopies

2.2.1 Photoelectron spectroscopy

Photoelectron spectroscopy is based on the interaction of (X-ray) photons with a solid matter. This interaction generates (photo)electrons via the so-called photoelectric effect. The photoelectric effect was discovered by Heinrich Rudolf Hertz in 1887, later on Albert Einstein explained in details its background mechanism, he was awarded a Nobel Prize in Physics 1921. Later on, Kai Siegbahn *et al.* developed a surface analyzing tool based on photoelectron effect. With his instrumentation the first high-energy resolution X-ray Photoelectron Spectroscopy (XPS) spectrum of NaCl was recorded in 1954. Hewlett-Packard in a cooperation with Siegbahn produced the first commercial monochromatic XPS instrument in 1969 that was devoted to qualitative and quantitative chemical analyses, therefore the commercial name Electron Spectroscopy for Chemical Analyses (ESCA) became widely used for this instrument. ESCA naturally refers to both XPS and Ultraviolet Photoelectron Spectroscopy (UPS). The latter one was developed by David Turner at Imperial Collage (and later at Oxford) in the UK. In UPS, the X-ray source is replaced by a helium lamp producing ultraviolet light and it is a perfect apparatus for making valance band analyses of molecular systems. Siegbahn received the Nobel Prize in 1981 for his extensive efforts to develop XPS into a useful analytical tool. Due to the large and growing number of synchrotron facilities, the access to synchrotron light (with various energies) turned into much easier in the last two decades. Therefore performing synchrotron radiation photoelectron spectroscopy (SRPES) is an appropriate option because the energy of the monochromatised light can be freely tuned in contrast to a convectional X-ray or UV source.

Photoelectric effect

The maximum kinetic energy E_{kin}^{max} of the ejected photoelectrons can be obtained from the Einstein's formula as

$$E_{kin}^{max} = h\nu - \varphi \tag{2.10}$$

where h is the Planck constant ν is the frequency of the incident (adsorbed) photon. φ corresponds to the work-function that can be formulated with the threshold frequency ν_0 of the photoemissive surface as $\varphi = h\nu_0$. φ refers to the minimum energy required to remove a delocalised electron from

the surface of the metal. Establishing a threshold for photoemission, $h(\nu - \nu_0)$ has only positive equity when $\nu > \nu_0$. If the electron is laying in a deeper energy level, an extra energy E_i^F needs to be consumed for moving the electron up to the Fermi level. With this ionization energy (respect to the Fermi level) our Equation 2.10 will look like

$$E_{kin}^{max} = h\nu - E_i^F - \varphi \tag{2.11}$$

The electrons with the kinetic energy of E_{kin}^{max} are collected with the spectrometer. In order to avoid charging, the spectrometer needs to be in electrical contact with the sample. If they are on the same potential, it is obviously the case for metallic specimens, E_{kin}^{max} for a spectrometer having ϕ work-function is given by:

$$E_{kin}^{max} = h\nu - E_{vac}^S - \phi + \varphi \tag{2.12}$$

where E_{vac}^S is the vacuum level of the sample that is, by definition, $E_{vac}^S = E_i^F + \varphi$. Inserting, this solution for E_{vac}^S into Equation 2.12 we get:

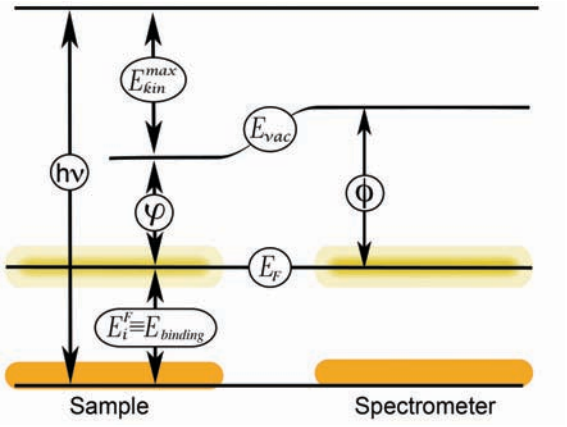

Figure 2.4: The energy level diagram of the photoemission process. The electrically conductive sample is on the same (ground) potential as the spectrometer, therefore the Fermi levels of the sample and the spectrometers are aligned. The $E_{B(inding)}$ is referenced with respect to E_F and it depends only on the spectrometer works function ϕ.

$$E_i^F = h\nu - E_{kin}^{max} - \phi(-U_{SP}) \equiv E_{B(inding)}. \tag{2.13}$$

The result for E_i^F is independent of the sample work function and E_i^F is called binding energy in photoelectron spectroscopy. The energetics of a photoemission process is summarized in Fig. 2.4. If the sample is non conductive or semi-conductive, charging of the sample will occur. As a result,

the Fermi levels are not aligned anymore, the U_{SP} potential difference needs to be taken into account. In order to have reproducible results, U_{SP} and $E_{binding}$ needs to be known with high precision and U_{SP} must to be constant all along the experiment. The latter one can be difficult especially with TiO_2 because the conductivity can change a lot after different kind of sample preparations. Therefore if it is possible, U_{SP} needs to be kept as small as possible by keeping the conductivity as high as possible.

Binding energy and chemical shift

The electron is removed by photon irradiation from the initial state $E_i(n)$ leaving a hole behind and the final state will be $E_f(n-1)$, the energy balance can be written as

$$E_B = E_f(n-1) - E_i(n). \tag{2.14}$$

As a starting approximation, one can assume that no rearrangement or any other relaxation process occurs after the electron is being removed. If it is so, E_B has the negative value of the orbital energy $-\varepsilon_k$ of the ejected electron. This assumption comes from the Koopmans' theorem, which "freezes" the electron orbitals during photoemission. However, this approximation give too much of simplification and it might lead to significant error [37]. The remaining electrons tend to minimize the energy of the ionized atom by rearranging the shield around the core of the atom (atomic relaxation) and consequently the surrounding atoms also get involved into the relaxation process (extra-atomic relaxation). E_B can be now expressed in more details as

$$E_B = -\varepsilon_k - E_r(k), \tag{2.15}$$

where $E_r(k)$ refers to the relaxation energy (final state effects).

In Equation 2.14 $E_i(n)$ refers to the initial state of the atom before the photoemission process takes place. $E_i(n)$ can change by forming or changing the bonding configuration with the surrounding atoms. Any variation in $E_i(n)$ leads to variation in the value of E_B as well, therefore, ΔE_B is called the *chemical shift*. It is usually assumed that initial state effects are responsible for the observed chemical shift, so that, as the formal oxidation state of an element increases, the E_B of the ejected photoelectrons from the element will increase [37]. It means that the change in the binding energy is just

$$\Delta E_B = -\Delta\varepsilon_k. \tag{2.16}$$

However, the correlation between the oxidation sate and the chemical shift is not always straightforward especially when the bonds have significant covalent character instead of ionic. One example is the chemical shifts of the Si 2p core level for different alkane terminated Si(1 1 1) and Si(0 0 1) surfaces. Besides having in all situations an sp^3 hybridized C atom attached to the silicon substrate, the charge distribution differs slightly, which leads to a variation of the chemical shift (see Section 4.5.4 for further details). Consequently, an approach was developed to show the impact of the charge potential on the chemical shift [37]. The charge potential model is formulated as follows

$$E_B = E_B^\circ + kq_i + \sum_{j\neq i}(q_j/r_{ij}) \tag{2.17}$$

where E_B° is a reference energy that equals to E_B for the neutral atom in most of the cases, k is a constant, q_i is the charge on the atom i and q_j is the charge on the surrounding atoms j separated by the distance r_{ij} from the atom i. It is clear now that, if the chemical interaction leads to a formation of a positive charge on the atom then E_B will increase as well. Equation 2.17 can be modified to express the chemical shift as well:

$$\begin{aligned}\Delta E_B &= k[q_i(1) - q_i(2)] + V_i(2) - V_i(1)\\ &= k\Delta q_i - \Delta V_i.\end{aligned} \tag{2.18}$$

Here V_i refers to $\sum_{j\neq i}(q_j/r_{ij})$ that is often called the Madelung potential.

Spin-orbit coupling

After the ionization the remaining electron can stay in two possible configurations: spin up or down. These states are energetically identical due to the orbital degeneracy. However, the electron spin and the angular momentum vector of the orbital can be either parallel or anti-parallel. Because of the magnetic spin-orbital interaction, the anti-parallel configuration has lower energy (higher E_B values) raising to the formation of non-degenerate Eigen states (see Figure 2.5). The total angular momentum j of an electron is described by the quantum numbers l and s and it can be

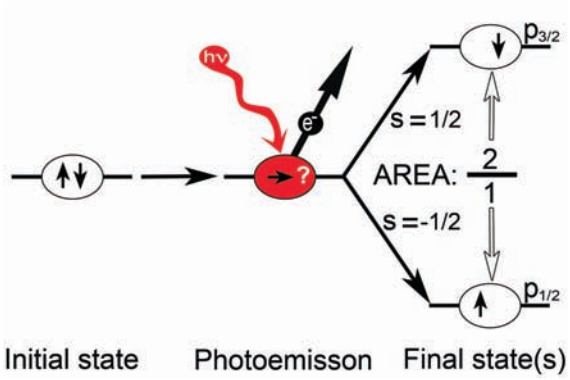

Figure 2.5: Spin-orbit coupling: After the ionization the remaining electron's spin and the angular momentum vector of the orbital can be either parallel or anti-parallel. Due to the (magnetic) spin-orbital interaction two non-degenerated Eigen states are formed.

calculated as $j = l + s$ ($j = l + 1/2$ when the two angular momenta are in the same direction and $j = l - 1/2$ for the opposite case). The occupation ratio between the spin up and down state can be obtained from $g = 2j + 1$, this also determines the intensities (peak areas) of the components. In the case of the Si 2p orbital, the orbital angular momentum quantum number $l = 1$ so the total angular momentum j is either $1/2$ (higher binding energy) or $3/2$ (lower binding energy) and the population ratio of these Eigen states are $4/2 : 8/2$ or $1 : 2$ respectively. For the sake of completeness in Table 2.1 all of the subshells are summarized. Note that the s orbital don't have spin-orbital splitting in general, a requirement for this splitting of the s photoemission peak into a doublet is that there be unpaired orbitals in the valence shells [37].

Peak width

The broadening of a measured photoelectron peak is the result of the lifetime of the core hole, instrumental resolution and satellite features. The lifetime component can be calculated from the Heisenberg uncertainty relationship:

$$\Gamma = h/\tau \tag{2.19}$$

Table 2.1: Orbitals

subshell	$j = (l + s)$	$g = (2j + 1)$
s	1 / 2	
p	1 / 2, 3 / 2	1 : 2
d	3 / 2, 5 / 2	2 : 3
f	5 / 2, 7 / 2	3 : 4

where Γ is the intrinsic peak width, h is the Planck constant, and τ is the core hole lifetime. The inner shell orbitals can be filled easier by outer electrons, therefore the lifetime τ decreases and, hence, Γ increases as deeper and deeper the orbital was holding the electron hole.
The instrumental broadening is determined by the energy distribution of the incident X-rays, by the resolution of the analyzer and by instrumental contributions and it can be characterized by a Gaussian lineshape. In summary the total full-width at the half-maximum ($FWHM_{tot}$) of an observed peak is approximated, by:

$$FWHM_{tot} = \sqrt{(FWHM_n^2 + FWHM_X^2 + FWHM_A^2 + FWHM_{ch}^2 \dots)} \qquad (2.20)$$

where FWHM is the full-width at half-maximum of the observed peak (tot), core hole lifetime (n), X-ray source (X), analyzer (A), and charging contribution (ch). The latter one (ch) becomes important for non-metallic samples, where the conductivity of the sample is limited that leads to non-uniform surface potential.
The satellite features having asymmetric line shapes originates from the contribution of vibrational broadening, multiplet splitting and shake-up satellites. Depending on the experimental conditions and on shifts in the value E_B caused by these effects, satellite features might be not distinguishable from the main photoemission peak and they contribute only to the total broadening of the given peak. Using X-ray monochromator and synchrotron light can generally decrease the impact of instrumental broadening and more buried contributions to the total with can be identified (for instance C−H vibrational losses discussed in Section 4.5.4).

Experimental setup

The shematic illustration of an ESCA machine is shown in Figure 2.6. During measurement low electron fluxes from the sample needs to be analyzed, therefore it is essential that the electrons shell not scattered away by colliding with gas phase molecules before reaching the analyzer. This can be only established in UHV environment, where the electron has longer mean free path than the size of the spectrometer. This requirement can be quite easily fulfilled because only modest vacuum (10^{-7} mbar) is needed [37]. However, the data acquisition can take up to several hours and the sample cleanness needs to be kept during that time frame. The speed of adsorption and of the development of surface contaminations demands for even better UVH conditions (10^{-10} mbar or even below), this is especially true for highly reactive surfaces such as the Si(1 1 1)–7×7.

In order to perform photoelectron spectroscopy X-rays (photons) needs to be created. Classi-

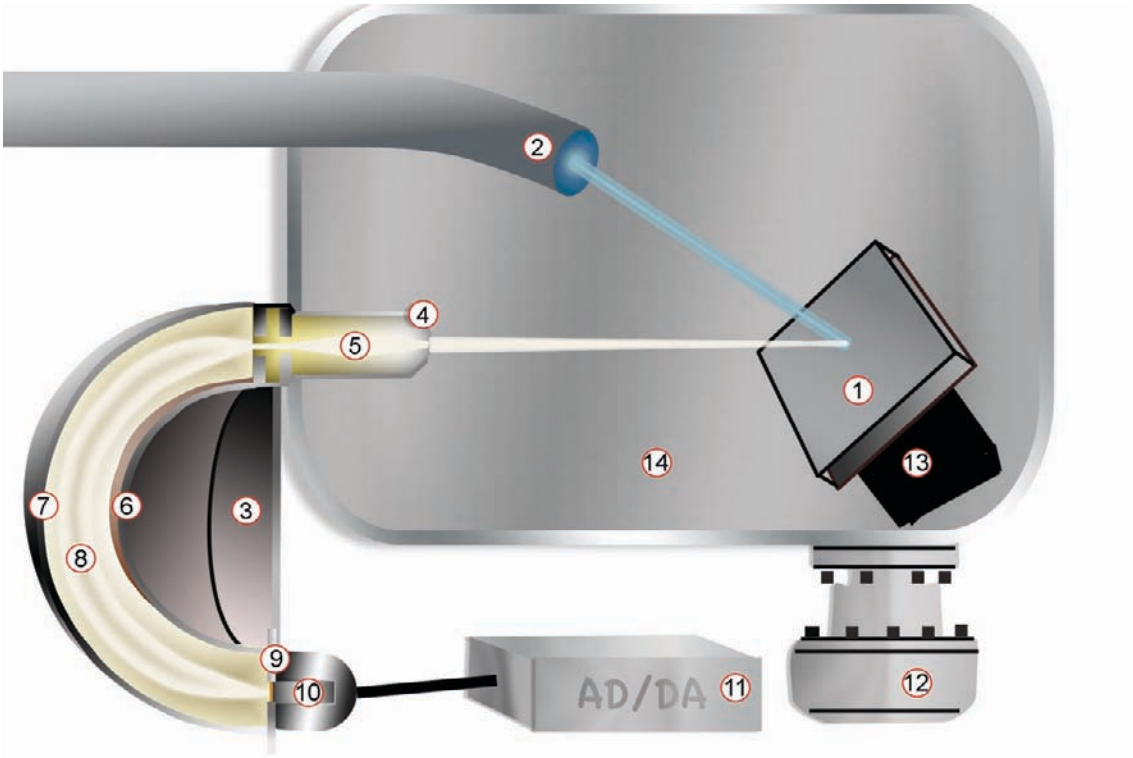

Figure 2.6: The schematic illustration of an ESCA machine with its key components: sample (1), X-ray source (2), hemispherical energy analyzer (3), variable aperture (entrance slit) (4), electron lens (5), inner (6) and outer electrodes (7), electron path inside the analyzer (8), exit slit (9), detector (10), data accusation and control system (11), vacuum pump (12), multi dimensional sample manipulator for positioning (13) and vacuum chamber (14).

cally, X-ray is produced by fluorescence effect in a way that a target is bombarded by high-energy ($\sim$ 10 keV) electrons that are capable of creating core holes in atoms of the target material. The fluorescent photons have characteristic energy for a given transition (relaxation), therefore quite narrow energy dispersion can be obtained. However, in order to minimize the FWHM of the XPS peaks further monochromatization is commonly applied, in most of the cases quartz serves as diffracting element. There is a further advantage of using monochromator, that is, the presence of satellite peaks can be depressed by off-filtering additional, less intensive fluorescence lines. Furthermore, also a thin metal film (Al) is placed in the X-ray path to eliminate electrons, background emission (Bremsstrahlung) and heat from the source [37].

As it was already mentioned, synchrotron radiation is an alternative option to conventional X-ray sources. In fact, the synchrotron produce broad band (from infrared to very hard X-rays) light. That light usually is highly collimated and polarized and it can have very high intensity. Only disadvantage of these facilities that users need to travel and perform the experiments at the place of the light source. Usually the research needs to be organized well before the actual measurement

that needs to be performed in a relatively short time period. As a consequence, any instrumental failure or need for further investigations may elongate the time frame to several years even.

In most of the experimental setups, the emitted photoelectrons are analyzed by a hemispherical energy analyzer. In which, the electrons are collected by the collection lens, energetically selected by the energy analyzer than counted by the detector. The collection lens allows high collection angle that is beneficial because much more electrons can be collected from the incident photon excitation. Therefore, lower light intensities can be used which opens the possibility of better light monochromatization or lower sample degradation caused by X-ray irradiation. However, wide acceptance angle obviously lowers the angular resolution. To be able to tune the operation mode for the experiment, an aperture is placed to the entrance of the analyzer. Nevertheless, closed aperture operation increases the accusation time or higher photon flux is needed. To overcome of this problem, two dimensional analyzers were developed, the kinetic energy is detected as a function of their emission angle, providing information about also the dispersion simultaneously [37]. The hart of the analyzer consists of two concentrical electrodes, which are kept at different potentials. Due to the applied potentials, only electrons with the desired kinetic energy (pass energy) can reach the detector that is usually a channeltron or a multichannel detector plate. The electronic signal produced by the detector is passed to the data accusation system in which also the mode of the operation can be selected. These operation modes are:

- ΔE = constant (FAT = fixed Analyzer Transmission mode) applying a constant pass energy
- $\Delta E/E$ = constant (FRR Fixed Relative Resolution) applying a constant energy ratio where ΔE is the $FWHM$ (Full Width at Half Maximum) of a given peak and E its kinetic energy [37].

Finally, in order to be able to control position of the sample, it needs to be mounted on a multidimensional manipulator that can adjust the position in three dimension and also the angle with respect to the analyzer/X-ray source.

2.2.2 Auger electron spectroscopy

As it was visible in the previously discussed process, the incident photon creates a hole in an electronic level by removing the electron via excitation. Here we have to mention that in Auger electron spectroscopy (AES) an electron source is used instead of photons for primary ionization. The hole can be reoccupied by an electron from an upper energy level. By this process the electron

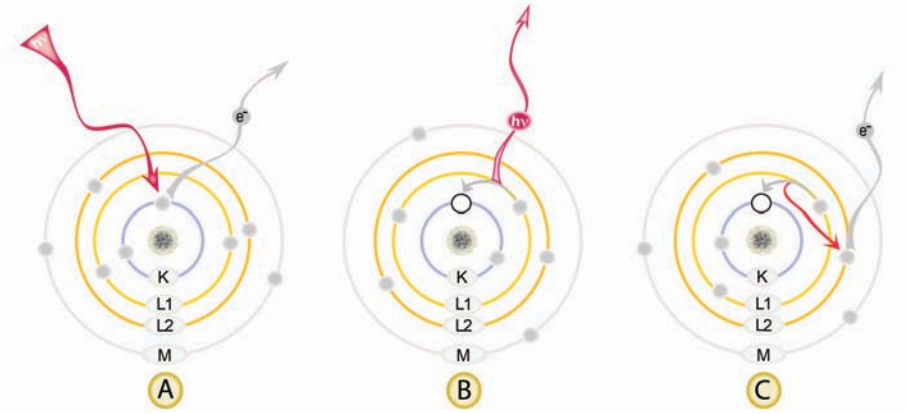

Figure 2.7: Schematic illustration of the production of photoelectrons (A), characteristic X-rays (B), and Auger electrons (C). An electron in the K shell is ejected from the atom by an external primary excitation x-ray, creating a vacancy (A). An electron from the L shell "jumps in " to occupy the vacancy and emits a characteristic x-ray unique to this element (B) or the energy gained during the "jump" is transferred to one of the outer electrons causing it to be ejected from the atom (Auger electron) (C).

gains and emits the energy raising from the difference between the two levels. This emitted energy can be transferred to a second electron being on the high laying state and the electron due to its secondary excitation is ejected, this secondary electron (the primary was the photoelectron) is named as Auger electron after Pierre Victor Auger who, probably as first, discovered this kind of emission in 1923 during his Phd. study. In general, the maximum kinetic energy $E_{kin}^{max}(WXY)$ of the electron produced by the WXY Auger process is governed by three parameters: the ionization energy $E_W(Z)$ of the electron W on the core level Z that is removed by the ionizing beam; the ionization energy $E_X(Z+\Delta)$ of the electron X on higher laying, $Z+\Delta$ shell that electron is replacing the hole produced by the ionization process; finally the ionization energy of the electron Y staying on the same atomic level as X was. The Y is the auger electron that takes the energy $E_W(Z) - E_X(Z+\Delta)$ and leaves the state described by the energy $E_Y(Z+\Delta)$ into the vacuum. In summary, the maximum kinetic energy $E_{kin}^{max}(WXY)$ is just:

$$E_{kin}^{max}(WXY) = E_W(Z) - E_X(Z+\Delta) - E_Y(Z+\Delta) - \Phi(-U_{SP}), \tag{2.21}$$

where Φ is the work function of the analyzer and the potential $-U_{SP}$ must be considered here as well (see discussion above). The term Δ (varies between 0 and 1) denotes the displacement of an electronic level towards higher binding energies after the ionization of the atom by the primary electron. $\Delta = 0.5$ represents a fair approximation for an estimate of the kinetic energy [37].
An example is visible in Figure 2.7 for the Auger process. In this particular case, the primary electron is removed from (W =)K shell and an electron from the (X =)L_1 occupies the state

of the primary electron. A second electron ejected from (Y =)L_2 state by gaining the energy difference between the K and L shell. In this scenario the energy of the incident electron be must be sufficiently high to cause primary ionization of the core level K. The measured peak is called KLL referring to the Auger electron process described by these specific energy levels. The nomenclature of AES orbitals in comparison with the ones used in XPS is listed in Table 2.2. Because the energy of these atomic levels are specific to each atom, the emitted Auger electrons have also characteristic energy allowing one to identify the emitting elements.

Table 2.2: Difference in the nomenclature of orbitals in AES and XPS

n	l	j	Index	AES notation	XPS notation
1	0	1/2	1	K	$1s_{1/2}$
2	0	1/2	1	L_1	$2s_{1/2}$
2	1	1/2	2	L_2	$2p_{1/2}$
2	1	3/2	3	L_3	$2p_{3/2}$
3	0	1/2	1	M_1	$3s_{1/2}$
3	1	1/2	2	M_2	$3p_{1/2}$
3	1	3/2	3	M_3	$3p_{3/2}$
3	2	3/2	4	M_4	$3d_{3/2}$
3	2	5/2	5	M_5	$3d_{5/2}$
...	...	...	...	...	...

After the primary ionization and reoccupation of the electron hole, beside the Auger effect the atom may emit a photon carrying the energy difference $h\nu = E_W(Z) - E_X(Z + \Delta)$ (see Fig. 2.7). Therefore the total transition rate ω is a combination between radiative ω_X and non-radiative (Auger) ω_A decay processes. Hence the Auger electron yield is

$$\omega_A = 1 - \omega_X = 1 - \frac{W_X}{W_X - W_A} \tag{2.22}$$

where W_X and W_A corresponds to the transition probability of the fluorescence (X-ray) and Auger pathway respectively. In general the Auger path is preferred by lighter elements and the photon emission occurs more frequently for heavier ones. However, the emission probability from an LMM or MNN Auger process shows reasonably high value even with high atomic number Z [37].

In order to detect Auger electrons characteristic for a given transition, they need to be able to leave the specimen without any loss in their kinetic energy. The electron has a characteristic distance that is the escape depth determined by the attenuation length of Auger electrons λ and

the kinetic energy E_{kin}:

$$\Lambda = \lambda \cos\theta \tag{2.23}$$

where θ is the emission angle of the Auger electrons with respect to surface normal. The probability for an electron to travel over a distance x without any collision is proportional to $e^{-x/\lambda}$ with 95 % of the Auger intensity coming from within 3λ of the surface. Depending on the kinetic energy of the electron, λ varies from 2 to 20 monolayers, where the thickness of a monolayer is approximatively 0.2–0.25 nm for metals [37]. To express the transportation properties, several terminologies are commonly used: inelastic mean free path (IMFP), mean escape depth (ED), information depth (ID).

As it was already shown in the previous part, change in the chemical environment induce change in the binding energies. As a consequence, the change in binding energy also induce chemical shift for the Auger transition. However, the Auger transition involves there energy levels (see Equation 2.21) and therefore the exact position of the peak is the result of even more complex initial and final state effects. Even though, the Auger peak composition is complicated based on the long and deep investigations, for instance, the structure of the Ti LMM peak in different oxidation state and in different chemical environment is known allowing experimentalists to identify each states [37].

Instrumentation

Similar experimental considerations can be made for Auger electron spectroscopy as it was already done for ESCA (see Fig. 2.6 and its discussion), therefore only the Cylindrical mirror analyzer (CMA) will be considered here. The CMA equipped with an electron gun is the most common configuration for AES and its schematic illustration is visible in Figure 2.8.
The Auger electrons are produced by electron irradiation from the electron source. The heart of a CMA is the inner and outer cylinder. By applying variable potential between these cylinders the incoming electrons can be separated by their kinetic energy E. In combination with the retarding field optic, the pass energy (energy resolution) can be chosen to a desired value. Electrons allowed to pass the analyzer are riching the channeltron that produces a electronic signal proportional to the number of detected electrons, N, described with the kinetic energy E. In practice not only Auger electrons are detected, therefore the Auger peaks are only superimposed on the spectra $N(E)/E$. However, with a non-monochromatized source, only the Auger peaks present sharp components, others only giving intensity into the background. Therefore AES spectrums are

commonly recorded in derivative mode ($^{dN}/_{dE}$). The derivation can be done by using an AC voltage component (with the DC offset) applied to the mirrors of the CMA. The DC offset determines the measured energy and the amplitude of the AC signal sets the with of the derivation. The derivation can be also done during the computer analyses of the recorded spectra.

As a results the points $N(E)$ of the maximum slopes will be the "Auger peaks". As the intensity $N(E)$ increases the slope of the peak will be enhanced as well, consequently the height of the $^{dN}/_{dE}$ peak carries also quantitative informations. The derivative mode has further benefit that is the fine structure of an Auger peak can be better observed.

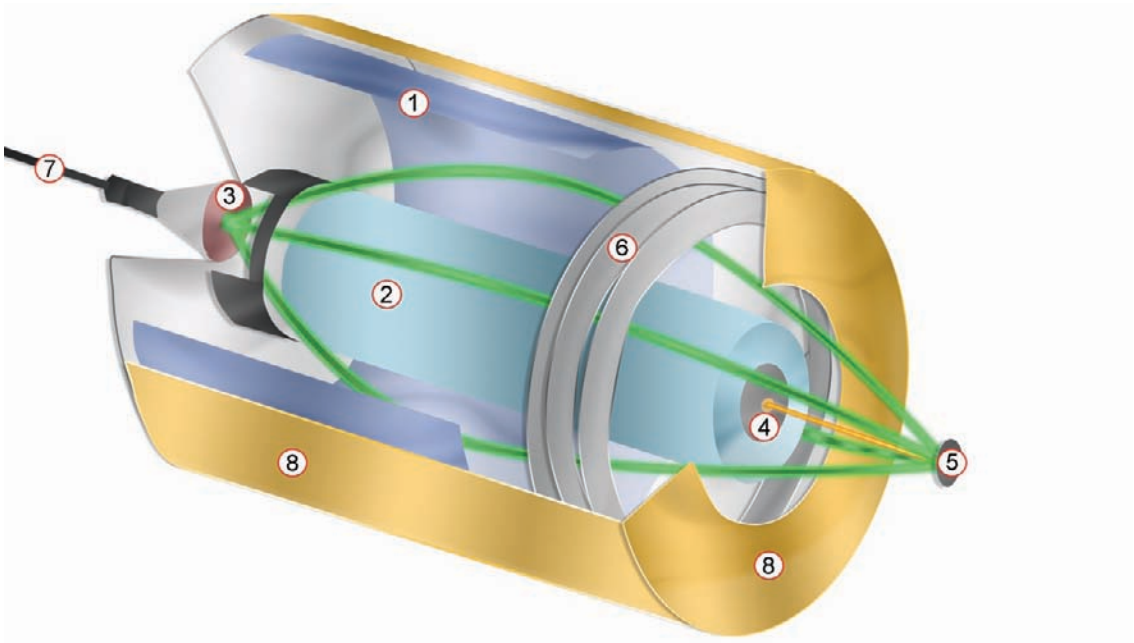

Figure 2.8: Schematic illustration and main components of a Cylindrical Mirror Analyzer (CMA). These building blocks are: outer (1) and inner (2) electrode of the CMA-optic, detector that is in most of the cases is a channeltron (3), electron gun (4), sample (5), retarding field optic (6), connection to power supplies and data accusation system (7) and enclosure (8).

"It's not given to people to judge what's right or wrong. People have eternally been mistaken and will be mistaken, and in nothing more than in what they consider right and wrong."

Leo Tolstoy, War and Peace

3

The material systems investigated in this thesis

3.1 Characteristics of the TiO_2 support

Among the large variety of investigated metal oxide systems, titanium dioxide is the most studied material and in the last few decades the applications of TiO_2 has been grown very rapidly (see the excellent review by Ulrike Diebold [4]). It is used as a support in heterogenous catalyses, as a white pigment, as an anticorrosive coating, for biocompatible bone implants. Furthermore, it is valuable for green energy constructions, such as solar cells for production of hydrogen and electricity. Beside all major applications, dominantly the better understanding of catalytic reactions have been drawn the interest of surface scientists to this system. Generally, a heterogeneous catalytic system consist of small supported metal clusters, therefore investigations of the growing mechanism of metals on TiO_2 became very popular. In most of the cases, the investigations are performed on rutile surfaces, particularly on the (110) facet. Although, anatase has also been considered many times because of its technological relevances [38–40].

3.1.1 Bulk properties

Titanium dioxide has three major different structures: rutile (tetragonal), anatase (tetragonal) and brookite (rhombohedrical). The bulk structure of rutile belongs to the D_{4h} symmetry group with the fallowing latice parameters: $a = b = 4.584$ Å, $c = 2.953$ Å [4]. The unit cells contains six sixfold coordinated Ti atoms in a slightly distorted octahedral configuration (see Fig.3.1).

Titanium dioxide is a member of reducible oxides meaning that it can be easily reduced by

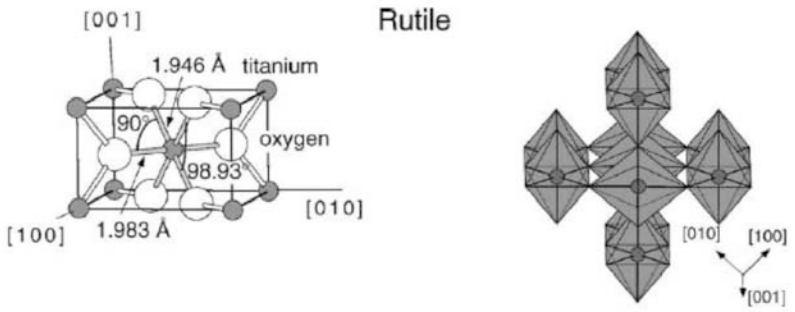

Figure 3.1: The bulk structure of rutile. The image is taken from Ref. [4].

temperature treatment. Consequently, many stable phases with different crystal structures appear on titanium/oxygen phase diagram (Figure 3.2). Bulk oxygen defects are acting as color centers which produce color changes of TiO_2 from transparent to very dark blue. Oxygen deficiency alters also the electrical properties of the crystal. These intrinsic defects create an n-type doping level in the band gap resulting a significant increase in conductivity. Compared to other common oxide supports like Al_2O_3, the fact that TiO_2 can be very conductive makes this substrate attractive for number of surface investigations, which are made, for instance, with scanning tunneling microscopy or photoelectron spectroscopy.

3.1.2 Rutile (1 1 0) surface

1×1 "bulk" termination

The rutile (1 1 0) surface is the most studied surface of the TiO_2 because it is very stable and convenient for fundamental studies of different kind of adsorption mechanism due to its relative simplicity. The structure of the bulk terminated TiO_2(1 1 0)–1×1 is presented in Figure 3.3. It is build up with several type of oxygen and titanium atoms. The top most layer of the 1×1 is

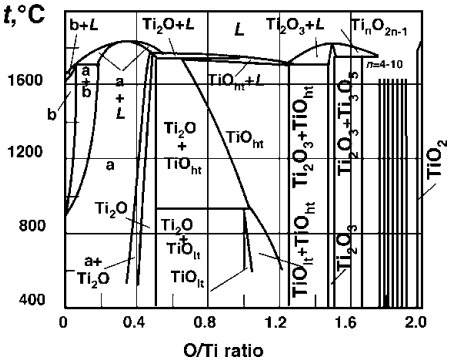

Figure 3.2: Phase diagram of the Ti−O system (from Ref. [4]).

populated by the so-called bridging oxygens, O_{bridge}. Beside bridging oxygens, the surface is also terminated by five fold coordinated Ti atoms, Ti_{5f}, with one dangling bonds perpendicular to the surface, and by in-plane oxygens, $O_{\text{in-plane}}$. An oxygen in bridge position is bounded to two six fold coordinated titanium atoms, Ti_{6f}. For adsorptions a very important surface defect is formed by removing one bridging oxygen, the oxygen vacancy, O_{vac}. The (thermal) energy needed to create an oxygen vacancy is relatively low because the oxygen in bridging position has lower coordination (two) compared to bulk ones (three). Due to the lower coordination of the bridge oxygen atom, the oxygen vacancies presents high mobility. One, obvious, possible pathway is among the oxygen rows (in [0 0 1] direction). This migration needs an activation energy, which was experimentally determined to be 1.12 eV in good agreement with the 1.02 eV theoretical value obtained by DFT calculations [41]. Surprisingly, Schaub *et al.* demonstrated that in the presence of molecular O_2 on the surface O_{vac}s have very high mobility perpendicular onto the rows ([0 0 1] direction) even at room temperature [42].

One of the most studied vacancy related reaction on TiO_2(1 1 0)–1×1 is the dissociation of water. The water tends to adsorb on the vacancy and dissociates, forming on OH group (see Figure 3.3) [44–46]. OH groups are also naturally exist on TiO_2(1 1 0)–1×1 even in the extreme UHV environment (pressure below 10^{-10} mbar) due to the presence of small amount of residual water. Therefore, if the goal of an investigation is concerned about vacancies, the time of experiment and the quality of UHV are crucial factors. The oxygen vacancies are generally acting as adsorption centers and as nucleation centers for the formation of metal cluster. For example, in the case of gold it was shown that their nanoclusters nucleate homogeneously on the terraces of the reduced and oxidized supports, whereas on hydrated TiO_2(1 1 0)–1×1 surface clusters form preferentially at the step edges [47].

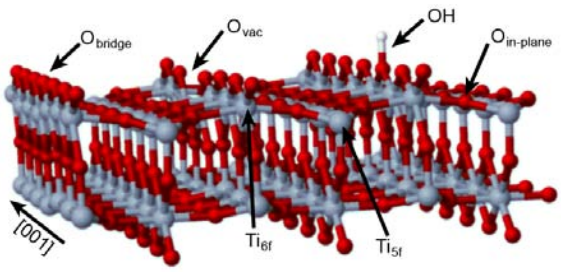

Figure 3.3: Ball-and-stick model of the TiO_2(1 1 0)–1×1 surface including the two typical type of defects commonly appearing on the surface; the oxygen vacancy, O_{vac} and the hydroxyl group, OH (based on the image presented in Ref. [43]). Special thanks to Cesar Pascual Gonzalez for providing the raw data of the structure.

Scanning probe surface characterization

Applying numerous surface characterization methods, especially at the same time, can significantly enhance the possibility of finding the correct answer for our questions. Scanning probe techniques, namely scanning tunneling microscopy and atomic force microscopy, have the advantage over others that they can image the surface in real time and even with very high speed (so called video rate SPMs). This makes them extremely useful tools for studying atomic-scale structures.

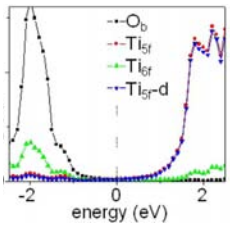

Figure 3.4: Computed total DOS (from Ref. [43]) on bridging oxygen O_b, Ti_{5f}, $Ti_{5f\text{-}d}$ (exclusively d-orbitals) and Ti_{6f}. During an STM scan the bias voltage is usually set to be between 1 and 1.6 V where predominantly Ti_{5f} 3d-like orbitals are contribution to the DOS. Therefore, under these conditions the STM tends to image the under-coordinated Ti atoms.

The scanning tunneling microscope measures the electronic structure of a conductive sample. Therefore it is not always obvious that the resulted image is a reflection also of the topographic structure or not. Titanium dioxide is an insulator but can be reduced easily by annealing (forming an n-type semiconductor as a result). In this case the Fermi level moves close to the conduction-band minimum (CBM) in the 3 eV band-gap. Therefore electronic conduction can occur predominantly through high-lying donor states (see for more details the work of Yagi *et al.* [48]). Albeit, the correct assignment of this state is still an opened issue (i.e. it is the result more of interstitial Ti species or more of oxygen vacancies) [49]. Atomic resolution can be archived on $TiO_2(1\,1\,0)$–1×1 in the most of the case by imaging empty (unoccupied) states. In other words the sample is usually biased to be positive and the bias voltage usually set to be between 1 and 1.6 V. As it can be seen from the total density of states presented in Figure 3.4, these states predominantly consist of Ti_{5f} 3d-like orbitals. Therefore, under these conditions the STM tends to image the under-coordinated Ti atoms, in spite of the physical protrusion of the O atoms, giving an apparent reversal of topographic contrast on the stoichiometric 1×1 [43, 50, 51].

In Figure 3.5 a typical STM scan of $TiO_2(1\,1\,0)$–1×1 is presented and several types of protrusions (dark and bright) clearly appears among Ti (bright) rows. In order to see better differences in the contrast, the image is also presented in 3D on the right side. Predominantly, three different groups can be made among surface defects of the 1×1 termination. The first one appears more

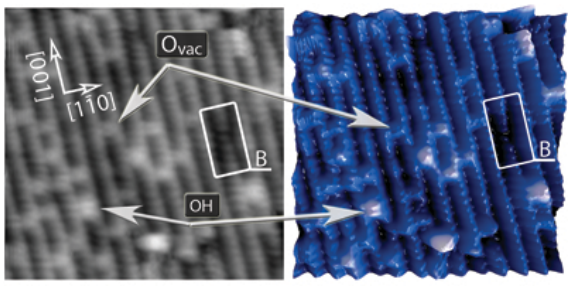

Figure 3.5: Atomically resolved STM image (10×10 nm^2, $U_{bias} = 1.0$ V, $I_t = 0.1$ nA) of the stoichiometric TiO_2(1 1 0)–1×1. The surface exhibits typically several kinds of defect sites. Here, these defects are identified based on the comparison with other images (and assignments) in the literature (see text). For better visual inspection, the image is also presented in *3D* on the right.

or less as bright as the Ti rows, they are associated with oxygen vacancies, O_{vac} (also marked as *"type-A"*, BBO_V in some publications). The O_{vac} was identified experimentally by adsorbing oxygen on the surface. These measurements showed that the number of O_{vac} defects significantly decreases with growing oxygen dosages [52].

The second one is somewhat brighter and centered closer to Ti_{5f} rows. This feature can be assigned to hydroxyl group formed by dissociation of residual water molecules in oxygen vacancies. Generally, the number of O_{vac} decreases while more and more OH is formed with the time of experiment. The speed of this process significantly depends on the level of UHV. Because, O_{vac} and OH appears in a very similar fashion in STM images, distinguishing between them can be a quite difficult problem. Only recently, STM with the capability of real time, direct observation of the reaction of water in O_{vac} made straightforward progress in this manner [44, 46, 53, 54]. Beside controlled surface reactions, an OH group can be identified by applying a bias pulse with a voltage of 3 V: by this procedure individual H atoms can be desorbed (and the defect disappears from the following STM scan) but the vacancies are remaining intact [53]. Apart from experimental investigations, also DFT studies gave more hint for their appearance [43, 54].

Finally, the last, less commonly presented feature is marked with *B* (according to Diebold's *type-B* assignment [52]) and appears as darks depressions among the Ti row. They can be as wide as several unit cell but as it can be seen in figure 3.5 the atoms seem to be preserved in their position, only their apparent hight is depressed. The origin of such darkening is not resolved yet but they are speculated to be related with subsurface defects, namely oxygen vacancies [4]. Recently, combined DFT and AFM/STM measurements shown that subsurface hydrogen atoms are found to reside in a stable interstitial site as subsurface OH groups detectable in scanning tunneling microscopy as a characteristic electronic state but imperceptible to atomic force microscopy [55–

57]. In a similar way, subsurface defect have an impact on STM contrast of anatase $TiO_2(1\,0\,1)$ where oxygen vacancies at subsurface bulk sites are significantly more stable than on the surface [58, 59].

Line defects and the 1×2 resonstruction

The removal of the oxygen from TiO_2 by sputtering and vacuum-annealing produces a crystal that is reduced. As a result the crystal becomes not just more and more conductive but line defects elongated in the [0 0 1] direction occur on the surface. These line defects (generally called strings or strands) can form an ordered structure that is the 1×2 resonstruction. Therefore all of the strands can be viewed as precursor of 1×2. There have been many attempts made for finding the exact structure for these strands and it is still not fully understood [60–75]. Several examples for line defects are visible in Figure 3.6.

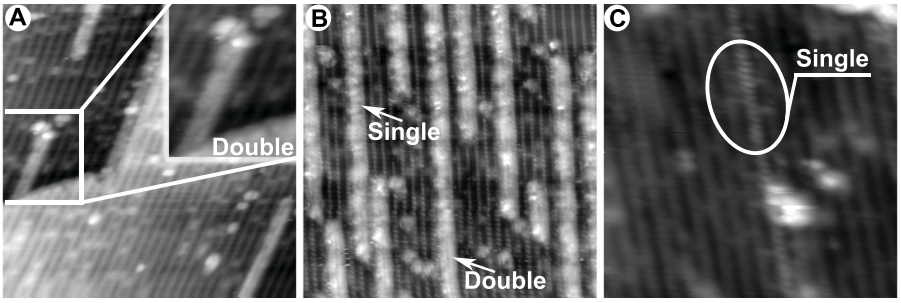

Figure 3.6: STM images. of typical line defects (U_{bias} = 0.9 V, I_t = 0.2 nA). These defects (strings or strands) are usually grown from the upper terraces and observed as double-strand structure (A). However, it can be observed on the high resolution images that the double character is not fully developed (B) or even a complete single strand can be found (C).

Prior to STM investigation, the 1×2 LEED pattern observed after high-temperature annealing was interpreted as alternate bridging O rows that are removed from the stoichiometric 1×1 termination. ("missing-row model") [60]. This idea was supported by the observed change in the Ti:O AES ratio upon the formation of 1×2 and by the appearance of the Ti^{3+} in the valance band. When the bridging oxygen atom is missing on the surface, the Ti^{4+} state with sixfold coordination numbers is reduced to a Ti^{3+} state with four-fold coordination numbers. Therefore, according to the missing-raw model the 1×2 surface is constructed by continuos rows of oxygen defects [60]. This simple model was later refined by STM studies to include lateral and in-plane relaxations [62].

In Figure 3.6A, the coverage of the strings is very low and they grow preferentially out of the upper terrace on the lower one (see inset). Each of them are composed of bright double strings,

separated by 5.5 Å. The strands have apparently smaller height than the step edge of 3.2 Å. The position of the double strands are located above the oxygen rows (although slightly shifted from the center) and the strand itself is centered above the five fold coordinated Ti atoms, Ti_{5f}. This observation shows very nice agreement with the previous STM results for the missing-row model with relaxations [62] and suggest that proposed model can not be ruled out only by STM.

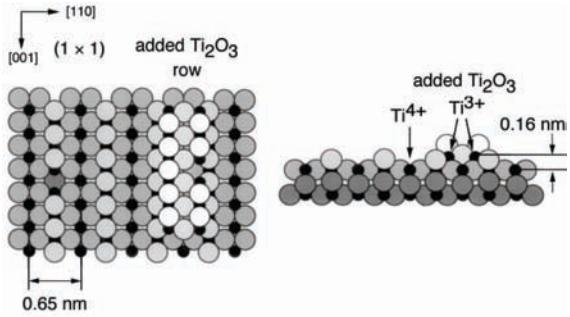

Figure 3.7: Plan and side views of the model developed by Onishi and Iwasawa where double rows of Ti (filled circles) occupy interstitial sites in stoichiometry of Ti_2O_3 [61, 63].

Onishi and Iwasawa proposed a different model consisting of double rows of Ti cations in a distorted tetrahedral configuration with Ti_2O_3 stoichiometry, these rows are "added" to the 1×1 termination [61, 63]. The proposed model is shown in Figure 3.7, the double rows of the string (see Figure 3.6A) can be correlated with the rows of Ti^{3+} and by neglecting electrical effect for a moment, the height of the added row is smaller than a regular step edge. Therefore, the Onishi-Iwasawa model can also explain well the observed STM images. Furthermore, the missing row model is in contradiction with ESDIAD (Electron Stimulated Desorption Ion Angular Distribution) result from the 1×2 surface and the measured data supports better this model [64]. However based on STM [65] and later on AFM results [68], Pang *et al.* found contradictions with this model and proposed another, called missing unit model. Among all of the models had been proposed so far, according to DFT calculations the added Ti_2O_3 rows appeared to be the most stable [69] and the calculated STM image of these rows had the best agreement with experiment. Finally, a recent combined LEED, STM and DFT investigation also showed that the best fit between different kind of experiments can be obtained with the Onishi-Iwasawa model [72, 74].

Figure 3.6b presents an other example for the appearance of strands on the $TiO_2(1\,1\,0)$–1×1. In contrast with those on Figure 3.6A, here they don't have that well developed double string internal structure. At some places they appear to be having more like single character. Figure 3.6C presents an atomically resolved single string growing out from the upper terrace with the apparent height of 6 Å. The origin of these special strings was solved by Park *et al.* [73]. The single string is

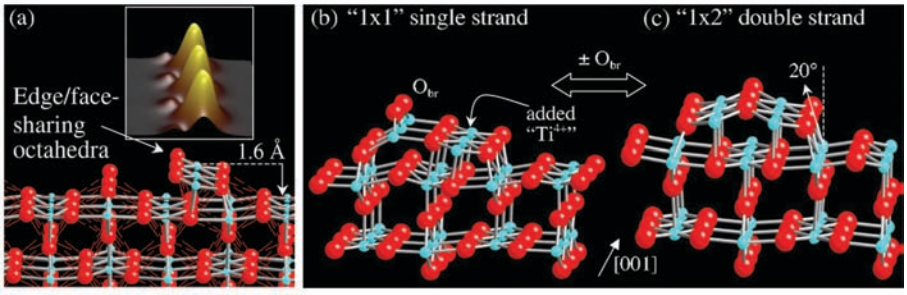

Figure 3.8: (a) DFT-relaxed structures of an interstitial Ti row, (b) single strand with 1×1 periodicity and (b) the Ti_2O double strand (from [73]).

a Ti-O structure, a partially complete octahedra centered on interstitial Ti. The edges of the equatorial O plane is shared with each other along the row and the faces are also shared with the substrate octahedra (see Figure 3.8A). Note here that, the notation "interstitials" strictly speaking is used only for bulk features, but in the literature it is a widely used for surface atoms as well due to their "interstitial" like position with respect to the supporting lattice. The inset in Figure 3.8A shows the calculated STM image giving a very good agreement with the experimental findings. The formation of double strand is explained by by adding additional Ti and O to the edge- or face-sharing octahedra. Figure 3.8A shows the most stable Ti_2O_2 strand. The geometry of Ti_2O_2 strand is the same as before and the second O row becomes the bridging O row of the surface. The height of the strand is about 1.6 Å, which is half of the hight of a step edge. The Ti_2O_2 single strands in fact generating a new 1×1 surface. When the surface gets reduced by loosing the bridging O row a double strand is formed with Ti_2O stoichiometry (see Figure 3.8B). Beside well explaining the observed line defects, the extra advantage of the Park model that it also gives a hint about the reversible transfer between the 1×1 and the 1×2 reconstruction. By comparing the model proposed by Onishi-Iwasawa and Park *et al.* it can be easily concluded that by STM or AFM it is difficult to judge which model is the right one. Apart from the fact that the two model differs from each other in oxygen stoichiometry, the reconstructed Ti atoms occupy interstitial sites and appear to be almost identical in the $[0\,0\,1]$ direction but the two model is different in the $[1\,\bar{1}\,0]$ direction. In the case of the Onishi-Iwasawa structure, interstitial Ti atoms are on the Ti-only columns, whereas they are on top of Ti-O columns in the Park model. Very recently the 1×2 reconstructed surface was investigated by high-voltage electron microscopy (HVEM) and aberration-corrected high-angle annular dark-field (HAADF) scanning transmission electron microscopy (STEM). The results with these new and exciting technique coincided only with the Park *et al.* model [75]. The benefit of the advanced TEM surface imaging is that the

resolution can be especially very high (sub-Å) [76] and the probe is well characterized and defined electron beam in contrast with SPM techniques where a change in the probe can effect drastically the observed image making the physical interpretation very difficult.

In summary, finding the real structure of the line defects on $TiO_2(1\,1\,0)$–1×1 is a challenging problem and it has been not fully solved during the last two decades. By simply counting the number of agreements, the model proposed by Onishi and Iwasawa seems to be the most accepted one [64, 69, 71, 72, 74]. The model proposed by Pang *et al.* and Park *et al.* corresponds to a surface state which has much larger oxygen deficiency. Therefore as it was already stated by other authors, it can be the case that the composition of the line defects and the 1×2 reconstruction can alter [4, 66]. However, the latest data from Shibata *et al.* (published in 2008) gives a very strong credit to the Park model. The fact that they inspected wide variety of samples and the results appeared to be constant gives further more support [75].

Despite the fact that the bulk terminated 1×1 is considered to be very stable, the (110) surface can reconstruct in to a more reduced form, to the 1×2 reconstruction. Interestingly, the origin of the single crystal also can affect the stability of 1×1. This can be associated with slight differences in productions. Thus the concentration of different kind of contaminations (mainly Ca, K) alters. In Section 4.2, the effect of potassium deposition on the surface reconstruction and on the morphology will be discussed in details. It will be shown that the potassium can easily drive the bulk terminated surface into the 1×2 reconstruction at quite low temperature due to the strong affinity of potassium to oxygen. In the following section the basic theoretical background of the metal/oxide interactions are going to be addressed.

3.2 Formation of ultrathin metal layers on TiO_2

As it was already stated among plenty of possible applications of TiO_2, one is it can serve as an oxide support for nanosized metal particles. The interaction between metals and oxide supports has great importance for heterogeneous catalysis. Therefore, the fabrication of ultra-thin metal films on oxide support has been attracted great interest and the investigation of their growth mechanism became necessary. By reducing the size of the supported particles to the size of few nanometers, the density of metal-oxide interfaces are rapidly increasing and the interaction between them becomes more and more relevant. Especially, the so-called strong metal-support interaction (SMSI) appeared to have great relevance on the chemisorption capacity for H_2 and CO of metal clusters supported on the reducible TiO_2 [77]. The encapsulation or in other words decoration layer has its own technological relevance, it can block active catalytic sites from being participating in chemical reactions. In order to better understand this interaction, so-called model systems were developed. A model system consist of well defined support, like $TiO_2(1\,1\,0)$–1×1, and clusters of metal nanoparticles under UHV condition that provides extremely high cleanness.

3.2.1 Thermodynamics

In general when a metal, M, is deposited onto TiO_2 surface the oxygen affinity of the deposited metal plays a very important rule, M should reduce the substrate and M itself becomes oxidized:

$$\mathrm{M} + \mathrm{TiO_2} \longrightarrow \mathrm{MO_x} + \mathrm{TiO_{2-x}}\,.$$

This process is thermodynamically favorable, if the change in the standard free energy (ΔG° = ΔH° - $T\Delta S^\circ$) is negative. TiO_2 can be easily reduced to a lower oxide:

$$2\,\mathrm{TiO_2(s)} \longrightarrow \mathrm{Ti_2O_3(s)} + \tfrac{1}{2}\,\mathrm{O_2}$$

$$\Delta H^\circ_{red.} = \Delta H^\circ_{f,\mathrm{Ti_2O_3}} - 2\Delta H^\circ_{f,\mathrm{TiO_2}} = 368\ \mathrm{kJ/mol}\ \ [4,78].$$

The difference in formation entropies of the oxides can be neglected, because the major entropy for the reaction is mainly due to the loss of entropy associated with the translational and rotational

degrees of freedom of oxygen and the formation entropies does not show significant variation among different MO_x [79]. The reduction of the TiO_2 substrate will occur when the standard heat of formation ($\Delta H^{\circ}_{f.MO_x}$) of the oxide MO_x is more negative than -$\Delta H^{\circ}_{red.}$ (standard heat of the reduction).

The next problem which needs to be addressed is the shape of the metal layer. The evaporated metal may form a continuos layer (wetting) or form clusters. The exact behavior of the metal is controlled by the surface free energy of clean substrate γ_{oxide} ,by the interfacial energy between the metal and the oxide $\gamma_{interface}$ and finally by the surface free energy of the overlayer metal γ_{metal}. By using Young's equation the mechanical equilibrium can be written as:

$$\gamma_{oxide} = \gamma_{metal}\cos(\theta) + \gamma_{interface} \tag{3.1}$$

The adhesion energy E_{ad}, which is the work needed to separate the metal/oxide interface in vacuum, can be expressed as fallows:

$$E_{ad} = \gamma_{metal} + \gamma_{oxide} - \gamma_{interface} \tag{3.2}$$

When the metal wets the surface the contact angle θ (in eq. 3.1) formed by the metal/vacuum and the metal/oxide interface will be zero and for clusters the contact angle is larger than zero. From this, the equilibrium condition can be written for vetting, because, $\cos(\theta)$ at 0 has the value of 1, the metal vets the surface if

$$\gamma_{interface} = \gamma_{oxide} - \gamma_{metal}, \qquad \text{substituting the solution for } \gamma_{interface} \text{ to eq. 3.2} \tag{3.3}$$

$$E_{ad} = 2\gamma_{interface}. \tag{3.4}$$

For thicker films, growth can proceed in a layer-by-layer fashion (Frank-van der Merwe growth mode). Particles are formed at thermodynamic equilibrium, when:

$$\gamma_{interface} < \gamma_{oxide} - \gamma_{metal}, \qquad \text{and for adhesion energy:} \tag{3.5}$$

$$E_{ad} < 2\gamma_{interface}. \tag{3.6}$$

It is possible that the metal grow via an intermediate monolayer, than due to the epitaxial strain

in thicker films clusters are formed. This is called the Stranski Krastanov (SK) growth mode. If 3D particles form without this intermediate monolayer, Volmer Weber (VW) growth occurs. The surface free energy of a clean metal is higher than that of TiO_2, therefore the left side of eq. 3.5 is negative. From this it can be seen that cluster growth should occur, unless the interface has more negative value [4]. Therefore, the strength of the metal-support interaction, the heat of MO_x oxide formation, is the dominating factor [4, 5, 78].

3.2.2 Strong metal-support interaction (SMSI) and decoration processes

The almost half-century effort for deeper understanding of the so-called strong metal-support interaction (SMSI) exhibits several turning points: (1) the detection of this phenomenon (SMSI state) appeared as the effect of an appropriate thermal treatment of noble metals supported on reducible oxides in a reductive atmosphere [80] and the connection of this state to a strongly suppressed CO chemisorption ability of the catalysts [81, 82]; (2) the observation that this state appears also in vacuum as the effect of annealing at high temperatures (600–1000 K), depending on the defect concentration in the bulk of the support oxide [81–83]; (3) the justification that the CO uptake on extended metal surfaces is determined by a simple site-blocking effect in which the coverage of the decoration oxide is proportional to the inhibited amount of adsorbed carbon-monoxide [84]; (4) the statement that this feature can be explained mainly by surface diffusion of oxygen-deficient phases of the reducible support onto the top of noble metal [83] or by formation of surface alloy or alloy oxides [82,85]; (5) demonstration of the self-limiting nature and the lateral ordering of the decoration layers detected on metal nanoparticles supported by oxide single crystal surfaces (2D model catalyst) [85–87].

It was recognized that the ordered ultrathin epitaxial oxide layers of different stoichiometries can serve as an excellent model system for the oxide-supported catalysts [88, 89]. In the present state of affairs, the biggest challenge is to explore all possible ordered decoration layers and to find connection between these structures and their chemical composition. The research devoted to this aim is carried out in two different ways: (1) epitaxial growth of oxide ultrathin films on metal single crystal surfaces as a function of oxidation conditions, listed here without a claim of completeness for TiO_x/metal single crystal systems: Pt(1 1 1) [90–94], Pt(1 1 0)-(1×2) [95], Pt(1 0 0) [96, 97], Re(1 0 1 0) [98], Rh(1 1 1) [84], Cu(1 0 0) [99], Ni(1 1 0) [100–103], Au(1 1 1) [104], Mo(1 1 2) [105, 106], Mo(1 0 0) [107], Mo(1 1 0) [108], W(1 1 0) [109], W(1 0 0) [110, 111]; (2) detection of ordered encapsulation phases on noble metal nanoparticles such as Pt [86, 87] and Pd [85] supported on

oxide single crystals. Although much effort has been made in the first direction by low-energy electron diffraction measurements, the real breakthrough was made by the application of scanning tunneling microscopy. For the studies in the second direction, scanning tunneling microscopy (STM) is the most appropriate method and is able to detect ordered phases on the surface of individual nanocrystallites.

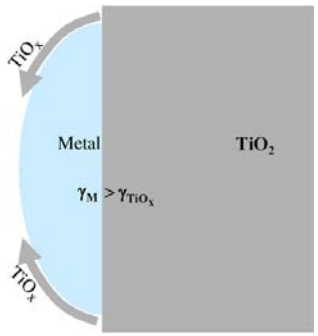

Figure 3.9: Thermodynamically minimization of the surface energy of a system is one of the main driving forces for encapsulation (from ref. [5]).

In the beginning it was proposed that minimization of the surface energy of a system is one of the main driving forces for an encapsulation reaction (Figure 3.9). This theory can work well for those metals that have higher surface energy than the supporting oxide has. Consequently, encapsulation is suspected in the case of Pt and Pd but not for Au or Ag. In addition, a support with low surface energy, for example TiO_2, will grow much more easily on top of metals than those having larger energies, such as SiO_2 or Al_2O_3 [5]. The main problem with this theory is that equilibrium conditions are supposed, however, that invokes for high temperatures in solid state reactions. Fu and Wagner gave a more complete theory that addresses the problem kinetically [5]. Based on their theory, M/TiO_2 (or in general an $M^{I}/M^{II}O_x$) systems can be divided into two distinct class by the relative position of the Fermi level, E_F, of the metal and that of the oxide. If $E_F(\mathrm{Me}) > E_F(\mathrm{TiO_2})$ than charge is transferred from the metal to the oxide and negative space charges form in the oxide. In order to minimize the electric field, E_0, the outward diffusion of O^{2-} ions is promoted (Figure 3.10A). However, in the case of the opposite scenario, in which $E_F(\mathrm{Me}) < E_F(\mathrm{TiO_2})$, the dominant diffusive process is the outward diffusion of Ti interstitial ions, Ti^{n+} (n< 4) (Figure 3.10B). This requires a metal with large work function, Φ_M, and a strongly n-type doped TiO_2 [5]. As it was mentioned already in Section 3.1, reduction of TiO_2 leads to a formation of an n-type doping level. This means that encapsulation is much more favored for heavily reduced samples.

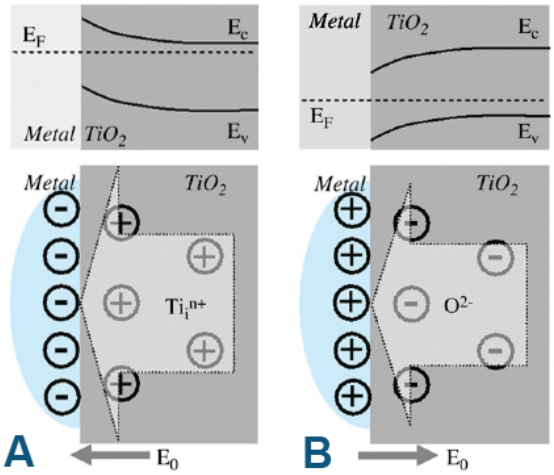

Figure 3.10: Top pannel: schematic representations of the energy bands of a metal/oxide interface in the case of $E_F(\mathrm{Me}) > E_F(\mathrm{TiO_2})$ (A) and $E_F(\mathrm{Me}) < E_F(\mathrm{TiO_2})$ (B). Bottom part: negative space charges at oxide surface regions and the electric field E_0 produced by the interfacial charge transfer process, promoting the outward diffusion of O^{2-} (A). Therefore, oxidation metal oxidation if favored. In the opposite case, promoting the outward diffusion of Ti interstitial ions, Ti^{n+} (n< 4), is the dominant process (B) (from Ref. [5]).

In Section 4.3 the results from our investigation of ordered and quasi-ordered TiO_x phases formed on the top facets of Rh crystallites supported on a $TiO_2(1\,1\,0)$ will be shown. Moreover, the effect of soft Ar^+ bombardment and restoration of the decoration layer by thermal treatments are evaluated in the light of the proposed structure of the decoration layer.

3.2.3 Interaction between alkali metals and the $TiO_2(1\,1\,0)$ substrate.

Alkali metal compounds are extensively applied as promoter additives for the preparation of catalysts and gas sensors for integrated humidity detection [112, 113]. During the last decades, most of the studies in connection of the effects of alkali metals have been focused on metal and semiconductor surfaces, such as GaAs [114]. Much less attention has been given to the interaction between alkali metals and oxide surfaces, although this type of experimental and theoretical works are very important for elucidating some important issues in the fine tuning of catalytic performance. By the application of two-dimensional metal-oxide model systems (planar catalysts), the complex effects of the additives can be efficiently studied [4]. The effect of the different additives can substantially be twofold: electronic and/or morphological. These two phenomena are often difficult to separate, since there is usually a strong interplay between them.

The influence of the pre-adsorbed potassium on the nanoscale morphology of Au deposited on $TiO_2(1\,1\,0)$ surface was perviously investigated [115]. It was found that the surface K sensitively

affects the particle formation of gold. At room temperature, gold exhibits higher dispersity in the presence of K, however, above 500–600 K a very intensive aggregation of the gold particles takes place, especially for higher K coverages (1–2 ML). Supported Au-catalysts presents high activity in the low temperature oxidation of CO, consequently, a tremendous work has been done for understanding of this reaction in detail and for the development of more efficient gold catalysts [105, 116, 117].

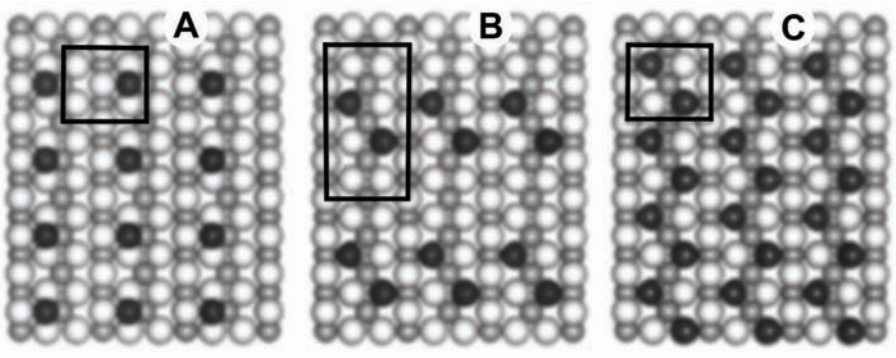

Figure 3.11: Possible structures of adsorbed K atoms on a $TiO_2(1\,1\,0)$ slab: (a) Hollow site (b) zigzag dimers (c) zigzag chain. Black spheres: K; dark spheres: Ti; grey spheres: O. (From Ref. [118])

The alkali adatoms prefer to sit in specific surface sites offered by the oxide lattice and due to the strong oxygen affinity of the deposited alkali metals, the evaporated metal growth via an intermediate monolayer, than at higher coverages clusters starts to form (Stranski-Krastanov growth mode) [78]. In the case of $TiO_2(1\,1\,0)$, alkalies prefers the adsorption position formed by three-fold O coordination sites and both between (hollow) and adjacent cites can be occupied depending on the coverage [5]. Generally, at higher coverages hallow sites are dominating due to the lateral interaction between the alkali adatoms [119]. In the case of potassium, the formation of a strong K−O bond and the reduction of the support were deduced from photoelectron spectroscopy measurements [120–126]. Although the presence of the Ti^{3+} species was detected by UPS and the correlation between the Ti^{3+} intensity and K coverage was also evidenced, direct observation by the surface sensitive metastable impact electron spectroscopy (MIES) of Ti^{3+} species failed. This phenomenon was explained by the delocalization of the transferred charge and the observed K induced enhancement of the Ti^{3+} signal is correlated with a decrease of the surface work function [127]. The screening of surface phonon modes detected by HREELS also supports the idea that potassium forms oxide species at room temperature at K coverages above 1 ML [123]. These experimental observations were studied and explained also by theoretical calculations [118, 119, 124, 127, 128]. Thermal desorption of K and Cs on $TiO_2(1\,1\,0)$ surface was also investigated in

detail [129, 130]. Moreover, atomic scale studies by STM and AFM methods were also performed in several cases for alkali metal atoms adsorbed on $TiO_2(1\,1\,0)$ surfaces [115, 126]. In harmony between experimental measurements and theoretical calculations, the main conclusion of these studies was that K adsorbs preferentially in threefold hollow sites formed by two bridging and one in-plane oxygen atoms of the substrate (see Fig. 3.11). Furthermore, the increase of the coverage results in a decrease of the bonding energy between potassium and the substrate, as a consequence of the repulsive interaction between the K ions. At the same time, this interaction cannot prevent the formation of K-covered islands, especially at lower coverages. All of these results strongly suggest that the electronic and morphological effects combine strongly and it should be taken into account in the interpretation of any special phenomenon related to alkali additives.

In Section 4.2 the effect of coverage and annealing temperature on the morphology of K deposited $TiO_2(1\,1\,0)$ surface are studied mainly by scanning tunneling microscopy (STM). In addition, some thermal desorption spectroscopy (TDS) and Auger-electron spectroscopy (AES) results are also presented. The discussion concentrate only for coverages below 1 ML, in other words, for the wetting layer of potassium.

3.3 The Si(1 1 1)–7×7 surface

3.3.1 Bulk and surface properties

Silicon crystallizes in a diamond (face-centered) cubic crystal structure, presented in Fig. 3.12, with a lattice constant 5.43 Å. It has melting points of around 1.650 K. Silicon is a semiconductor descried with a negative temperature coefficient of resistance, that means, the number of free charge carriers increases with temperature. The choice of the facet in this theses is the Si(1 1 1)–7×7 because it is well characterized and in fact it is very easy to prepare the surface reproducibly with very small defect concentration. The latter one can be contributed to the fact that silicon is mass produced with very high cleanness due to its massive usage for electrical devices. These make the surface ideal for investigations of surface/adsorbate interactions.

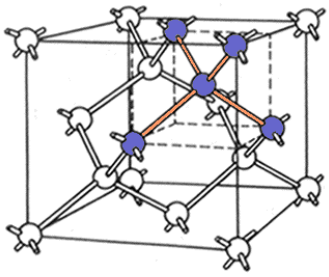

Figure 3.12: Diamond (face-centered) cubic crystal structure of the silicon.

The LEED pattern of the Si(1 1 1)–7×7 structure was observed already in 1959 [131]. However, the structural composition of the surface had been on the table for decades, before Takayanagi *et al.*. first appropriately characterized the 7 × 7 reconstruction as a Dimer-Adatom-Stacking fault (DAS) structure (shwon in Figure 3.13) in 1985 [132, 133]. Each 7 × 7 unit cell is divided to two halves; the faulted and the unfaulted sub-unit cells. The topmost layer of the cell, is made up 12 adatoms which are categorized as either corner or center adatoms. The second layer consist 6 rest atoms laying about 1 Å beneath the first layer. Each adatom and rest atom has a one dangling bond. The corner hole atoms are 4.4 Å below the first, adatom layer and they also have a dangling bond. In total, the reconstructed 7 × 7 has 19 dangling bonds. For comparison, the unreconstructed 1 × 1 surface would have 49 dangling bonds in the same area. Finally, the last layer of the 7 × 7 is called dimer layer. In addition to the complex structure, there are charge transfers within the unit cells. Firstly, from the adatoms to the rest atoms and to the corner hole atoms which results in doubly occupied dangling bond states on these atoms. Secondly, there is

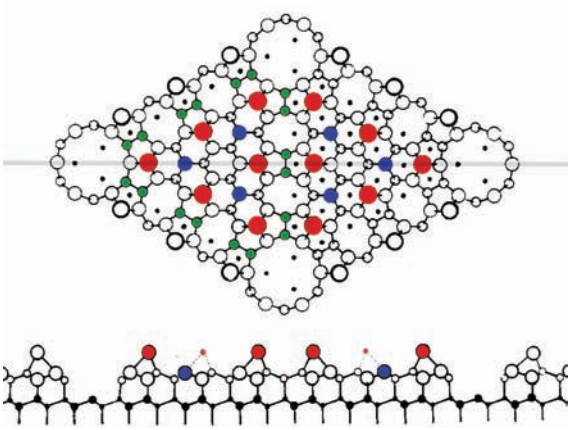

Figure 3.13: Dimer-Adatom-Stacking fault (DAS) model of the 7x7 structure proposed by Takayanagi *et al.* [132, 133]. The red circles are corresponding to the adatoms, the blue circles are the rest atoms, and green circles are representing the dimer atoms. The cross sectional view on the bottom is taken along the long diagonal of the unit cell. The stacking fault layer is in the left triangular subunit.

charge transfer from the unfaulted to the faulted half of the unit cell, resulting in a difference in electronic structure. As a consequence, different STM contrasts are observed; the faulted half of the unit cell appears brighter or higher in occupied states images and the rest atoms are not visible in empty state scans.

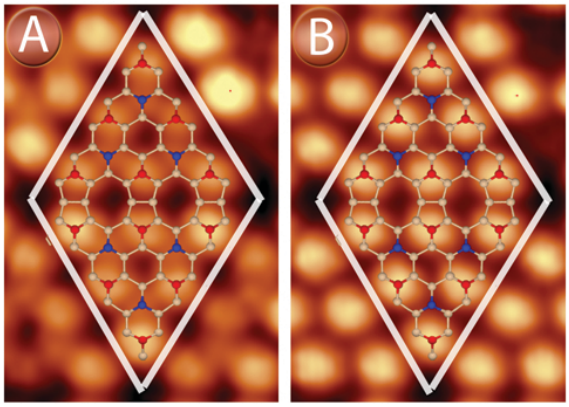

Figure 3.14: Constant current of 0.64 nA STM image of a Si(1 1 1)–7×7 unit cell with a bias voltage of −1 V (A) and +1 V (B). For better identification, the structure is also shown. Due to the charge transfers within the unit cell, the rest atoms (blue circlers) only observed in filled state scans (negative bias) and also the faulted half of the unit cell appears somewhat brighter with these scanning condition. In empty state images only the adatoms (red circles) appear.

3.3.2 Reaction with ethylene

So far in this theses only the adsorption process of metal particles were considered, in this part an example will be given for a molecular adsorption mechanism, particularly the adsorption of ethylene on Si(1 1 1)–7×7 will be considered.

Ethylene serves as an invaluable "model system" in the study of adsorption on metal surfaces because it is a simple unsaturated, nonaromatic molecule. Among the metal surfaces that have been investigated, the Ni(1 1 0) surface has attracted the most attention: although Ni(1 1 0) has been studied from a number of complementary perspectives [134, 135], there has been a particular focus on the adsorption-induced changes in the valence band region. Moreover, these adsorption studies have also been extended to the low-index semiconductor surfaces because of the importance of supported SiC, diamond films, and their chemical vapor deposition. In the case of Si(0 0 1)–2×1, several theoretical studies have sought to understand both the atomic and the electronic structure of the adsorbed system [136–139]. However, because of the complexity of the Si(1 1 1)–7×7 surface reconstruction and the highly reactive nature of the same, this has turned out to be a highly nontrivial task.

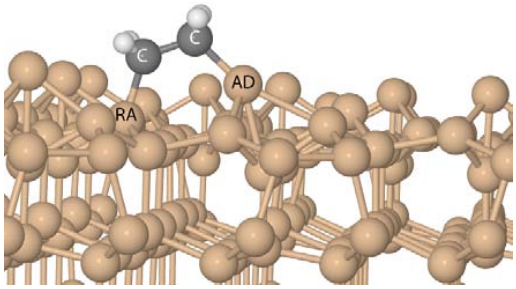

Figure 3.15: Ball-and-stick model representing the adatom–restatom adsorption configuration.

One of the first studies of ethylene adsorption on Si(1 1 1)–7×7 was performed by Klimesch and coworkers [140]. They proposed that the ethylene most probably adsorbs without dehydrogenation and found that compared with metal surfaces the dehydrogenation takes place at much higher temperature suggesting a strong and stable adsorption(chemisorption) mechanism. Further experiments with electron energy loss spectroscopy (EELS) demonstrated that the ethylene is predominantly adsorbed nondissociatively at room temperature and the C has a hybridization state that is close to sp^3, indicating an additional adsorption mechanism [141]. Piancastelli *et al.*. reported a scanning tunneling microscopy (STM) experiment where ethylene exposures caused surface atoms to "disappear" and also introduced change in the local density of states around the

Fermi level [142]. This tendency was observed not only on the surface atoms directly involved in the adsorbate–substrate bonds but also on some of the neighboring atoms. On the basis of their observations, they proposed an adsorption model, where the molecule bridges an adatom and an adjacent restatom (see Figure 3.15).. Similar observation had been reported before for the acetylene molecule, and it had been suggested that this adsorption scheme is common for other unsaturated molecules on 7×7 [143]. The fact that the adatoms and the restatoms are involved in the adsorption process was subsequently proved in a photoelectron spectroscopy (PES) study, where after depositing C_2H_4, the intensity corresponding to surface states simultaneously decreases in both the valence band and in the Si 2p core level spectra [144].

Until now, only Rochet and coworkers disagreed with the suggested adsorption process described above [138]. On the basis of their combined LEED and PES experiment, an alternative adsorption mechanism was proposed involving the reconstruction of the 7×7 unit cell. This alternative mechanism would allow many more molecules to be adsorbed in a unit cell than was proposed in the adatom–restatom theory. The idea of adsorption-induced reconstruction was supported later also by Kim *et al.* [145]. From the Si 2p core level analyses, they also claimed that there are other adsorption sites involved in addition to bridging sites. Moreover, a similar configuration to the proposed one for the adsorption of acetylene (coupled-bridge) on the 7×7 surface [146] must be considered for ethylene as well.

Interestingly, there is only one theoretical paper so far concerning the adsorption of ethylene on the Si(1 1 1)–7×7 surface. Lu and coworkers published a detailed study of the cycloaddition-like reaction with small Si clusters representing the Si(1 1 1)–7×7 for several molecules including ethylene [147]. Their calculation did not show any intermediate or transition state along the reaction pathway supporting the previously accepted adatom–restatom adsorption model. In addition, they found that the substrate reconstruction has very low probability. The conclusions of this study depend critically on the degree to which the cluster, or unit-cell fragment, reproduces the behavior of the 7×7 unit cell.

Because of the recent discussion about the validity of the adatom–restatom model for the adsorption of ethylene on the Si(1 1 1)–7×7 surface, the adsorption of ethylene from low coverage until the saturation coverage when all bridging sites are occupied will be examine in details further in Section 4.5. It will be shown that in some case only a complex analyses, which involve the combination of different techniques (DFT, STM, AFM, PES), can predict the proper adsorption mechanism.

"The strongest of all warriors are these two — Time and Patience."

Leo Tolstoy, War and Peace

4

Results and discussion

4.1 Experimental details

The experimental results presented in this thesis has been collected using two UHV systems equipped with STM/AFM heads and several other surface analyzing tools. In addition, there were several possibilities to perform research at the Materials Science Beamline at the Elettra synchrotron light source in Trieste, Italy. The photoelectron spectroscopy results were obtained in that beam-line.

4.1.1 Experimental setups

Materials Science Beamline

The photoemission experiments were performed at the Materials Science Beamline at the Elettra synchrotron light source in Trieste. The beamline is equipped with a plane grating monochromator providing synchrotron light in the energy range of 40-800 eV, a Specs Phoibos 150 hemispherical electron energy analyzer, a low-energy electron diffraction (LEED) optics and a dual-anode X-ray source. During the experiments, the base pressure in the main chamber was in the low 10^{-10} mbar range. Furthermore, the chamber contains quadrupole mass spectrometers allowing the determination of the inserted gas purity. The Si 2p core level spectra were recorded at 150 eV of photon energy in normal emission geometry (NE, incidence/emission angles of $60^{\circ}/0^{\circ}$ and normal incidence geometry (NI, incidence/emission angles of $0^{\circ}/60^{\circ}$) with total energy resolution

(both analyzer and beamline) of 0.15 eV. The C 1s XPS spectra were collected in the same geometries, and the photon energy and the total resolution were 330 and 0.45 eV, respectively. The valence band spectra were measured with the same Phoibos analyzer using angular resolution of 2° and total energy resolution of 50 meV; spectra were measured in the interval between NE and NI with a step of 6°. The photon energy was 45 eV. The binding energy (BE) was calibrated by measuring the Fermi edge. The polarization of light from the beamline has not been measured but is believed to be between 80 and 90 % linear, as the source is a bending magnet. The raw data were normalized to the intensity of the photon beam, which was measured by means of a high-transmission gold mesh and by corresponding spectra of the clean sample, and recorded under identical conditions.

System I.

The first UHV system was used mainly for characterization of the growth of various metals on $TiO_2(1\,1\,0)$–1×1 (presented in Section 4.2 and 4.3). The experiments were carried out in an ultrahigh vacuum (UHV) system evacuated down to 1×10^{-9} mbar or bellow and equipped with a commercial room temperature (RT) scanning tunneling microscope (WA-Technology, Cambridge, U.K.), a cylindrical mirror analyzer with a central electron gun (Staib Instruments, Langenbach, Germany) and a quadrupole mass spectrometer (Balzers-Pfeiffer, Asslar, Germany).

Initially, W tips were applied in the course of the STM experiments, however, because this STM system lacks on any tip cleaning tool Pt–Ir tips were also used. In fact, the head has the possibility of using high voltage (max. 200 V) for tip treatments. Nevertheless, in order to have reasonable cleaning effect with filled emission higher voltage needs to be applied from time to time and the sample must be replaced with a metal substrate to gain higher currents and avoid any damage in the model system (M/TiO_2). Due to the limited sample storage capacity, inert Pt-Ir tips appeared to be more natural choice. The Pt–Ir (80–20 %) tips were produced first by cutting the wire with a wire-cutter. The tips were then immersed to a depth of 1-2 cm in an etching (polishing) solution of $CaCl_2 \cdot 2\,H_2O$ (35 g in 200 ml distilled water and 10 ml acetone) [148]. A circular platinum ring counter electrode was immersed to the same depth as the tip and the tip was positioned in the center of the ring. An etching current of 1 A at 15 V AC was then applied across the tip wire and the counter electrode for periods of 0.25, 1, 3, and 10 s. The tips were removed from the etching solution and then washed initially in de-ionized water with a final rinse in 95 % ethanol [148].

One side epi-polished $TiO_2(1\,1\,0)$ single crystal of $5 \times 5 \times 1$ mm^3 was directly fixed to a Ta filament by an oxide adhesive (ceramobond-571, Aremco Products, Valley Cottage, NY), and it was mounted on a transferable sample holder. The probe was indirectly annealed by the current flowing through the Ta filament. Because the Ta filament heating resulted unhomogeneous heat distribution across the sample, in some cases, a Si plate with a size of $5 \times 5 \times 0.4$ mm^3 was used as heating element. Further benefit of this method is that, the oxide glue, which tends to degas heavily upon UHV annealing, is not needed. The temperature of the probe was measured by a chromel–alumel (K-type) thermocouple stuck to the side of the sample by the same oxide adhesive. It is worth noting that we have never detected any contamination due to these components, even after extended high-temperature thermal treatments of the probe.

The cleaning of the sample was started by a gradual increase of the temperature up to 1050 K (degassing) while the maximum pressure was kept in the range of 10^{-8} mbar. Upon annealing the color of the sample was changed from transparent to light blue. The pure annealing stage was continued by Ar^+ bombardment with an average current density of 4-6 μA/cm^2 at 1000 K with stepwise decreased ion energies of 2, 1.5, and 1 keV for 1-2 h. The color of the sample usually changed further into dark blue. The change of the color of the sample reflects some reduction in the subsurface layer, resulting in a more conductive sample (beneficial for avoiding charging effect during spectroscopy and microscopy measurements). To reset the TiO_2 stoichiometry, the samples were from time to time reoxidized in 1×10^{-6} mbar oxygen at 900 K till the sample became light blue or even transparent again. The final treatment was usually a short sputtering and annealing at 1050 K in UHV. Details of the $TiO_2(1\,1\,0)$ substrate are discussed in Section 3.1.

Finally, metal depositions ware carried out with a commercial getter sources (SAES) for K-deposition and the chamber was equipped with a commercial four-pocket evaporator (Oxford Applied Research, Oxford, U.K.). One of the pocket was loaded with high-purity (99.95 %) Rh rod.

System II.

The SPM measurements on $Si(1\,1\,1)$–7×7 were performed at room temperature with Omicron VT XA qPlus AFM/STM system operating at the base pressure bellow 1×10^{-10} mbar. In this experimental setup, the tunneling current is acquired with an *in vacuo* preamplifier floating on the potential of the bias voltage and the sample holder is grounded. NanoSurf EasyPLL is used for the FM demodulation and the Omicron MATRIX control system for the data acquisition.

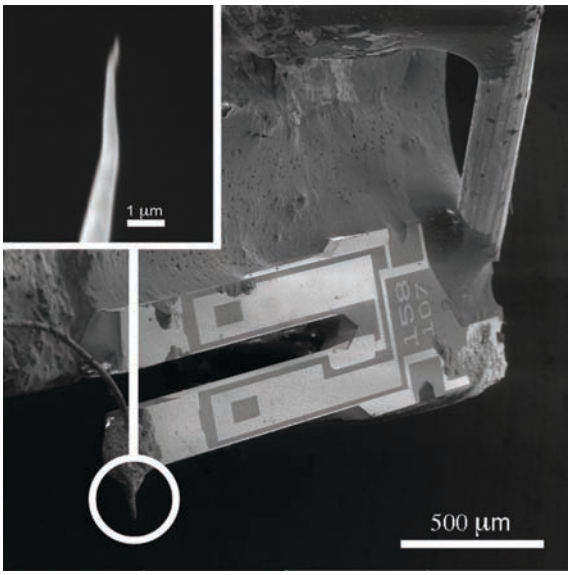

Figure 4.1: Scanning electron microscope (SEM) image of a tuning fork based (qPlus) AFM/STM sensor applied in this work.

Q-plus sensors were built from commercially available tuning forks from Micro Crystal, originally packed in the SMD package MS1V-T1K. Chemically etched tungsten tips were mounted at the end of the free pong (see Figure 4.1). The original tuning fork was shortened in order to reach higher sensitivity (charge produced by deflection) [149] which allows us to reach lower amplitudes. The interaction force between the tip and surface atoms was calculated from the measured frequency shift data by means of the Sader formula [28], which was introduced in Chapter 1. The tunneling current I_t was calculated from time-averaged tunneling current $< I_t >$ using a similar approach [150]. The chamber also contained a quadrupole mass spectrometer (Balzers-Pfeiffer), (Spot Profile Analysis-)Low Energy Electron Diffraction (Omicron) and a precision leak-valve for gas depositions.

4.1.2 Simultaneous detection of beam-deflection and tunneling current

The aim of this section is to discuss basics of so-called cross-talk phenomena, where an interference between the current and deflection channels leads to undesired modulation of tuning fork motion. It is going to be demonstrated that the modulation of the tunneling current signal due to dynamical motion of the probe may affects functionality of the current to voltage converter.

In FM-AFM mode, the sensor oscillates with the resonant frequency f_o. Decreasing the tip-sample distance the value of f_o is changed by Δf due to forces acting between the probe and the sample. If the tip and the sample are conductive, tunneling current I_t can be detected. The impact

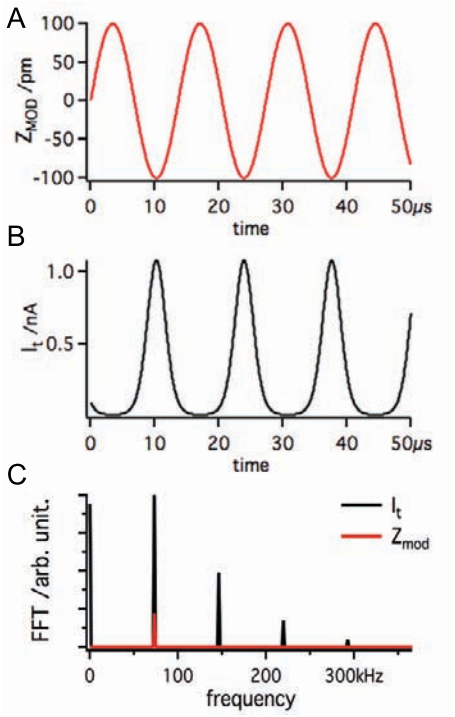

Figure 4.2: The effect of z modulation (A) on the tunneling current (B). a_{mod} = 0.1 nm and f_0 = *73180* Hz; I_t calculated by using $I_t(z)=I_0 e^{-2\kappa z}$ where κ_I=11.9 nm^{-1} and I_0 = 0.1 nA). In order to see better the frequency distribution FFT is also shown (C).

of the tip-sample distance modulation on the tunneling current is shown in Figure 4.2. Since the tunneling current depends exponentially on the tip-surface separation z as $I_t(z)=I_0 e^{-2\kappa z}$, the harmonic modulation produces sharp peaks in the current signal (Figure 4.2B). As a consequence, the frequency spectrum of the tunneling current shows higher harmonics of the modulation signal (Figure 4.2C).

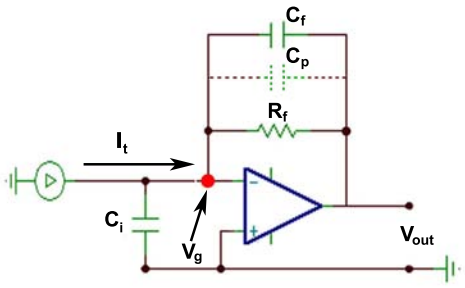

Figure 4.3: Circuit diagram of a current to voltage converter (IVC) where R_f is the feedback resistance with the parallel capacitance C_f. C_i is the input capacitance (in addition to the amplifier owns one). C_p represents the parasitic capacitance of the feedback resistor. The input of the operational amplifier is floating on the virtual ground potential(V_g)

The tunneling current I_t is converted to a voltage signal V_{out} with the current to voltage

converter (IVC). The circuit diagram of an IVC is presented in the Figure 4.3, where R_f is the feedback resistor with the parallel capacitance C_f and C_i represents the input capacitance caused by cabling. The current passing through the feedback resistor R_f induces a voltage drop that equals to the value of $R_f I_t$. Due to the potential difference between the input terminals, the operational amplifier (OPA) will change its output voltage V_{out} compensating the voltage drop to ensure zero potential difference between the input terminals. Because the inverting input is kept at the ground potential this terminal is called virtual ground. The output voltage correlated with the tunneling current will be $V_{out} = -R_f I_t$.

When working with small values of the tunneling current (order of nA) the feedback resistance R_f must be high enough to get a reasonable value for the output voltage. However there is a side effect of high gain operation. The frequency response is strongly reduced as the gain is inversely proportional to the bandwidth. In such regime, the feedback capacitor C_f plays an important role in the circuit reducing the gain at high frequencies (i.e. eliminates instabilities and prevents self-oscillations). In a real circuit, the parasitic capacitance C_p across the large feedback resistor R_f ($\approx$ 100 MΩ) is in the range of a pF that fully covers the function of the feedback capacitor C_f. Therefore, we will consider only the parasitic capacitance C_p in the rest of the discussion.

For circuit analyses, numerical simulations were performed with a simple to use SPICE-based analog simulation program TINA-TI [151]. The frequency response of the IVC is shown in Figure 4.4A. For calculations, the macro model of Op111 was used with parameters R_f = 100 MΩ, C_p= 1 pF and C_i =10 pF. The latter one, C_i, corresponds to the capacitance of $\sim$10-15 cm long coaxial cable (depending on the exact type of the cable) making connection between the tip and the input of the op-amp [152].

As already mentioned, the voltage drop will appear on the inverting input of the OPA. The OPA will counteract by producing the same voltage on the output, but with different sign to keep the differential voltage zero between the input terminals. As it can be seen form Figure 4.4A the output voltage V_{out} varies with the frequency. In terms of currents, the output voltage can be better expressed as $-R_f I_t/(1+2\pi f R_f C_p)$ [153]. At small frequencies, the term $2\pi f R_f C_p$ is negligible and the original expression for the output voltage $V_{out} = -R_f I_t$ is recovered. For the frequencies higher than the first frequency pole $f_1 = 1/(2\pi R_f C_p)$ (in our case f_1= 1.6 kHz) the amplifier gain drops -20 dB/decade being proportional to $1/f$. In this regime, the amplifier behaves as an integrator circuit and the value of C_p becomes dominant. The voltage at the capacitor equals to the charge q on the capacitor divided by its capacitance, therefore $V_{out} = q/C_p$. Because the

output voltage V_{out} is proportional to the charge it is also called a charge amplifier. The charge amplification breaks at the second pole in the frequency response (f_2) which is around 110 kHz in this particular example setup.

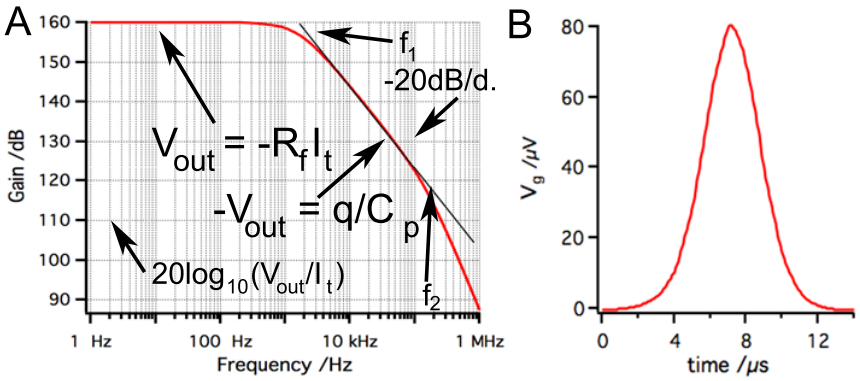

Figure 4.4: a) Frequency response of the IVC presented in Fig. 4.3. The following parameters were used to simulate R_f = 100 MΩ, C_p= 1 pF and C_i =10 pF. b) the effect of the tunneling current presented in Figure 4.2 on the virtual ground

The optimal function of IVC is guaranteed as long as the value of the virtual ground potential V_g is held at the ground potential. V_g is kept constant by varying the output voltage V_{out}. The slew rate of OPA determines the maximum speed at which the output voltage can change. For sinusoidal changes given with $V_{out} = V_{out}^{peak}\sin(2\pi ft)$ the slew rate must exceed

$$\frac{dV_{out}}{dt} = 2\pi f \cdot V_{out}^{peak}\cos(2\pi ft), \tag{4.1}$$

with the maximum value at t=0:

$$\left(\frac{dV_{out}}{dt}\right)_{max} = 2\pi f \cdot V_{out}^{peak}. \tag{4.2}$$

For the resonant frequency of the tuning fork 73180 Hz and the output voltage of 1 V the maximum speed (dV_{out}/dt) is 0.46 V/µs. The maximum slew rate of Op111 is 2 V/µs which means that optimal operation of the IVC is ensured for output amplitudes $<$ 4.3 V at the given frequency. As it was already shown in Figure 4.2, the tunneling current during dynamic AFM measurements contains much higher frequency components than the resonant frequency of the tuning fork. Therefore the OPA may not be able to keep the virtual ground (gap voltage) constant with high precision due the speed limit of the amplifier. When data from Figure 4.2 are used for simulation of the circuit function, V_g shows oscillations with peak amplitudes $V_g^{peak} \approx 80\mu V$.

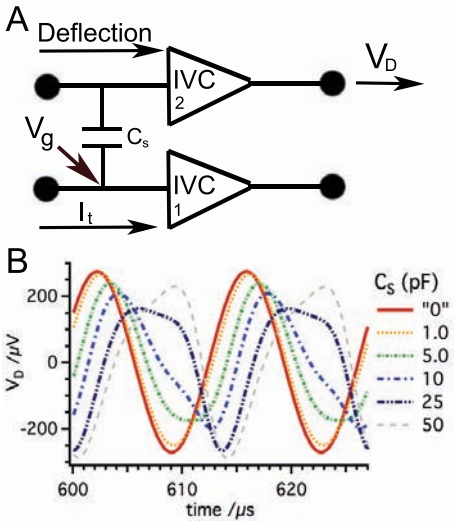

Figure 4.5: The coupling between the deflection and the tunneling current channel is established by the stray capacitance C_s (A). To show the effect of the cross talk, signals shown in Figure 4.2 were used as input values for the amplifiers. The signal in the deflection channel is altered significantly on the output V_D for C_s values exceeding 1 pF (B).

The modulated potential in the current channel may interfere with the input signal of deflection channel. The coupling of the channels is driven by the stray capacitance C_s (see Figure 4.5). To demonstrate how the crosstalk affects the deflection signal we analyzed the configuration shown in Figure 4.5. To simplify the electric circuit identical, amplifiers were used in both channels (Figure 4.3). For the given resonant frequency f_o=73180 Hz the amplifier operates in the charge amplifier regime (see Figure 4.3). To simulate the output from the deflection channel close to our experimental conditions, 3 µC/m sensitivity was used for the sensor [16]. The transmitted signals, shown in Figure 4.2, were used as input values of the amplifiers in the simulation. Using 100 pm deflection amplitude with 1 pF of the capacitance C_p we obtain the output voltage value approx. to 300 µV .

If the input terminal of the amplifier in the deflection channel is held at the ground potential, the current I_{C_s} due to the stray capacitance between the channels can be expressed as:

$$I_{C_s} = C_s \cdot (dV_g/dt). \tag{4.3}$$

Hence the maximum current $I_{C_s}^{max}$ is defined (using eqn.4.2 for V_g instead of V_{out}):

$$I_{C_s}^{max} = 2\pi f C_s V_g^{max}, \tag{4.4}$$

where the V_g^{max} can be estimated by circuit simulations. From eqn.4.4 we immediately see, that

the maximal current $I_{C_s}^{max}$ (or in other words the degree of the cross-talk) depends on the value C_s as well as on the resonance frequency f_0 and the maximal amplitude of the ground potential oscillation V_g^{max}. V_g^{max} depends also on the frequency f_0, the oscillation amplitude A and the characteristic decay length κ_I of the tunneling current. Therefore the crosstalk can be enhanced when the sensor is operated at high frequencies. Figure 4.5 shows that the signal in the deflection channel appear altered significantly on the output V_D for C_s values exceeding 1 pF. In case of the stray capacitance of 5 pF the crosstalk causes the decrease of the initial value of V_D 273 µV to 250 µV with 6.8° phase shift. Note here, that by inverting the sign of the bias voltage the result will be different and even larger oscillation signals can be detected.

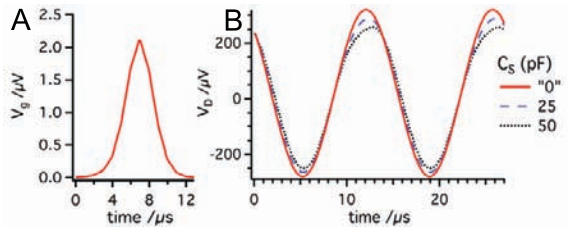

Figure 4.6: If the slow Op111 is replaced by a faster OPA, Op637 the modulation of the virtual ground V_g^{peak} can be significantly reduced (by a factor of 40) (A). Consequently, the signal in the deflection channel is altered at much higher C_s values (B)

Together with C_s the crosstalk depends also on the speed of the amplifier response. It was shown that the virtual ground is modulated when the amplifier response is too slow. The same analysis was done with Op 637 instead of Op111. The Op637 has much higher slew rate ($\approx$ 50 times). The results show that the modulation of the virtual ground is reduced by a factor of 40 (Figure 4.6A). As a consequence, the crosstalk appears at much higher values of C_s (Figure 4.6A).

In conclusion, it was shown that the crosstalk between the current channel and the deflection depends mainly on two parameters: (i) the stray capacitance C_s between the channels; (ii) the resonance frequency f of the sensor. The cross-talk alters the detected oscillation amplitude and its phase. The amplitude regulator tends to suppress the artificial oscillation amplitude leading to appearance of "dissipation" signal. That can have both positive and negative value. Finally, special attention has to be paid when the tuning fork is used in higher harmonics or higher flexural modes because the harmonic modulation of the tunneling current can appear in the deflection signal due to the coupling between the channels.

4.1.3 Modified experimental setup for simultaneous current and force detection

In a joint project with Omicron Nanotechnology, we evaluated the crosstalk in the qPlus sensor. We suggested several improvements in order to keep the capacitive couplings as low as possible. First we modified the construction of the sensor. Originally, one of the electrodes of the tuning fork was connected to the deflection amplifier and the second electrode was used for detection of the tunneling current. The tip was glued directly to the electrode. This arrangement of electrodes can lead to self excitations by the AC component on the virtual ground potential at the I_t detection path. The capacitance between the electrodes of the tuning fork acts as a coupling capacitor.

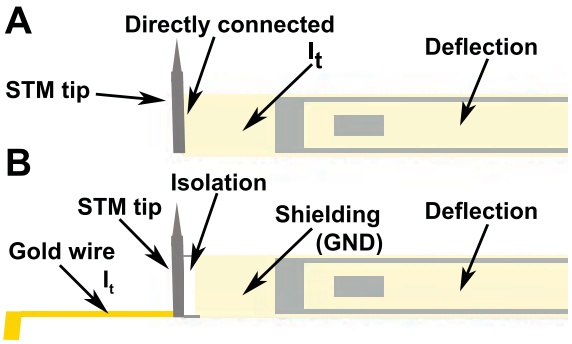

Figure 4.7: Original connections where one of the electrodes of the tuning fork was connected to the deflection amplifier and the second electrode was used for detection of the tunneling current (A). To reduce the capacitance between the channels and eliminate any possibility of self-excitation.The tip is connected by a separated gold wire to the IVC and the electrode originally used for the tunneling current is grounded now. The wire and the tip is electrically isolated from the rest of the fork (B).

In the new sensor design, the tip is connected with a separate wire (0.25 µm gold) to the OPA for the current channel. The measurement of the tunneling current via separate wire was also reported by other groups [36, 154, 155]. The electrode originally used for detection of the tunneling current is grounded to create a shielding electrode (see Figure 4.7). The gold wire and the tip on the active prong have to be electrically isolated from the quartz of the prong to avoid self–oscillations of the sensor.

We found that the original ceramic support of the tuning fork with printed wiring increases the capacitance between the tunneling current and the deflection channels. We replaced the ceramics with a metal plate connected to the ground potential. The electrodes of the tuning fork and the tip itself are directly connected to the connector pins. The metal plate works now as an extra shielding between pins used to connect the current and deflection channels. The modified wiring on the ceramics support with grounded metal plates on both sides shows similar electrical properties

as a fully metallic support could. Beside the modifications in the sensor design, we replaced the internal coaxial cable making connection between the tip and the tunneling current amplifier with double shielded one and also the sensor reception stage got altered to reduce even further the stray capacitance. Morover, as it was already mentioned the sensitivity of the sensor can be increased by shortening the tuning fork. The higher deflection signal reduce the impact of the cross-talk at given amplitude compared to sensors having the original length and lower amplitudes can be reached. Let us note that collecting the tunneling current on the sample side with carefully designed internal wiring can be an alternative option for several microscopes. In Section 4.4 the proper working mechanism of the microscope will be demonstrated on the prototypical Si(1 1 1)–7×7 surface.

4.2 Adsorption of potassium on TiO_2(1 1 0)

4.2.1 AES and STM detection of K adsorption on TiO_2(1 1 0)

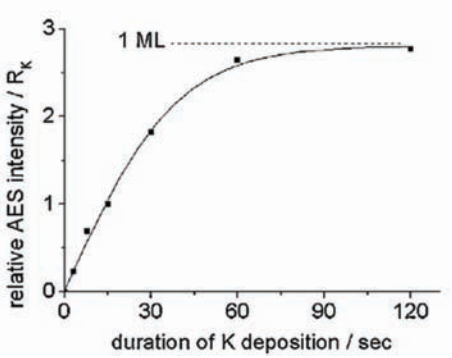

Figure 4.8: Change of the relative AES intensity, $R_{\mathrm{K}} = \frac{I_{\mathrm{K-252\ eV}}}{I_{\mathrm{Ti-385\ eV}}}$, as a function of the duration of K deposition at 330 K

Potassium was deposited on a clean TiO_2(1 1 0)–1×1 surface exhibiting bulk terminated atomic positions (see STM imaging below) and Auger peaks characteristic of Ti and O. During the deposition, the temperature was kept slightly above room temperature (330 K). The potassium deposition was followed by measuring the peak-to-peak values of K(LMM) at 252 eV and Ti(LMM) at 385 eV on AES curves ($^{\mathrm{d}N}/_{\mathrm{d}E}$) and by determining their relative intensities R_{K} (Fig. 4.8). It can be seen that in the function of the duration, R_{K} increases almost linearly up to 1 and asymptotically reaches a saturation value of approximately 2.80 after 120 s deposition. This curve-shape depends naturally on the heating current used for the K-source and this duration-dependence was fixed during this work by tuning the heating current from time to time. The amount of deposited potassium at 330 K, the value of R_{K} (≈ 2.8) corresponds to one monolayer coverage ($\theta_{\mathrm{K}} = 1$ ML) in this work.

Up to one monolayer, the peak-to-peak Auger-signal corresponds well to the surface concentration of K. Naturally, measuring reproducibly absolute intensities are experimentally much more difficult than to determine the relative intensities. However, the relative intensities (R_{K}), mainly because of the shadowing effect, correlate only roughly with the surface concentration of potassium. Nevertheless, based on all the previous studies, potassium shows strong preference for the hollow adsorption sides. If adsorption positions are uniform, electrons collected and emitted by Ti atoms are uniformly shaded, scattered. If it is so, assuming that the value of R_{K} shows linear dependance with the coverage is straightforward.

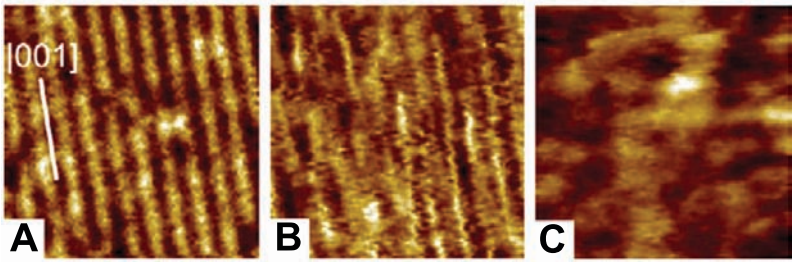

Figure 4.9: Characteristic STM images of 7×7 nm^2 recorded on (A) clean TiO_2(1 1 0)–1×1 and covered by (B) 0.09 ML, (C) 0.55 ML of potassium.

The saturation of the potassium adlayer was followed also by recording STM images. Fig. 4.9 shows the characteristic images (7×7 nm^2) of clean (a) and K covered surfaces of 0.09 ML (b) and 0.55 ML (c). The clean surface exhibits dark and bright lines running in parallel with a distance of 6.5 Å. This morphology is characteristic for 1×1 (for more details see Section 3.1.2) At $\theta_K = 0.09$ ML, elongated dark islands appear at the place of the bright rows (Fig. 4.9B). This behaviour is in harmony with the earlier observations presented for low K-coverage [126]. In the case of 0.55 ML coverage the dark pits and white dots constitute a rather unordered surface structure (Fig. 4.9C), although larger scale images (not shown here) indicate some ordering in the [0 0 1] direction. For even higher K-coverages, the surface exhibited only strongly disordered structures. However, due to the charge transfer from the K atoms, states accessible for tunneling electrons are more and more removed as the coverage increases. As a consequence, STM imaging and solid interpretations based on them are difficult at hight coverages. AFM is a better choice for studies as it was used by Pang *et al.* [126]. Unfortunately, they presented images only for very low coverages (0.03 ML).

4.2.2 AES and TDS measurements

In this series of experiments, TiO_2(1 1 0) surfaces were initially deposited by different amount of potassium at near room temperature (330 K) and were subsequently annealed for 2 min at elevated temperatures between 300 K and 1100 K. Auger-electron spectroscopy measurements plotted in Fig. 4.10A were performed for three initial K coverages: $\theta_K = 0.35$ ML ($R_K = 1.00$), $\theta_K = 0.65$ ML ($R_K = 1.82$) and 0.99 ML ($R_K = 2.77$). The change of the relative AES intensities indicates that after a slight decrease between 300 K and 500 K, a significant and gradual loss of the K signal can be detected between 500 K and 900 K for each probe. The curves show that the higher the coverage the lower the temperature where the maximum rate of the potassium loss appears. For example, in the case of the lowest initial coverage ($R_K = 0.35$), the decrease of the

K signal begins only above 700 K. The reason for this behavior is that the local dipol moment of the alkali-metal-substrate complex decreases smoothly with the coverage in the first ML, due to the lateral repulsive forces between dipoles. As a result, the heat of adsorption is decreasing with the coverage [130], with the heat of adsorption also the barrier for desorption will decrease as well. It can also be seen that all the three curves approach a similar value ($R_{\mathrm{K}} = 0.10$) in the range between 900 K and 1100 K. This means that it is impossible to entirely clean the surface from K by a few minutes annealing at 1100 K. It is worth remarking that to remove all potassium, the surface had to be bombarded by Ar^+ ions and annealed for a few minutes at 1100 K.

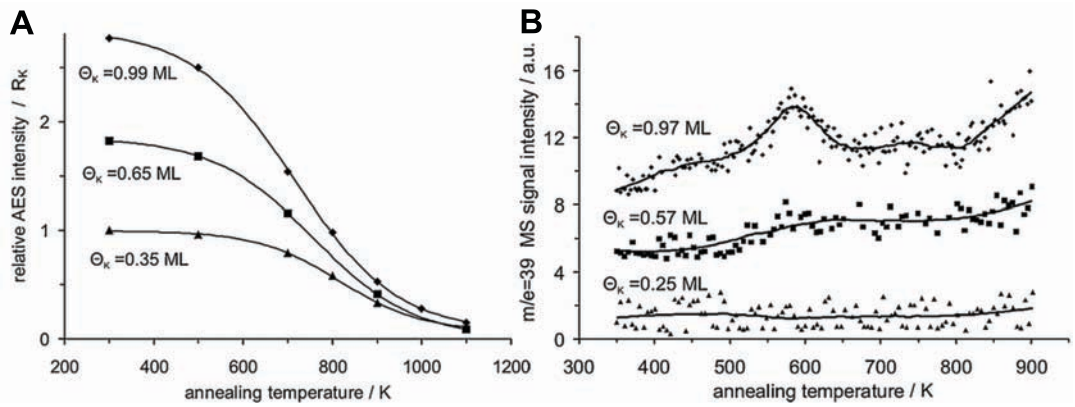

Figure 4.10: (A) Change of the relative AES intensity (R_{K}) as a function of the annealing temperature for three initial K coverages; (B) thermal desorption curves (TDS) of K recorded at $m/e = 39$ for different initial K coverages (heating rate is 2 K/s).

The thermal desorption curves recorded for $m/e = 39$ mass spectrometer (MS) signal (characteristic of atomic K) after the deposition of different amount of K at near room temperature (330 K) are presented in Fig. 4.10B. The heating rate of 2 $\mathrm{K\,s^{-1}}$ was applied in each case. The temperature range of the plots is limited to 900 K because the MS signal increases very intensively (especially for higher K coverages) above this temperature. We assume that this behavior is due to the desorption from the sample holder or to the appearance of K ions among the desorbing species. For 0.25 ML (or less), the MS signal of $m/e = 39$ shows a very small feature at around 450 K and above 800 K. More pronounced desorption traces appear for $\theta_{\mathrm{K}} = 0.57$ ML and $\theta_{\mathrm{K}} = 0.97$ ML initial coverages. These latter curves are peaked at around 550 K and 900 K and smaller desorption features appear at 400 K and 750 K. The wide temperature range is a typical feature of alkali metal desorption from different metal and oxide surfaces and can be explained by a gradual decrease of the activation energy (bonding energy) with the coverage. It is worth to note that the region around 550 K for the initial K coverage higher than 0.5–0.6 ML can be ascribed to simultaneous desorption of CO_2 and K due to decomposition of some surface K_2CO_3 contam-

ination. Some C contamination of the K adlayer was also detectable in the range of 0.5–1.0 ML by Auger-spectroscopy. We have looked for other desorption species like KO, K_2O, KO_2, O_2 and K_2TiO_3. It was found that a weak intensity KO desorption can be detected in the temperature range of 800–900 K for higher K coverages.

4.2.3 Morphological characterization by STM

As mentioned above, in the case of low K coverages ($\theta_K < 0.2$ ML), annealing up to 900 K causes only a moderate change in the relative AES signal intensity of K. In contrast to this stability, STM images indicate substantial morphological changes of the atomic terraces: the terrace edges became lacy and small dots of 1–2 nm appear on TiO_2(1 1 0)–1×1 surface exposed to 0.09 ML potassium at 330 K and annealed at 900 K for 2 min (Fig. 4.11A). Further annealing at 1000 K for 2 min results in straight line edges, at the same time the terraces are covered with quasi rectangular or slightly elongated clusters (Fig. 4.11B). The concentration of latter species decreases on the effect of annealing at 1100 K for 2 min (Fig. 4.11C). Supposing that these clusters can be identified with nanoparticles containing K, their disappearance is in good harmony with the gradual decrease of θ_K (see Fig. 4.10A) in this temperature range. For the bulk reaction, it can be written

$$K(s) + 2\,TiO_2(s) \longrightarrow K_2O(s) + Ti_2O_3(s)$$

where the formation enthalpy of K_2O is $H^\circ_{f,K_2O} = -362$ kJ/mol [130] and the reduction of TiO_2

$$2\,TiO_2(s) \longrightarrow Ti_2O_3(s) + \tfrac{1}{2}\,O_2$$

$$\Delta H^\circ_{red.} = \Delta H^\circ_{f,Ti_2O_3} - 2\Delta H^\circ_{f,TiO_2} = 368 \text{ kJ/mol}.$$

Therefore, the formation of K_xO or K_xTiO_y (potassium metatitanate) top layer complexes can be thermodynamically favored. From this fact it can be concluded that these nanoclusters consist of some surface K compound, which – instead of agglomeration into larger crystallites – disappears (desorb from the surface or diffuse into the bulk) in a relatively slow process. The insert of 7×7 nm^2 in Fig. 4.11C (top left) exhibits a typical island with a height of 0.2 nm.

A similar deposition/annealing experiment was also performed for a K coverage of 0.36 ML (Fig. 4.12). The surface structures obtained after different K depositions at near room temperature have already been presented above (Fig. 4.9). The STM image of 50×50 nm^2 in Fig. 4.12A shows

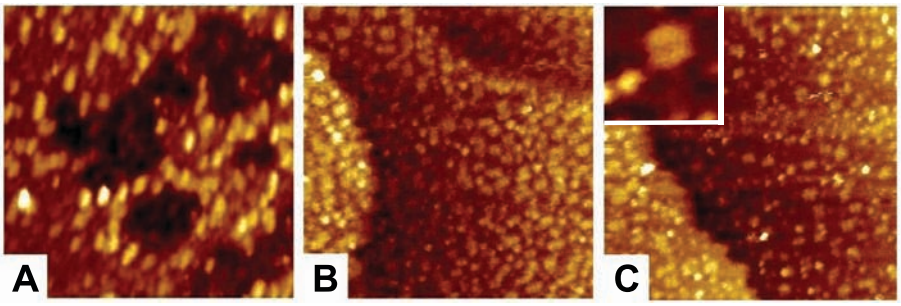

Figure 4.11: STM images (50×50 nm^2) recorded on K deposited (0.09 ML) $TiO_2(1\,1\,0)$ surface annealed at (A) 900 K, (B) 1000 K and (C) 1100 K for 2 min.

a characteristic surface morphology appearing after a thermal treatment at 700 K in UHV for 2 min. Some ordering of the surface in the [0 0 1] direction can obviously be seen, nevertheless, the general morphology of the surface refers to some "etching" process. The average periodicity of the deep and the protruding rows is approximately 5 ($\pm$0.5) nm and the variation of the height is 0.3–0.4 nm. Further annealing at 900 K results in agglomeration of the islands without any significant change of the average surface corrugation of 0.5 nm (the Z-distance between the lowest and the highest point of the image) (Fig. 4.12B). It should be remarked that in accordance with the AES measurements presented in Figure 4.12A, this is the temperature regime where the largest K loss appears. This treatment results in the appearance of a completely new ordering: 1 atomic layer deep leaky terraces and almost fully periodic arrangement of [0 0 1] direction on the atomic terraces decorated by some outrising nanodots. The lateral distance between the rows is 1.3 nm measured on the 7×7 nm^2 image which corresponds unambiguously to a 1×2 reconstruction (bottom middle insert in (Fig. 4.12B). This structure was already discussed in details Section 3.1.2. The fact that the surface is almost completely transformed into 1×2 reconstruction, suggests a stoichiometric removal of oxygen. However, the stoichiometry of the remaining Ti rich layer varies among the described models. One one hand, removing one oxygen atom from every second unit cell of the support ($2\,TiO_2 = Ti_2O_3 + O$) leads to the formation of Ti_2O_3 "added" layers suggested by Onishi and Iwasawa [61, 63]. On the other hand, the reversible transformation between the 1×1 and 1×2 presented by Park et. al. (Figure 3.8) can be an alternative option and in fact the Park model gives better explanation for the reversible transformation. Even though, the latter model got strong support recently [75], there is no sufficient information for us here for making clear justification. The other surprising result is that one atomic deep terrace pits are formed in 20–30 % of the layer. This latter feature can tentatively be explained also by the removal of Ti from the surface layer what suggests a desorption of both $K-O_x$ and $K-Ti_xO_y$ compounds.

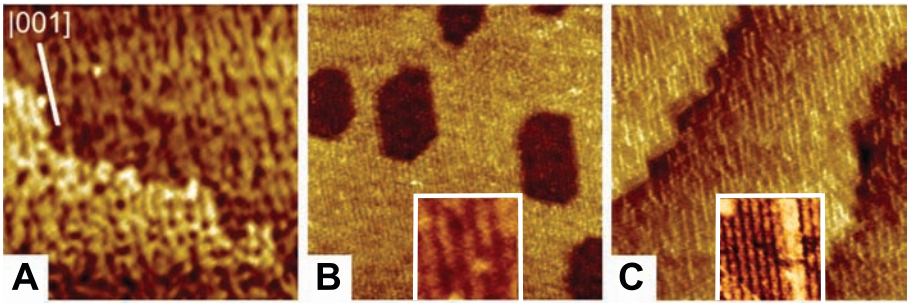

Figure 4.12: STM images (100×100 nm^2) recorded on TiO_2(1 1 0)–1×1 surface deposited by K of 0.36 ML at 330 K and annealed at (A) 700 K, (B) 900 K and (D) 1100 K for 2 min. The size of the STM images inserted in B and C (bottom middle) is 7×7 nm^2.

Note that only at this K coverage (θ_K =1/3 ML) was it possible to obtain an almost completely 1×2 reconstructed surface. Further annealing (2 min) at 1100 K resulted in a 1×2 → 1×1 phase transition (Fig. 4.12C). The lateral distance between the rows is 0.65 nm measured on the 7×7 nm^2 image inserted in Figure 4.12C. Note that the regained bulk terminated 1×1 surface shows higher concentration of reduced 1D stripes than that for the initial surface (before the deposition of K at near room temperature).

The effect of the variation of the initial K coverage can be seen on the images presented in Fig. 4.13. The disturbed atomic terraces formed after annealing at 900 K can be compared. In the case of a low K coverage (θ_K = 0.09 ML), the surface exhibits the formation of flat terraces decorated by small nanoparticles described above (Fig. 4.13A and 4.11). At approximately 1/3 ML coverage, the same treatment results in the formation of pits and a reconstruction into 1×2 arrangement (Fig. 4.13B). By further increasing the initial K coverage, the extension of the pits becomes sufficiently large for the appearance of protruding islands (Fig. 4.13C). The different terrace composition developed suggests that the formation of this kind of terrace decorations is certainly connected to the initial K concentration.

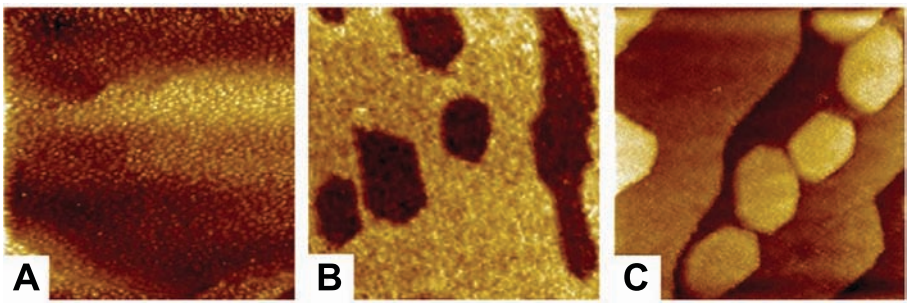

Figure 4.13: STM images (100×100 nm^2) taken after different K depositions at 330 K and annealing at 900 K for 2 min: (A) 0.09 ML, (B) 0.35 ML and (C) 0.66ML.

According to our best knowledge, this is the first systematic STM study on the thermal behavior of a K-deposited TiO_2 single crystal surface. The thermally induced morphological changes studied for lower K coverage (app. 0.1 ML) clearly indicate that in spite of the very slight change of the relative K Auger-signal and the lack of desorbing species detectable by TPD measurements, the STM indicates a huge material transport in the surface layers even below 900 K (Figs. 4.10 and 4.11). The splitting of terraces is especially an interesting feature suggesting that Ti ions become also mobile in the presence of surface K. Taking into account the low intensity of the AES signal and the relatively large coverage of islands found by STM (Fig. 4.11B), it can be assumed that the K atom is immerged in the interface (subsurface) layer [156]. For larger K coverages ($\geq$ 1/3 ML) we have found even more dramatic rearrangements in the surface layers (Fig. 4.12). In this work, it was assumed that the partial reduction of TiO_2 by adsorbed K or Cs and the formation of a mixed alkali-metal–Ti oxide may be thermodynamically preferred. From experimental aspects, a weak point of this argument could be that, in our case, no other desorbed species, but potassium and a very low intensity KO signal, were detected. In an earlier paper, the bulk to surface diffusion of Ti ions was studied and it was concluded that below 900 K the segregation of Ti to the surface is strongly retarded [157]. In this way, only the pits appeared on the $TiO_2(1\,1\,0)$ atomic terraces (Fig. 4.12B) suggest that a compound containing Ti was also desorbed.

4.2.4 Summary

In summary, the reaction of alkalies with oxide surfaces can be well modeled by the $K/TiO_2(1\,1\,0)$ system. From the strong electrical modification of the surface (detected by STM), it can be concluded that there is a non-localized charge transfer from the K to the substrate in good agreement with the previous results. The AES and TPD study of the desorption clearly shows that at larger coverages the sublimation energy decreases via the decrease in the heat of adsorption. The formation of the reduced 1×2 reconstruction and the presence of terrace decoration after annealing to 900 K strongly suggest that potassium creates both $K{-}O_x$ and $K{-}Ti_xO_y$ compounds and leaves the surface in this form. Annealing further near to 1100 K results a back transformation to the original 1×1 reconstruction with slightly increased concentration of strings. This latter process may be connected to the segregation of oxygen from the subsurface region.

4.3 Surface characterization of TiO_2 supported Rh crystallites

4.3.1 Tailored Formation of Rh Crystallites on $TiO_2(1\,1\,0)$

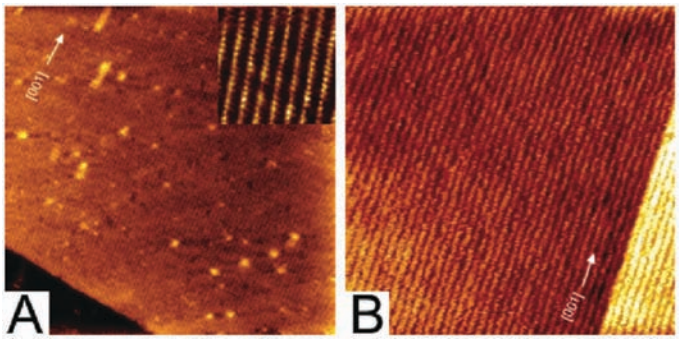

Figure 4.14: Characteristic constant current (*cc*)STM images of 50×50 nm^2 recorded on (A) $TiO_2(1\,1\,0)$–1×1 and (B) $TiO_2(1\,1\,0)$–1×2 surfaces used as supports for studying the growth of Rh. The insert in (A) shows a 5×5 nm^2, atomically resolved STM image recorded the 1×1 bulk terminated terrace.

Most of the experiments presented here were carried out on a bulk-terminated $TiO_2(1\,1\,0)$–1×1 surface exhibiting defect features of low concentration. Figure 4.14A shows an STM image of a constant current (*cc*) mode (50×50 nm^2) recorded in a region of typical morphology. The inserted constant height (*ch*) mode image (5×5 nm^2) exhibits bright rows corresponding to Ti_{5f} atoms and the rows are separated by 0.65 nm. We also used more reduced samples having a complete 1×2 reconstruction presented in Figure 4.14B. For detailed discussion of the clean support see Section 3.1.

Regarding the supported metal particles, to detect the inner structure of the top facets, one needs nanoparticles. Three distinct methods were applied in this work to form larger Rh particles: (1) deposition of Rh at RT and annealing at elevated temperatures, (2) deposition of Rh at elevated temperatures in the range of 850–1050 K, and (3) deposition of Rh at elevated temperature (1050 K) onto a $TiO_2(1\,1\,0)$–1×1 surface previously decorated with Rh nanoparticles. In the first case, the average size of the particles will be rather low as compared with those prepared by the other two methods. Nevertheless, by depositing a larger amount of Rh (8–10 ML), the first method leads to the formation of larger dendrite-like nanoparticles. By applying the second and third methods, the deposition performed at high temperatures results in the growth of large and well-separated Rh particles [158, 159].

Figure 4.15 displays some characteristic 20×20 nm^2 STM images recorded after different deposition conditions. The deposition of 0.03 ML of Rh at 330 K onto a $TiO_2(1\,1\,0)$–1×2 surface

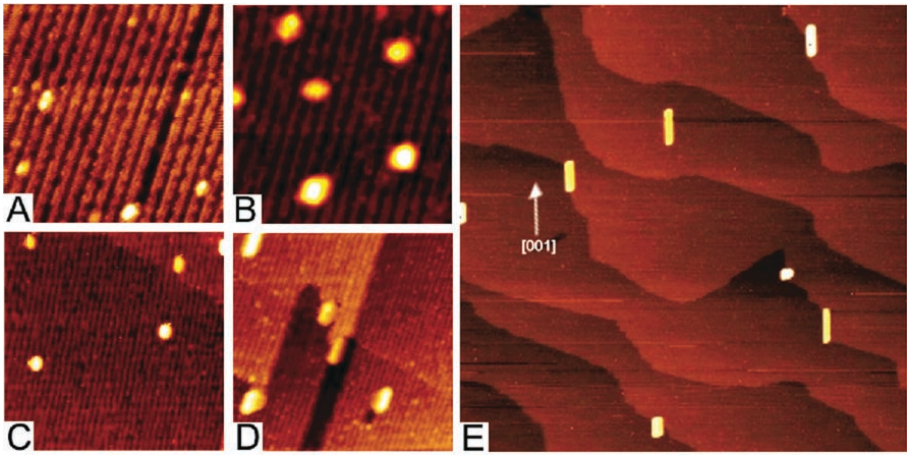

Figure 4.15: The morphology of Rh/ $TiO_2(1\,1\,0)$–1×2 prepared by different treatments: (A) deposition of 0.03 ML of Rh at 330 K, followed by 10 min annealing at 850 K; (B) after deposition of additional 0.25 ML Rh at 850 K onto the surface imaged in part A; (C) deposition of 0.05 ML of Rh at 330 K, followed by 10 min annealing at 950 K; (D) after deposition of an additional 0.30 ML Rh at 950 K onto the surface imaged in part C. Image sizes: (A, B) 20×20 nm^2, (C, D) 50×50 nm^2. Finally, image (E) represents an STM image of 400×400 nm^2 recorded on $TiO_2(1\,1\,0)$–1×1 after depositing 0.30 ML Rh at 1050 K.

and annealing at 850 K for 10 min results in 1–2 atomic layer thick Rh nanoparticles with a diameter of ∼1.5 nm (Figure 4.15A). The average particle density is $\sim 1.5 \times 10^{12}$ cm^{-2}. It can be seen that the particles preferentially occupy the bright rows identified with a reduced 1D phase, and some of them are slightly elongated along the rows. Despite the appearance of somewhat elongated Rh particles in the first step, the Rh particles postgrown at 850 K (deposition of an additional 0.25 ML Rh onto the surface characterized Figure 4.15A) are mostly of round shape (Figure 4.15B). The average diameter and thickness of the nanoparticles varied in the range of ∼1.5-2.2 nm and 1–3 atomic layers, respectively. The particle density (the number of particles on a unit surface area) did not change, suggesting that the mean free path of the atomic diffusion is larger than the average particle–particle distance (∼4-6 nm) in the present case.

The same sequence of experiments was also performed at 950 K (instead of 850 K, before) (Figure 4.15C, D). The size of these latter STM images is 50×50 nm^2. It can be observed that nearly round Rh nanoparticles are formed after the deposition of Rh (0.05 ML) at 330 K and annealing of the probe at 950 K for 10 min (Figure 4.15C). The average diameter of these nanoparticles is 3 nm, and they consist of 2–3 atomic layers. The postdeposition of Rh at 950 K results in mainly elongated particles, independently of their location (Figure 4.15D). Note that some pits around the particles appear frequently, as can be seen at the end of the nanoparticle located on the right terrace of the recorded region. The appearance of similar features indicates

clearly that the titania surface itself becomes mobile above 900–950 K [160]. At the same time, the change in the growth mode, in which the formation of elongated particles will be prevailing, is probably connected with the activation of the support lattice diffusion, as well. On the basis of a more detailed investigation of the 1D growth of Rh particles, we can state that the ratio of the elongated and the round particles increases gradually by raising the temperature in the range of 850–1050 K. Moreover, this behavior is more or less independent of the reconstruction of the support; it appears also on a bulk- terminated $TiO_2(1\,1\,0)$–1×1 surface. Strongly elongated Rh nanoparticles were formed at high probability after the deposition of Rh at 1050 K (without seeding before) onto an unreconstructed titania surface, as is shown in a large-scale STM image of 400×400 nm^2 (Figure 4.15E).

The main message of the experimental results presented in this section is that by varying the deposition conditions, it is possible to grow isotropically or anisotropically extended Rh nanoparticles, which provides facility for detailed and systematic study of the formation of SMSI decoration films. The detection and analysis of the ordered or quasi-ordered decoration layers formed in the growth procedures described above are reported in the subsequent part of this work. The terminology used in a recent study on a TiO_x film/Pt(1 1 1) system presented by Granozzi *et al.* was applied for similar structures observed in this work [92, 93].

"Worm-Like" Decoration Layer

Formation of a quasi-ordered decoration layer was observed for giant hexagonal particles, indicated by I in Figure 4.16A. These particles were grown by postgrowth of Rh on $TiO_2(1\,1\,0)$ surface: deposition of 0.8 ML Rh at 1050 K followed by repeated deposition of 10 ML of Rh at 1050 K. The size of the image is 200×200 nm^2. Note that due to the tip–particle convolution, it was difficult to obtain a sharp perimeter line around the particles. The height of this nanoparticle is ∼2.5 nm (10–12 atomic layers). The constant-height STM images of two different scales of 20×20 nm^2 and 10×10 nm^2 in Figure 4.16B and C recorded on its top facet clearly show the appearance of 1D stripes with a length of 2–3 nm and a width of ∼0.5 nm. These features are randomly oriented in a hexagonal overall structure, which is probably determined by the symmetry of Rh(1 1 1) facet. They are more or less uniformly distributed on the Rh facet (Figure 4.16B), and a few of them follow the edge of the particle aligned in the [0 0 1] orientation of the support oxide. This structure is reminiscent of a "worm-like" texture also described by Sedona *et al.* [92]; however, in our case, it clearly consists of straight 1D nanostripes. A very similar overlayer structure but

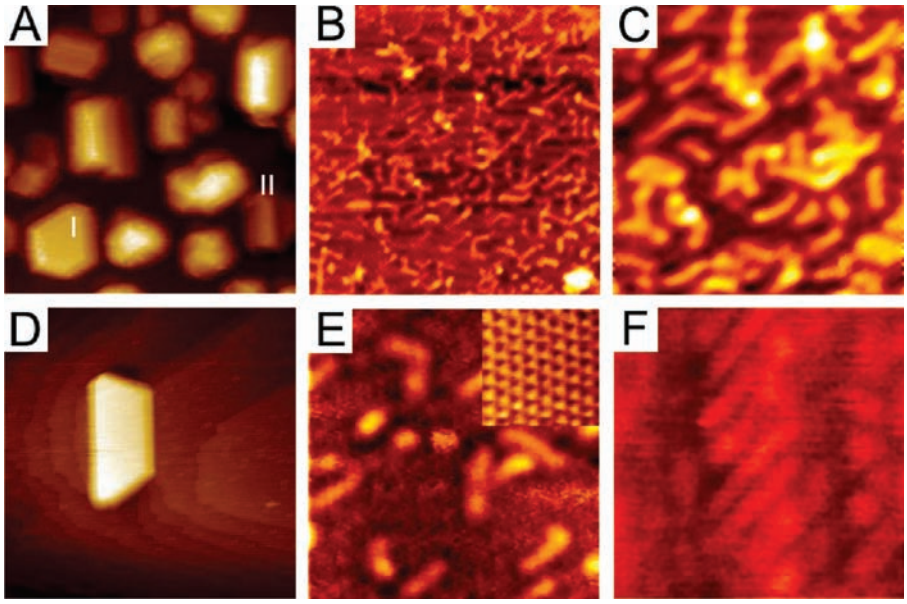

Figure 4.16: Worm-like decoration layer detected on different Rh nanoparticles supported on a $TiO_2(1\,1\,0)$–1×2 surface. (A) Large Rh particles grown by a postgrowth method at 1050 K (image size: 200×200 nm). (B, C) STM *ch* images recorded on the top facet of a hexagonal Rh particle, indicated by **I** on the *cc* image (A). Image sizes: (B) 20×20 nm and (C) 100×100 nm. (D) Large elongated hexagonal Rh nanoparticle detected on a 100×100 nm area and (E) its top facet structure (the inset shows a 2×2 nm area of clean Rh with atomic resolution). (F) Periodic overlayer structure observed on the top facet of an elongated nanoparticle indicated by **II** in the image (A). The size of the latter image is 5×5 nm. The STM images (D, E, F) were recorded in *cc* mode.

with a lower concentration of the stripes was detected on the top facet of the postgrown elongated and hexagonal Rh nanoparticle shown in Figure 4.16D. In this case, in addition to the stripes, some 0D nanodots can also be seen in the image of 10×10 nm^2 (Figure 4.16E). Moreover, an atomically resolved image of the undecorated facet regions clearly exhibits a configuration characteristic of the Rh(1 1 1) surface with a periodicity of 0.27 ($\pm$0.01) nm (the bulk nearest distance is 0.269 nm), as can be seen in the inset of 2×2 nm^2 (Figure 4.16E). The decoration layer detected on a 14 atomic layer high elongated Rh nanoparticle (indicated by II on the Figure 4.16a) exhibits periodically arranged stripes with a separation of 0.53 nm, being very close to the 1×1 periodicity (Figure 4.16F). The size of the latter STM image is 5×5 nm^2.

All the STM images presented in this section were recorded in constant current mode by chemically etched W-tip. The subsequent high-resolution images, however, were recorded mostly in constant height mode to obtain the best lateral contrast.

"Wheel-Like" Decoration Layer

Our first experimental indication of a 2-dimensional long-range ordered encapsulation layer was obtained on large hexagonal Rh crystallites grown by deposition of Rh (∼1.2 ML) at 1050 K onto a Rh-seeded (deposition of 0.04 ML Rh at 300 K, followed by annealing at 1050 K for 15 K) $TiO_2(1\,1\,0)$–(1×2) sample. Figure 4.17A shows a 50×50 nm^2 region where both a hexagonal and an elongated Rh particle can be seen. The top facet of both particles exhibits some extra features, suggesting the formation of decoration phase. In the case of the hexagonal crystallite, the dots are arranged in a quasi-hexagonal ordering, as it is presented in a magnified image of 6×6 nm^2 (Figure 4.17B). These images were recorded in constant current mode. As indicated in Figure 4.17A, there is a rotation angle of $17(\pm 2)^\circ$ between one edge of the hexagonal crystallite and one row of their overlayer structure.

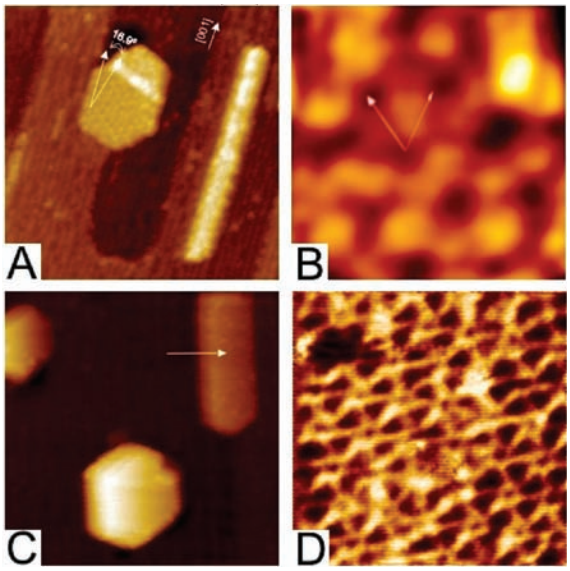

Figure 4.17: (A) Hexagonal and elongated Rh nanoparticles grown on TiOtwo surface exhibiting 1D reduced Ti_2O_3 phase in high concentration. (B) The top facet of the hexagonal particle indicating the presence of quasi-ordered hexagonal decoration layer. (C) STM image showing large Rh particles and (D) its long-range ordered decoration phase (wheel structure). Image sizes: (A, C) 50×50 nm^2, (B, D) 6×6 nm^2. Images A, B, and C were recorded in *cc* mode; image D was detected in *ch* mode.

In another case, in which the Rh particles were grown on a $TiO_2(1\,1\,0)$–1×1 surface (without preseeding) by deposition of 0.8 ML Rh at 1050 K (Figure 4.17C), a less intense hexagonal wheel structure was recorded in constant height mode, as shown in Figure 4.17D. This texture was detected on the top facet of an elongated particle (a 5–6 atomic layers height nanoplank) indicated by the arrow in Figure 4.17C. The periodicity of the hexagonally arranged wheel structure was $1.50(\pm 0.05)$ nm, determined by the average distance of the pivots (black holes in the center of the

wheels).

It is worth noting that the top facets of the hexagonal particles are not always parallel to the plane of the support oxide, but they can show a typical declination of $8 - 10^{\circ}$, as in the case of the center bottom particle in Figure 4.17C. This declination angle can be explained by the formation of a reconstructed $TiO_2(1\,1\,0)//Rh(1\,1\,1)$ interface at the early stage of the Rh nucleation. Nevertheless, for the detection of ordered decoration layers, we chose the particles with the top facet parallel to the substrate, indicating the $TiO_2(1\,1\,0)//Rh(1\,1\,1)$ interface.

To improve the resolution of the imaging of encapsulation layers, we used constant height mode. In the course of recording the image, both the current and the bias were carefully adjusted. In Figure 4.18, two STM *ch* images recorded with different imaging parameters and contrasts are presented on a more or less completely ordered encapsulation layer. The hexagonal unit cell (1.46 ± 0.05 nm) of this periodic structure can be clearly recognized, as indicated in Figure 4.18A. Note that the unit cell of this structure is slightly smaller than that of the similar pattern in Figure 4.17. One side of the bright triangles of the wheel structure exhibits a rotation angle of 11°, compared with one of the unit cell vectors. The inner atomic structure is also appreciable, and it clearly consists of six atoms (5 times the 0.31 nm atom-to-atom distance) in the direction of the wings. The atomic rows are more visible in Figure 4.18B, although the contrast for the wheel structure itself is reduced in this case.

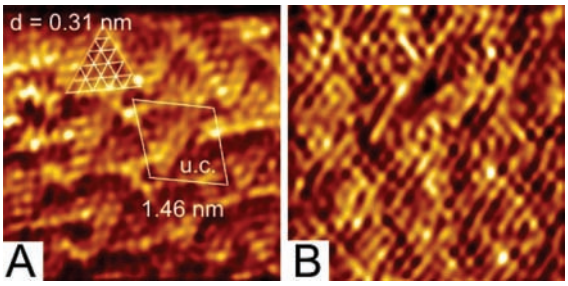

Figure 4.18: (A, B) Atomically resolved constant height STM images detected on a completely decorated large, hexagonal Rh particle formed at 1050 K. They show the wheel structure in two different contrasts. The characteristic lattice parameters are indicated on the image (A). Image sizes: 5×5 nm^2.

4.3.2 Removing and Restitution of Decoration Layers by Ar^+ Sputtering

In the subsequent experiments, we chose a preparation method that results in Rh crystallites with rather large top facets. The surface morphology detected by STM after depositing 13 ML of Rh at room temperature and annealing the $TiO_2(1\,1\,0)$–(1×2) sample at 1050 K for 5 min is

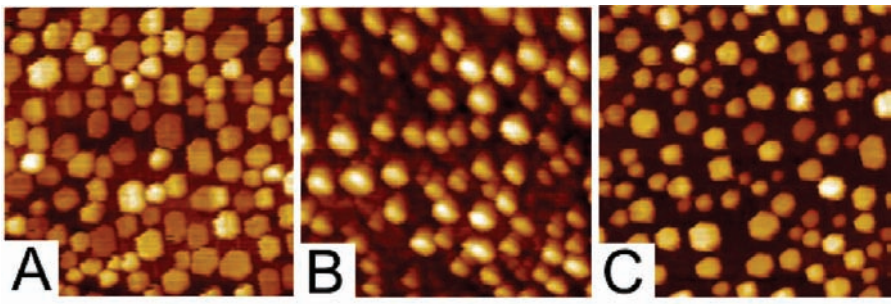

Figure 4.19: STM and AES detection of the removal of Rh nanoparticles formed at 1050 K. STM images of 100×100 nm^2 detected (A) before and (B) after 110 s Ar^+ bombardment at room temperature and (C) following 10 min annealing at 1050 K in UHV.

shown in Figure 4.19A. The size of the selected characteristic region was 100×100 nm^2, and the surface density of the particles was $\sim 0.97\,(\pm 0.05)\,10^{12}$ cm^{-2}. The largest hexagonal particles consist of 25–30 atomic layers. Starting from this state, the effect of stepwise Ar^+ bombardment ($\sim$12 μA/cm^2, 0.5 keV) on the relative Auger electron spectrometry (AES) intensity of Rh (R_{Rh}) is shown in Figure 4.20. R_{Rh} is defined as the ratio between the peak-to-peak intensity on $^{\mathrm{d}N}/_{\mathrm{d}E}$ Auger-spectra for Rh and Ti elements at energies of 302 and 385 eV, respectively. This value increases in the first period of the bombardment (0–30 s) from $\sim$1.2 up to $\sim$1.6, followed by a gradual decrease down to $\sim$0.6 at 110 s duration of the sputtering. The initial increase in the Rh signal has already been observed by similar AES and low-energy ion scattering spectroscopy measurements, and it was explained by the removal of a TiO_x decoration ultrathin film from the top of the supported and encapsulated metal nanoparticles [83].

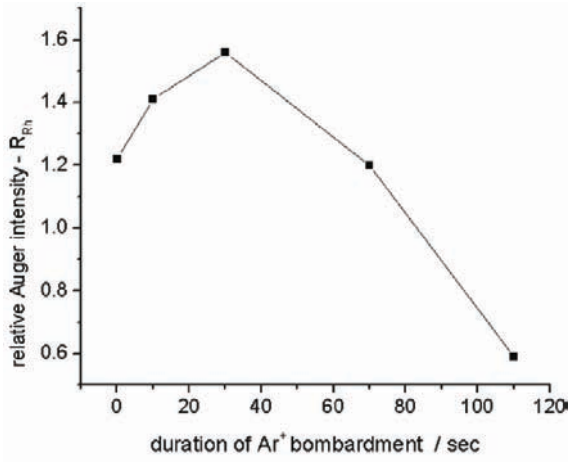

Figure 4.20: Change in the relative intensity of Rh (302 eV) and Ti (385 eV) AES signals after 0.5 keVAr^+ sputtering.

After accomplishing the sputtering cycles, the surface morphology was tested by STM (Fig-

ure 4.19B). The characteristic surface area of 100×100 nm^2 exhibits similar surface density of the nanoparticles, with significantly modified shape (unfortunately, this special image is also influenced by a tip-shape convolution effect). The sharp, hexagonal outline of the particles disappeared, and the average corrugation of the surface decreased by ∼40 %. An estimation for the removed amount of Rh was possible by recording STM images after 5 min annealing at 1050 K (Figure 4.19C). The hexagonal morphology of the separated Rh particles is recovered. The Rh coverage was ∼6 ML, and the surface density of the particles was ∼0.95 (±0.05) 10^{12} cm^{-2}. The highest particles consist of 20–25 atomic layers (only slightly less than originally), indicating that the Ar^+ sputtering and annealing reduce mainly the mean diameter of the nanoparticles. From the decrease in coverage for the states of A and C (Figure 4.19), it can be estimated that in our case, 15–20 s sputtering is sufficient for removing 1 ML of Rh. We assume that this statement is also valid for the encapsulation layer.

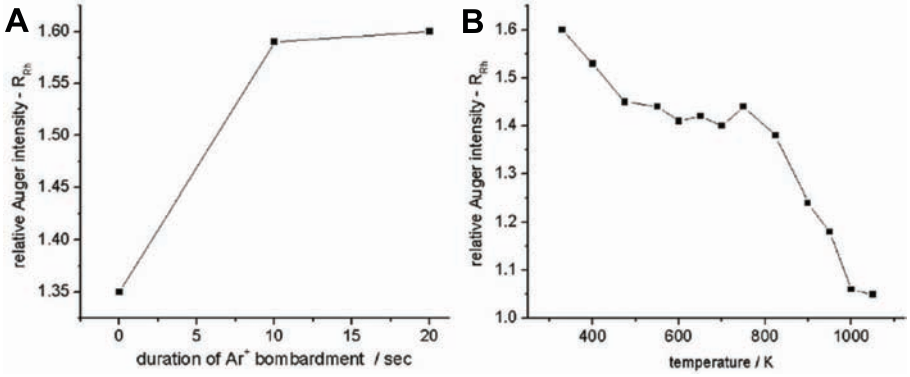

Figure 4.21: AES detection of removal and restoration of ordered TiO_x decoration SMSI layer covering Rh nanoparticles. Change in the relative intensity of Rh and Ti AES signals as a function of (A) Ar^+ sputtering duration and (B) the subsequent annealing at elevated temperatures.

In the following experiments, we investigate the restitution of the ordered encapsulation layer removed previously by Ar^+ sputtering. After cleaning the $TiO_2(1\,1\,0)$ surface and preparing Rh particles similarly as above, the sample was sputtered for only 20 s, at which point the relative AES signal for Rh reached roughly a maximum (Figure 4.21A). Subsequently, the probe was stepwise annealed up to elevated temperatures, and after each annealing cycle, an AES spectra was recorded (Figure 4.21B). There is a slight (∼10%) decrease in R_{Rh} resulting from the effect of annealing between 300 and 450 K, followed by a range (450–800 K) of almost constant level. The initial decrease at low temperatures may be explained by reordering of the Rh nanocrystallites; however, regarding the increased mobility of the support material due to the previous ion sputtering, a limited decoration process cannot also be excluded in this low temperature range. The reordering

of the surface Rh means that atomically dispersed Rh produced by the ion bombardment can condense on the larger Rh nanoparticles.

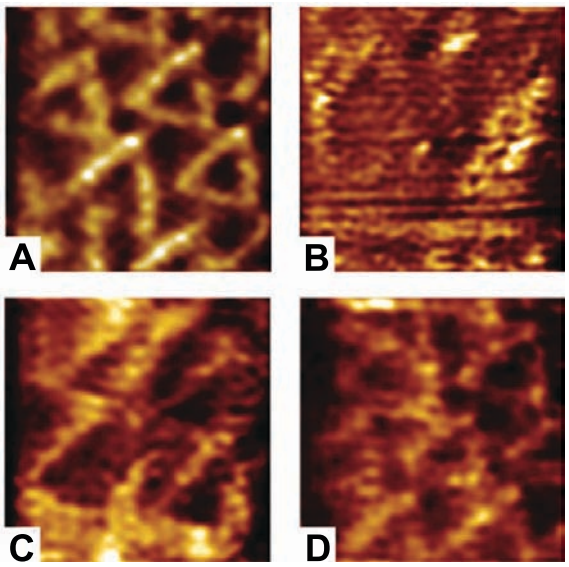

Figure 4.22: Characteristic constant height STM images (4×4 nm^2) of the structure of top facets of Rh nanoparticles (A) before and after 20 s Ar^+ sputtering followed by annealing at (B) 650, (C) 900, and (D) 1000 K.

For the thermal treatments in the range between 800 and 1000 K, the decrease in Rh relative the AES ratio is very pronounced, and it reaches a value that is slightly lower than that before the Ar^+ bombardment (Figure 4.21). The difference between the final value of R_{Rh} (1.0) in Figure 4.21B and its initial value (1.34) in Figure 4.21A is larger than the error limit of the measurement; accordingly, it indicates the removal of some amount of Rh itself, or it suggests a modified stoichiometry or some contamination of the bar support regions. Nevertheless, the main drop in the R_{Rh} signal between 800 and 1000 K K is probably a consequence of the recovery and the shadowing effect of the decoration TiO_x thin film. It means that for our samples, the formation of a decoration film takes place in the temperature range of 800–1000 K, as can be seen in the STM images (Figure 4.22). The constant height images of 4×4 nm^2 clearly show that the wheel structure is present before the sputtering (Figure 4.22A), but obviously disappears after the bombardment and annealing at 650 K in UHV for 5 min (Figure 4.21B). Some ordering can be observed after the thermal treatment at 900 K for 5 min (Figure 4.22C), but the reappearance of triangles characteristic of the wheel structure takes place only after annealing at 1000 K (Figure 4.22D).

4.3.3 The Role of Surface and Subsurface Diffusion in the Formation Decoration Adlayers

The formation of epitaxial, ultrathin oxide layers on the top of metal nanoparticles supported on oxide surfaces is a result of a rather complex diffusion process in which the kinetic parameters of both the surface and subsurface diffusion are of importance [5]. Regarding the limited mass transport in the formation of an atomic scale adlayer and the diffusion distances of only few nanometers, we can assume that after the thermal treatment of several minutes at 900–1100 K, the energetically stable state can be reached for the decoration systems investigated here. Concerning the source of the mass transport, the components of the support oxide structure should be mobile at the temperatures of the decoration process. It is known that the mobility of the metal and oxygen atoms is higher in the reduced oxide phases; accordingly, the formation of a decoration film takes place at lower temperatures on reduced $TiO_2(1\,1\,0)$ surfaces than on stoichiometric ones [5, 81, 161].

This feature also connects strongly to the original observation of SMSI, where the formation of this state was detected as a result of annealing in hydrogen atmosphere. It was assumed that the primary role of this gas is probably reducing the surface and subsurface region of the support [80, 81]. Note that the preliminary step for the SMSI process is the spillover of hot atomic hydrogen formed by the dissociation of H_2 molecules on the metal particle. The defect sites formed in this way in the surface and subsurface region of the oxide will serve as a diffusion path for the Ti and O atoms, although the role of the interstitial diffusion cannot be neglected [157, 162, 163]. Moreover, the surface diffusion of certain atomic clusters of Ti_xO_y may also play some role, as was shown for the slightly sputtered $TiO_2(1\,1\,0)$ surfaces [164].

Fu and Wagner have called attention to the dual driving force of the decoration process: (i) interfacial charge redistribution (electronic interaction) and (ii) interfacial mass transport (chemical interaction) [5]. Note that this duality is also expressed in the double designation ("strong metal–support interaction, SMSI" and "decoration"), which incidentally induced vigorous debates on the mechanism of the process. Actually, the "decoration" is mainly indicative of the mass transport, while the original meaning of SMSI is expressively related on the electronically influenced CO uptake [80, 165]. In their review, Fu and Wagner completed the mechanism of SMSI by proposing a strong interplay between the chemical and electronic effects. They emphasize the connection between the interfacial space charge and the diffusion of ionic defects across the interface [5]. In

other words, the mass diffusion processes from the subsurface region to the surface are significantly activated by the charge distribution (Schottky barrier) determined by the work function of the constituent materials.

The diffusion of constituent metal ions of the oxide to the supported metal particles is not retarded effectively at the oxide particle perimeter line because they bind more stably on the metal particles than on the support itself. This feature reveals itself in the fact that we have never detected extra material accumulated at the perimeter of the crystallites. At the same time, on filling up the decoration overlayer, this driving force will be drastically attenuated. This effect probably leads to the well-known self-limitation of the decoration layer, keeping it in atomically thin layer form. The decoration oxide film toward the metal nanoparticle is usually terminated by the metal atom of the oxide due to the stronger bonding between M support and M particle than between O support and M particle. Accordingly, the characteristic decoration layers consist of M–O double layers terminated by O toward the vacuum, as in the case of the zigzag or wagon-wheel structures [85–87]. This is probably also the case for the decoration layer formed on Rh nanoparticles supported on a $TiO_2(1\,1\,0)$ surface. Naturally, the stoichiometry of the decoration layer formed by a certain annealing treatment is determined by the oxidation state of the support and the particle/decoration interface energy. This condition results in a sensitive variation of the decoration layer composition, as was studied in detail for Pt/TiO_2 sytems [90–94].

For a two-dimensional ordering of the accumulated oxide phase on the top facet of the supported metal nanocrystallite, several requirements have to be fulfilled: (i) a sufficiently large (5–10 nm^2) flat facet of the metal crystallite and (ii) a rather strong bond between the oxide ultrathin film and the metal or sufficiently large cohesion inside the layer of the 2D form, preventing its transformation into 3D oxide particles. The studies on the reactivity of encapsulated particles indicate that a complete capping layer (sheet) is rather unreactive toward adsorption of any gases. This is true even for not fully oxidized oxide layers [92]; however, these complete ultrathin oxide films may play a very important role in different catalytic reactions [89].

4.3.4 Comparison of "Wheel-Like" Decoration Layers

The high-temperature, ultrathin oxide films exhibiting wheel-like (w) structure represent a characteristic and interesting long-range, ordered decoration phase that was observed for different oxide–metal compositions [85, 92, 110, 166–168]. Note that the wheel-like arrangement is only a single case among the other ordered and quasi-ordered structures found and studied in detail; for

example, the case of oxidative deposition of Ti onto Pt (1 1 1) surface [90–94].

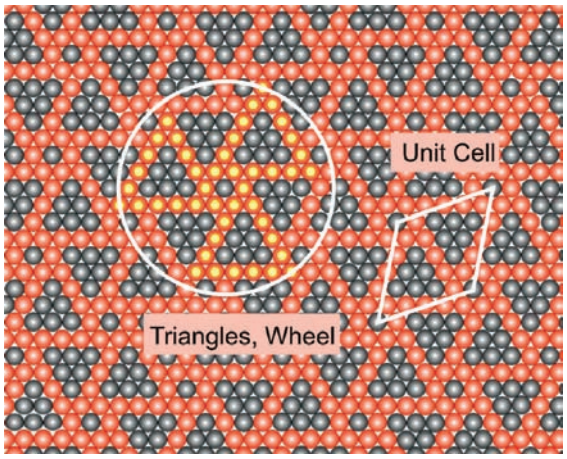

Figure 4.23: Scheme of the wheel structure.

Despite the overall similarity of w-structures, the details of their contrast and the interpretation of the pattern are yet unclear. The most important question is whether this film consists of only Ti and O or some mixing with the atoms of the supported noble metal, such as Rh and Pt, also takes place. The characteristic features of this arrangement depicted in Figure 4.23 are the following: (1) bright dots forming triangles, (2) three triangles constitute a wheel, (3) axle points of the wheels determine the unit cell, (4) the number of dots in the wheel spokes (part of the triangles), and (5) the characteristic distance between the neighboring dots.

It is rather surprising that the clearest STM image for a w-structure was presented in the case of a Pt(111) surface exposed to Cr atoms at room temperature and annealed at 800 K without using oxygen [166]. The strong contrast of the wheel spokes was explained by the formation of a long-range ordered surface alloy in which the characteristic bright triangles consisted of Pt atoms. For this system, varying the bias direction caused a spectacular change in the STM contrast. Accepting this suggestion, Bowker and his co-workers interpreted the w-like decoration film formed on the top facets of Pd crystallites supported on TiO_2 as a surface alloy (Pd–Ti) oxide [85]. In contrast to this explanation, the w-structure is identified as a two-dimensional M–O double layer in which the overlayer structure is terminated with oxygen atoms in the case of reactive deposition of Ti onto Pt(1 1 1) surface [92] and that of V onto the Rh(1 1 1) surface [168, 169]. The large unit cell of this structure is probably the result of a slight misfit between the atomic lattice of the metal particles and that of the overlayer oxide (moiré pattern).

The unit cell vector of these structures varies in the range of 1.5–1.9 nm and the number of spoke atoms changes in the range of 4–6. The assumption that the wheel structure is a moiré

pattern implies also the statement that the supported oxide layer can be regarded as a sheet. Note that from this point of view, this thin film behaves similarly to the covalently bonded graphene. This condition is obviously much more fulfilled for the TiO_2-film/Ru(0 0 0 1) system, in which a clear moiré pattern appears [170]. Nevertheless, in the case of a reduced TiO_x film the bonding to the supporting metal is probably more stable.

These conditions suggest double roots of appearance of the wheel pattern: (1) moiré-like behavior where the periodicity is determined by the lattice misfit and (2) significant lateral relaxation of the atoms in the oxide film caused by local interaction with the supporting metal atoms. In the case of Rh(1 1 1), the complex wheel structure is, in fact, a moiré pattern formed by a superposition of the hexagonal lattices of the oxide film with lattice constant of 0.31 nm and that of the underlying metal.

In the experiments presented in Figure 4.21 and 4.22, we tried to follow the building up of a wheel-like decoration layer. We assumed that the worm-like structure (Figure 4.16) consisting of 1D stripes (oriented in the close-packed direction of the Rh crystallites) is an initial state for the 2D wheel structure. Unfortunately, we did not find direct evidence, only a faint indication, for this idea. It is worth mentioning that the 1D type growth of ionically bonded layers on metal surfaces was found in several cases; for example, for submonolayer growth of NaCl on Cu(1 0 0) [169]. The uniform length of the TiO_x nanostripes observed in our case is probably caused by the accumulated strain appearing at their ends.

4.3.5 Summary

Formation of ordered decoration TiO_x layer was found on TiO_2(1 1 0)-supported Rh nanoparticles as a result of annealing at 1050 K. This finding reveals that the formation of ordered 2D TiO_x films is a quite general feature for the noble metal/TiO_2 systems. The encapsulation layer at saturation coverage exhibited a "wheel" structure with a hexagonal unit cell of ∼1.5 nm × 1.5 nm. The wheels are determined by three triangles consisting of 5 atoms in a distance of 0.31 nm. A "worm-like", partially saturated layer was also detected which exhibited 1D stripes (nanostripes) oriented in the close-packed direction of the Rh(1 1 1) top facet. The characteristic sizes of these latter features are the following: width of 0.5 nm and length of 2–3 nm. The "worm-like" structure can be regarded as an initial state for the formation of the "wheel" arrangement. It was proved that it is possible to selectively remove the "wheel-like" decoration layer by Ar^+ sputtering (0.5 keV) and to subsequently restore it by a short thermal treatment at 1000 K.

4.4 Simultaneous STM/AFM measurement on Si(1 1 1)–7×7

Among characterizations of surface properties, proper working mechanism of the instrumentations needs to be ensured. As it was derived in chapter 4.1.2, parallel measurement of the tunneling current and force might lead to an undesired side effect, to the cross-talk phenomena between these two channels. In this chapter, the proper working mechanism of a tuning fork based AFM/STM microscope will be shown by using the exemplarily Si(1 1 1)–7×7 surface. Therefore, this chapter can be treated as supplementary to the adsorption parts.

4.4.1 Mapping of the Si(1 1 1)–7×7 surface

Simultaneous STM/AFM measurements were performed on the Si(1 1 1)–7×7 surface using our modified sensor. The measurements were done in the constant frequency shift mode at room temperature. To compensate long-range electrostatic forces, the bias voltage was adjusted at minimum of the Kelvin parabola (generally ≈ +0.4 V). Figure 4.24 shows set of the average tunneling current $<I_t>$ and the constant frequency shift maps at the decreasing tip–sample separation. While we were unable to observe any atomic contrast in the topography signal at Δf set points above ≈ -35 Hz (see Fig. 4.24A, B), the atomic contrast in $<I_t>$ was already achieved. Approaching the tip further towards the sample, the onset of the short–range chemical force F_{SR} is reached and the atomic contrast in Z maps appears. When the set point Δf is tuned to more negative values, the atomic corrugation induced by the chemical interaction [171] between the tip apex and the adatoms becomes larger.

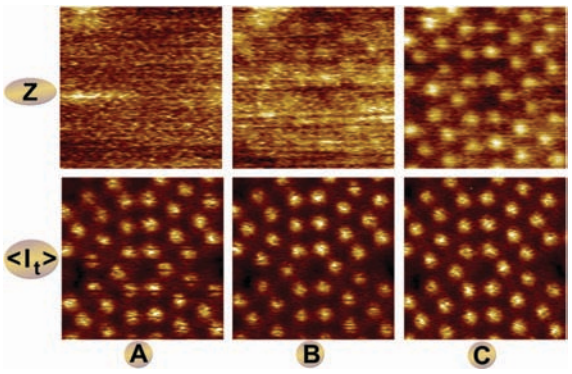

Figure 4.24: A set of the constant frequency shift maps (Z) and simultaneously recorded average tunneling current maps ($< I_t >$). The frequency shift set points for topographic imaging are the following: -35 (a), -40 (b) and -45 Hz (c).

4.4.2 Site-specific point spectroscopy above Si adatoms

In addition, we performed site-specific point spectroscopy [172, 173] above Si adatoms. Note that the spectroscopy curves shown in Fig. 4.25A were obtained with a slightly different tip than the maps in Fig. 4.24. To obtain the bare short-range force above an adatom, we subtracted the long range component of the force measured above the corner hole site. The dependence of the short-range chemical force and the tunneling current on the tip-sample distance is plotted in Figure 4.25A.

For this particular tip, the short range force maxima reached 1.5 nN. Both the tunneling current and the short range force show the exponential dependence $A(z)=A_0e^{-2\kappa z}$ where A means I_t or F_{SR} on the tip-sample distance z at large distances (for *z>0.24 nm* for I_t). We also estimated the characteristic decay lengths of the tunneling current κ_I=11.9 nm^{-1} and the short-range force κ_F= 6.3nm^{-1}. Comparing the characteristic decay lengths $\kappa_I \approx 1.89^*\kappa_F$, we immediately find the tunneling current is proportional to the square of the short-range force *(*$I_t = F_{SR}^2$). Note that this relation corresponds to the interaction between two localized states degenerated in energy as it was recently predicted theoretically (see a related discussion in [174]).

In distance z smaller than 0.24 nm, the tunneling current is no longer exponential function of the distance z. It drops significantly due to the substantial modification of the atomic and electronic structure of the surface dangling bond state [175]. The drop occurs close to the set-point, where the short-range force reaches the maxima. Our spectroscopic data agree very well with similar measurements done by the beam deflection method [176].

Additionally, we repeated the spectroscopy measurement with the identical sensor but with different tip apex. The tip change was induced by applying combination of z pulses and voltage pulses. The obtained data show (see Fig. 4.25B) a significant reduction of the force maxima of the short range force $F_{SR} \approx 0.8$ nN. In the weak interaction regime (here *z>0.07 nm*), the exponential dependence is presented. However the characteristic decay length of the tunneling current κ_I=7.6 nm^{-1} decreases while the decay length of the short-range force increased to κ_F=6.9 nm^{-1}. The ration between the characteristic decay lengths is $\kappa_I \approx 1.10^*\kappa_F$ now. Therefore, in this particular case the tunneling current I_t is closely proportional to the chemical force F_{SR} as it has been observed experimentally [177] and predicted theoretically [174, 177].

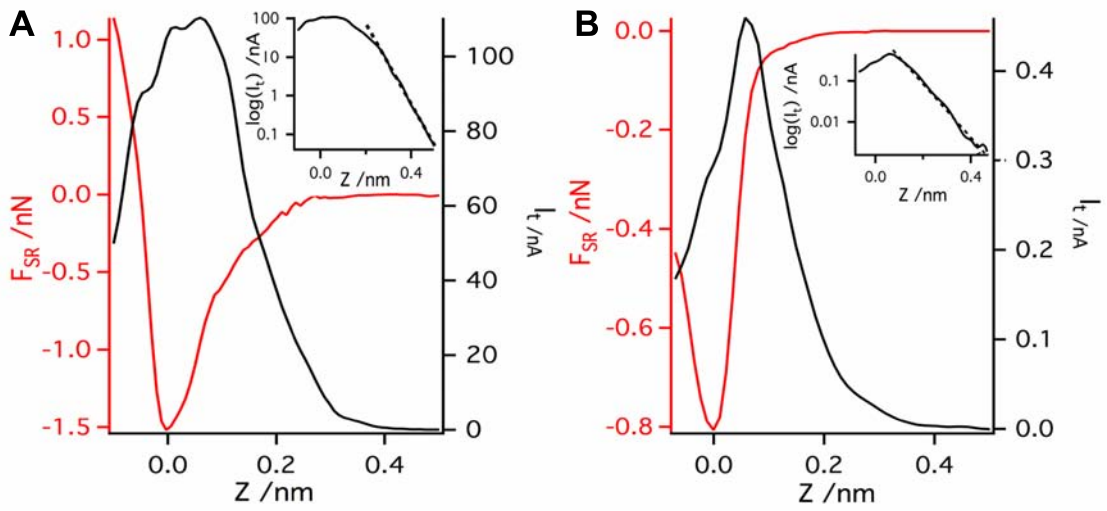

Figure 4.25: Two typically observed dependence of the short range interaction force (F_{SR}) and the tunneling current (I_t) on the tip-sample separation (z) with a logarithmic plot of I_t in the inset. The first tip termination (A) presents much stronger attractive short range interaction than the second (B), also the tunneling current is much smaller in (B) case. The acquisition parameters are $f_0 = 73180$ Hz, $a = 0.215$ nm, $k = 3750$ N/m, and $V_{bias} = 0.4$V.

4.4.3 Dissipation signal

Appearance of the dissipation signal and its origin in FM-AFM experiment has received a lot of both experimental [178–180] and theoretical [181–184] attention last years. However, general understanding of the dissipation mechanism is still missing. Beside of the electronic structure effects [185,186] and adhesion hysteresis at atomic scale [181,183], there is also a so called "apparent dissipation". Recently Labuda *et al.* [187] showed that the apparent damping can be attributed to the transfer function of the piezo-acustic excitations system. Therefore the dissipation signal needs to be carefully analyzed because it is one of the best indicators of the instrumental artifacts. As it was already discussed in the previous chapter, the cross-talk is accompanied by the presence of a distinct dissipation signal. What more, simultaneous measurement of the tunneling current and the frequency shift introduces additional complexity to the origin of the dissipation signal. Recently, Weymouth *et al.* reported so called "phantom force" phenomena [188], where an extra force arises due to a limited electron transport of injected charge in low conductive samples. However, there is not too much known about its impact on the dissipation signal yet.

In this section we analyze the effect of the tunneling current on the dissipation signal. This can be done by directly comparing the dissipation and tunneling current above the corner hole and adatom. As clearly shown in Figure 4.26 the dissipation signals are very similar, despite the strong difference in the magnitude of the tunneling current. Hence it can be concluded that tunneling

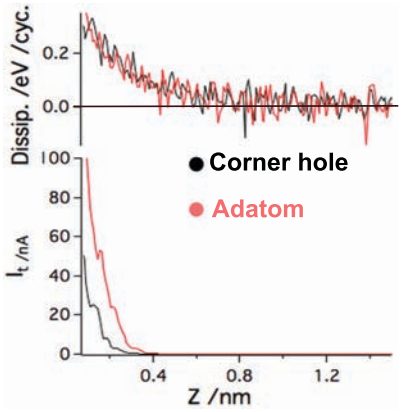

Figure 4.26: Analyses of the impact of the tunneling current on disspipation. It can be clearly seen that the tunneling current does not affect directly (by cross-talk) or indirectly by induced non-conservative forces the dissipation.

current does not affect directly (due to any kind of the cross-talk) the amplitude regulation in our modified experimental setup. One could also note, that at room temperature the tunneling current does not give rise to any non-conservative forces in the case of the Si(1 1 1)–7×7 substrate.

In order to analyze the long range dissipation in Figure 4.26, the relationship between the frequency shift and dissipation was investigated for both tip terminations presented in the previous subsection (reactive *Tip "A"* and less reactive *Tip "B"*). Comparing the frequency shift during the z approach for both tips, we can see that the the long range forces are more dominant for *Tip "A"*.

Interestingly we found that the long range dissipation signal is correlated to the frequency shifts. In order to see better the relation between the frequency shift and the dissipation signal, we plot the dissipation as a function of Δf for data measured above the adatoms(see insets in Figure 4.27). In both cases, the long range parts show linear relationship. What more, the slopes are nearly identical in both cases $(4.0\pm0.3)\times10^{-3}$ eV/Hz for *Tip "A"* and $(3.7\pm0.6)\times10^{-3}$ eV/Hz for *Tip "B"*). The proportional relation is broken at -76 Hz in the case of *Tip "A"* and -20 Hz in the case of *Tip "B"*. The linear dependence between dissipation and Δf suggests that the origin of the dissipation here is more instrumental (apparent) than related to the tip-sample interaction.

The apparent dissipation presented in our data can be explained by means of the effect of the piezo transducer transfer function reported recently [187]. This idea is supported by the fact that the relation between the frequency shift and the apparent dissipation in Figure 4.27 shows the same quantitative characteristics for both data sets. However, other tuning forks (operating at different eigenfrequencies) show different apparent dissipation or even no apparent dissipation at all.

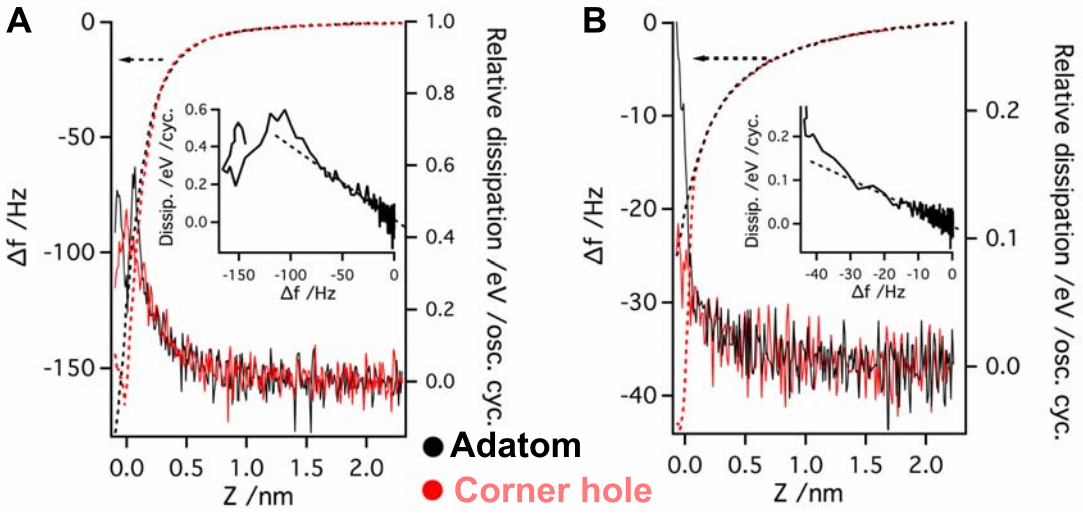

Figure 4.27: Relationship between frequency the shift and the dissipation for reactive tip termination (A) and also for the less reactive one (B). Dissipation is plotted with continuous line and the frequency shift with dashed. The corner hole data is marked with black and adatom with red color. On insets, the dissipation is plotted as a function of the frequency shift for the adatom data.

Using the linear dependence of the apparent dissipation signal on Δf, we can define a simple correction function independent of surface site. Using the correction function, we can subtract the apparent dissipation signal from data set. Bare short-range dissipation signal is plotted in Figure 4.28 together with the short range interaction for better comparison. The same correction function was applied for damping measured above the corner hole as well. The dissipation signal becomes flat after the correction at far distances. A minor increase of the dissipation signal appears on the onset of the chemical force above the adatom site. Therefore, we can attribute the origin of the dissipation signal to the adhesion hysteresis [181].

4.4.4 Summary

We introduced the origin of the so-called cross-talk phenomena in Section 4.1.2 and presented in Section 4.1.3 a modification of Omicron qPlus VT system, made to avoid this problem between the deflection and the tunneling current channels. The aim of this section was to prove that the microscope can work properly. The site-specific force/tunneling current measurements on the Si(1 1 1)–7×7 surface show an excellent agreement with the published results obtained with the optical beam deflection system. The sudden decrease of the tunneling current [175] caused by the formation of a covalent bond between the tip and the sample was clearly repeated, as in the previous work. Analysis of the dissipation signal shows that that the tunneling current does not induce artificial damping up to 100 nA at room temperature. The dissipation detected by

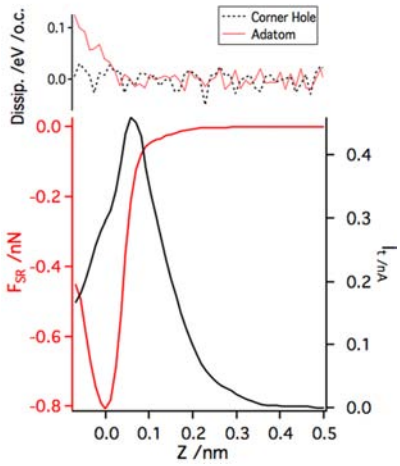

Figure 4.28: Corrected dissipation for damping measured above the adatom and above the corner hole. The corner hole shows only non-dissipative interactions. The adatom starts to show dissipation when the z approach reaches and exceeds the force maxima.

the amplitude regulator is the result of mainly two contributions. The first one, which has long range characteristic, is related with the instrumentation and it can be subtracted. The second one appears only above the adatom site after the tip approach exceeds the positions of the short range attractive force maxima. We attribute the latter one to the adhesion hysteresis [181].

4.5 Ethylene Attachment to Si(1 1 1)–7×7

4.5.1 Equilibrium Adsorption Geometry

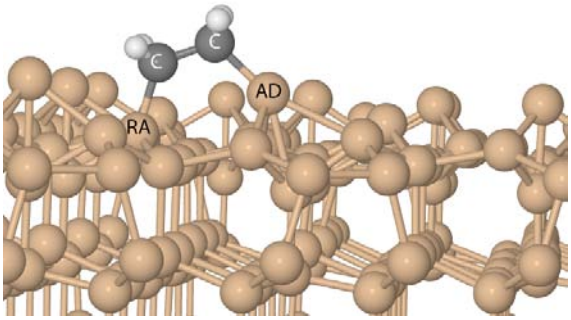

Figure 4.29: Ball-and-stick model representing the adatom–restatom adsorption configuration.

From DFT calculations, it is known that the ethylene molecule is adsorbed without decomposition in a bridge adatom–restatom position (Figure 4.29), with a single bond between C atoms, as the configuration with the lowest total energy. The BE E_b can be calculated as it was already shown for metals:

$$E_b = E_{clean} + E_{C_2H_4} - E_{ads}$$

where E_{clean} and $E_{C_2H_4}$ are the total energies of the clean 7×7 surface and an isolated ethylene molecule, respectively, whereas E_{ads} is the total energy of the surface with the adsorbed molecule. It was found that ethylene adsorption in the corner bridging site (Co–Re) to be only slightly preferable to ethylene adsorption in the center bridging site (Ce–Re); the binding energies being 2.41 and 2.34 eV, respectively. No difference in total energy between ethylene adsorption in the faulted and unfaulted subunit was found in the calculations.

The adsorption of ethylene on 7×7 results in structural deformations of both the surface and the molecule. The substrate deformation due to adsorption of a single ethylene molecule in the Co–Re position is shown in Figure 4.30 (left), where only vertical displacements of adatoms and restatoms larger than 0.02 Åare indicated. The restatom/adatom bonded to the molecule is displaced inward/upward by -0.42 Å and $+0.02$ Å, respectively. The other two adatoms near the molecule go upward from the surface by $+0.14$ Å. The structural changes for ethylene absorption in the Ce–Re position (not shown) are substantially the same. Calculations were also performed for two ethylene molecules in bridging sites within one unit cell half. For two molecules, there

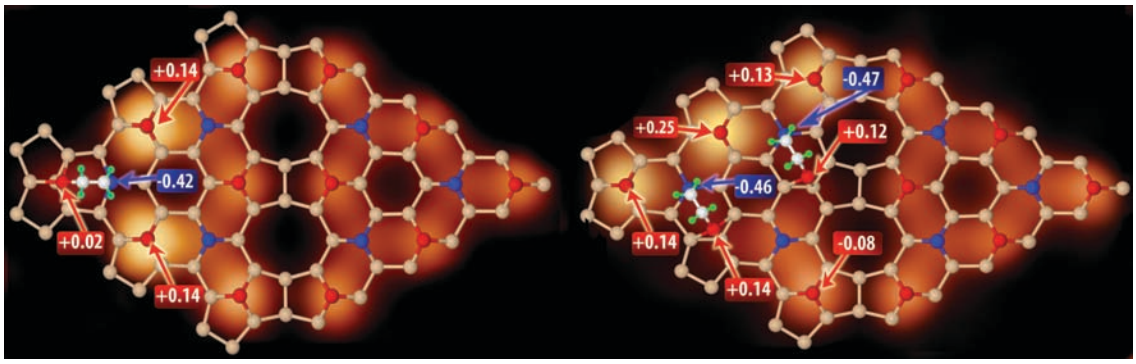

Figure 4.30: Vertical displacements of the silicon atoms (in angstroms) in the reacted half unit cell due to: (left) single ethylene adsorption in Co–Re position and (right) multiple ethylene adsorption (Ce–Re and Ce–Re configuration) with respect to Si atoms positions in the ideal Si(1 1 1)–7×7 surface. Vertical displacements below (0.02 Å are not shown). Calculated STM images (filled state, −1 V) are used as a background to emphasize the impact of molecular adsorption on STM scans.

are five different configurations, and no significant difference in the BE per molecule was found. This suggests that there is no additional barrier for multiple adsorption, for up to three molecules, within the same half of the 7×7 unit cell. The deformation induced by two ethylene molecules (Figure 4.30, right panel) is, in a first approximation, the superposition of the displacements induced by single ethylene molecule adsorption (compare with Figure 4.30, left panel). This suggests that the interaction between adsorbed molecules is small and that the BE E_b per molecule does not depend on whether there is a single or multiple adsorption.

Table 4.1: Equilibrium position of the adsorbed molecule*

$d(C_{Ad}–H)$	1.11	$d(C_{Re}–H)$	1.11
$d(C_{Ad}–H')$	1.11	$d(C_{Re}–H')$	1.11
$d(C_{Ad}–Si)$	1.99	$d(C_{Re}–Si)$	1.98
$\alpha(H–C_{Ad}–H')$	105.7	$\alpha(H–C_{Re}–H')$	105.4
$\alpha(C_{Re}–C_{Ad}–H)$	107.7	$\alpha(C_{Ad}–C_{Re}–H)$	108.2
$\alpha(C_{Re}–C_{Ad}–H')$	107.8	$\alpha(C_{Ad}–C_{Re}–H')$	108.1
$\alpha(C_{Re}–C_{Ad}–Si_{Ad})$	117.7	$\alpha(C_{Ad}–C_{Re}–Si_{Re})$	124.9
$d(C–C)$	1.64		
$\phi(C–C)$	1.2		

*All distances are in angstroms. The bond angles defined by the atoms in the brackets are represented by α, whereas ϕ represents the dihedral (torsion) angle.

Table 4.1 shows the calculated equilibrium geometry for the adsorbed molecule. The C−C bond length of 1.64 Å is close to the single carbon bond length of 1.54 Å of ethane (C_2H_6) in the

gas phase. Therefore, it can be concluded that C−C bond in the adsorbed ethylene molecule is a single bond. In general, the adsorbed ethylene molecule has a lower symmetry when compared with the corresponding hydrogen addition product (D_{3d} for C_2H_6). On metal (e.g., Ni(1 1 0)) and on Si(0 0 1)–2×1 surfaces, the molecule loses its three-fold axis, and the symmetry reduces to C_{2v}; an even stronger reduction in symmetry to C_2 (even C_1) might occur [134–137, 143]. In contrast with metal surfaces, the molecule can easily form a strong covalent bond with the silicon substrate, resonant states or Bloch states (if symmetrically allowed), leading to distortions of the molecule geometry [136,137]. In our case, the dangling bond state of the adatom and the restatom has different occupation including unsaturated dangling bonds on adatoms. The presence of these electronic states enhances the chemical reactivity of the surface. Molecules after adsorption no longer have two-fold symmetry (see Table 4.1 and C−C−Si angles) converting into C_s symmetry (strictly speaking, the mirror plane is gone as well, therefore C_1).

4.5.2 Scanning probe microscopy

To acquire more detailed information about the adsorption of ethylene on the Si(1 1 1)–7×7 surface, atomic-scale STM imaging was performed on the ethylene exposed surface. Figure 4.31 contains two images that were collected after the Si(1 1 1)–7×7 surface had been exposed to 250 L of ethylene at room temperature. They were collected with bias voltages that probe filled and empty states (−1.0 and +1.0 V, respectively). Counterintuitively, the chemisorbed molecules do not produce protrusions in the constant-current topographical images. Instead, they produce depressions, closely resembling Si adatom vacancies: when alkenes and small aromatic molecules chemisorb to the Si(1 1 1)–7×7 surface, the process of covalent bond formation shifts surface electronic states out of the energy range, close to the Fermi level, which is normally accessed by the tunneling electrons [142,189]. Consequently, the chemisorbed molecules image as depressions and the number of these features scales in a straightforward fashion with the ethylene exposure. For example, we found that the surface shown in Figure 4.31 had on average one Si adatom vacancy for every 14 7×7 unit cells before it was exposed to ethylene. After ethylene exposure, the average number of missing adatoms in each 7×7 cell increased to 1.33. In common with many other alkenes and small organic molecules, ethylene shows a preference for the faulted half on the 7×7 cell: the average number of missing adatoms after ethylene exposure divides unevenly into 1.17 and 0.15 for the faulted and unfaulted half unit cells, respectively. This uneven occupation of faulted/unfaulted half cells is known to be due to differences in the activation energy barrier for chemisorption from

a mobile precursor (physisorbed) state [190, 191].

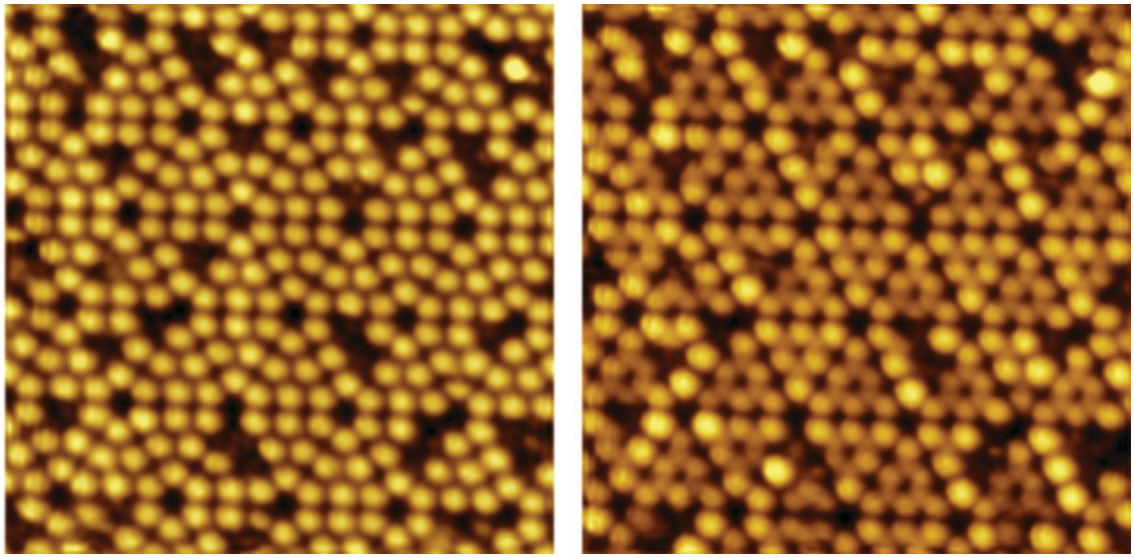

Figure 4.31: Constant current (0.65 nA) STM images after adsorption of 250 L of ethylene molecules. On the left side is an empty state image, on the right side is the corresponding filled state of the same area (13 nm × 13nm) recorded at a bias voltage of +1 and −1 V, respectively.

To demonstrate that ethylene, like many other molecules, images as a depression, calculated STM images using a fully relaxed Si(1 1 1)–7×7 surface for an ethylene molecule located in the corner bridging position are compared with the experimental results. Both the experimental high-resolution STM images (A–D) and the theoretical STM images (E,F) are presented in Figure 4.32. The Figure also includes cross-sectional cuts of the experimental occupied-state images of the 7×7 surface (from Figure4.32A) and of an ethylene molecule chemisorbed in the unit cell (from Figure 4.32C). The arrows on Figure 4.32A,C indicate the position and direction of the line-profiles. To make the calculations tractable, the STM images were calculated using periodic boundary conditions and a 7×7 supercell. To facilitate comparison of the theoretical and experimental images, the simulated 7×7 cell was tiled to fill the same area. Consequently, in Figure 4.32E,F, each 7×7 unit cell contains an ethylene molecule located in the corner-bridging site. There is clearly good agreement between the theoretical and experimental images, indicating that ethylene forms a bridge between the corner adatom and the nearest neighbor restatom. The formation of the covalent bond between the Si adatom and the ethylene molecules produces a suppression of the corner adatom. Contrastingly, the intensity of the nearest neighboring (center) adatom increases by ∼75 pm while the next corner adatom in the half unit cell remains largely unperturbed. These observations are in good agreement with the previous STM study [142], where it was also reported that adatoms neighboring the ethylene adsorption sites appear brighter in filled-state STM images.

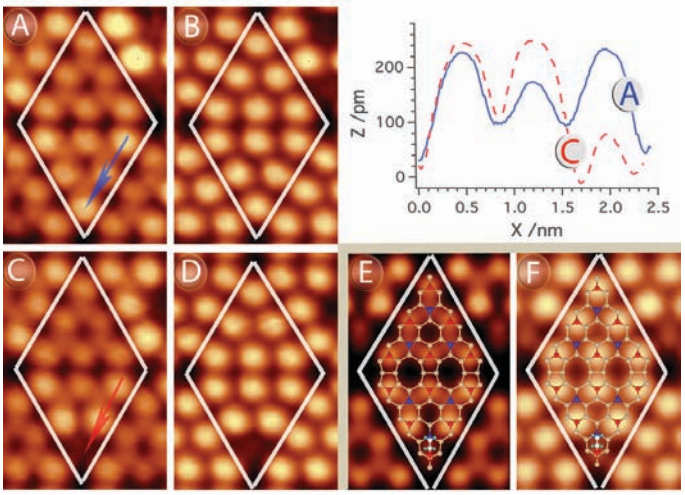

Figure 4.32: Comparison between experimental high-resolution STM(A–D) and calculated images (E,F). Filled (A,C,E) and empty states (B,D,F) were probed with bias voltage of -1.0 and $+1.0$ V, respectively. For experimental scans, a constant current of 0.65 nA was used. A and B represent an intact 7×7 unit cell, and from C to F an ethylene molecule was adsorbed in the corner adatom–restatom position. The reacted unit cell is repeated to fill the area in the case of the theoretical image. The cross-sectional cuts on the top are taken from the experimental occupied-state images of the 7 surface (from A) and of an ethylene molecule chemisorbed in the unit cell (from C). (Arrows are indicating the position and direction of the line profiles.)

Our calculations indicate that the presence of the ethylene molecule induces an upward movement of the nearest neighbor adatoms (Figure 4.30) and a small downward shift of the dangling bond state. Therefore, the enhanced contrast in the filled state images for the nearest neighbor adatoms is caused by both vertical relaxation and changes in the electronic LDOS. The Si adatoms that form covalent bonds with the ethylene molecule image as depressions because the dangling bond states associated with the adatom/restatom are shifted downward in energy (see Figure 4.38). The impact of molecular adsorption on the surface electronic structures will also be discussed in the section following.

As it was already mentioned, the characteristic signature of small molecule attachment makes the distinguishing from missing Si adatoms very difficult. In contrast with STM, atomic force microscope (AFM) has already achieved high-resolution images of individual molecules on surfaces [192]. In addition, AFM with the help of DFT has excellently performed chemical identification of individual atoms [2]. In order to clearly identify the adsorbed species, measurements were performed also by using a tuning fork based (qPlus) AFM/STM capable of recording tip-sample interaction force and tunneling current simultaneously. In Figure 4.33 maps of tunneling current and frequency shift (force) are visible after a deposition of 50 L of ethylene at RT. The scanning was performed in quasi constant height mode (with slow Δf feedback). Here constant height scan-

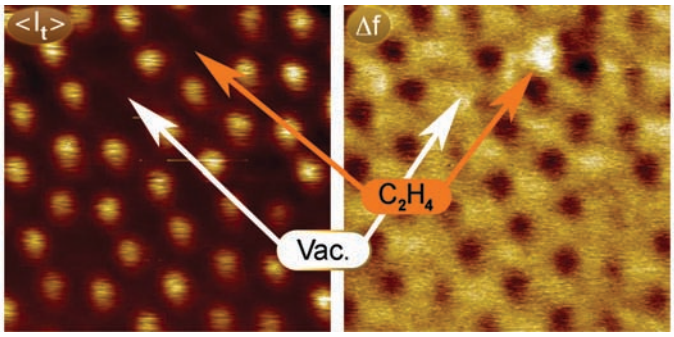

Figure 4.33: Simultaneously recorded map (5×5 nm^2) of the tunneling current and frequency shift (force) after a deposition of 50 L of ethylene at RT. The scanning was performed in quasi constant height mode (with slow Δf feedback). In the tunneling current channel only missing adatoms can be observed, whereas in Δf; in one case there is no short-range force contribution, in the other case a bright protrusion appears. They can be attributed to a adatom vacancy and adsorbed ethylene molecule, respectively. For more details see text.

ning is inevitable because the force and the tunneling current has different dependance on the tip sample separation. Therefore with any kind of Z regulation (I_t or Δf) physical interpretation of the images becomes difficult.

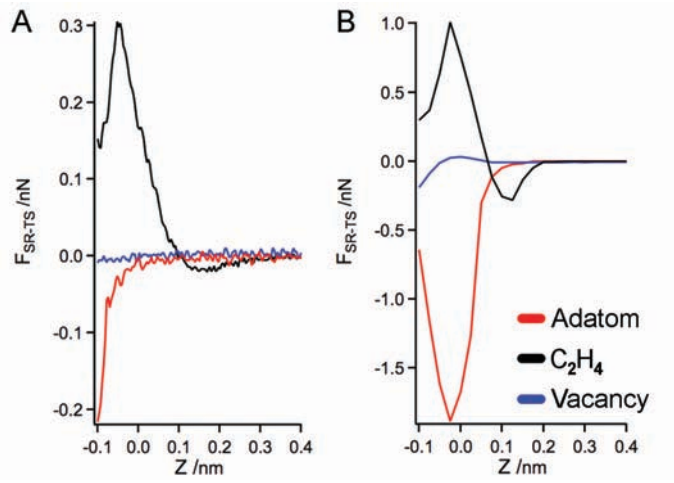

Figure 4.34: Force site spectroscopy measured over an unreacted adatom, molecule (bright protrusion in Figure 4.33 Δf map) and vacancy. From the comparison of the experimentally recorded spectrums (A) and the ones obtained by DFT (B), the adatom vacancy and the adsorbed C_2H_4 molecule can be clearly distinguished.

In the tunneling current channel only missing adatoms can be observed as before, whereas in Δf; in one case there is no short-range force contribution, in the other case a bright protrusion appears. The bright contribution refers to repulsive force component, in contrast with the dark features, which is attractive, observed over the adatoms. To get better understanding of acting forces, the force site spectroscopy is plotted in Figure 4.34A with the corresponding simulated

(DFT) spectrums as well (B). Similarly as shown in the previous chapter, the adatom gives strong attractive force contribution (only the force maxima is not shown here again to have better scaling with the force acquired over the molecule). Over the molecule only a very weak attractive force appear and mainly the repulsive interaction acts along tip approach, while there is no repulsive interaction (or attractive neither) over vacancy sites at the same tip-sample distance. Based on force site spectroscopy combined with DFT, the adsorbed molecules can be clearly distinguished from the adatom vacancies. In fact, the bright protrusion in Δf map occupies not only the position of the (center) adatom but extend to the rest atom as well giving further strong evidence for the adatom-restatom adsorption shame.

4.5.3 Valence Band

Because of the strong lifetime broadening and band dispersion caused mainly by electron phonon interaction near the Fermi level at the Si(1 1 1)–7×7 [193], it is not a simple task to give a precise description for the adsorption effects in this region. The influence of the temperature on the adatom states has been investigated already, and it was found that at low temperature the adatom peak clearly splits into two components (usually labeled as S_1 and S_1') that are separated by 0.20 to 0.25 eV: this is the difference in the dangling bond energy between the corner and the center adatoms [193, 194]. Moreover, a detailed analysis of the LDOS of 7×7 in real space made by the combination of phase-sensitive lock-in technique with STM was also in very good agreement with these photoemission findings [195].

Figure 4.35 shows angle-resolved valence band spectra for the clean 7×7 reconstructed surface (top) and after 500 L of adsorption of ethylene (bottom). To obtain better resolution for the surface states, the sample was cooled down to the temperature of 110 K during the data acquisition. The two well-known surface peaks, S_1 ($\sim$0.12 eV) and S_2 ($\sim$0.85 eV), correspond to adatoms and restatoms, respectively [196, 197], and at the emission angle of 36° the S_1' (0.22 eV from S_1) surface state is clearly distinguishable. After a 500 L dose of ethylene, the intensity at the Fermi level strongly decreased, and also S_2 dropped to approximately half of its initial value, which is in good agreement with previous studies [138, 144]. Note that the adsorption strongly affects the electron population at the Fermi level; therefore, the position of the restatom peak (fixed at 0.85 eV) should be used as an energy reference for all intermediate coverage. Furthermore, because of the effect of the temperature on the Fermi edge (shift and broadening), the same fixed position for the restatoms was used at room temperature to get comparable and more accurate results.

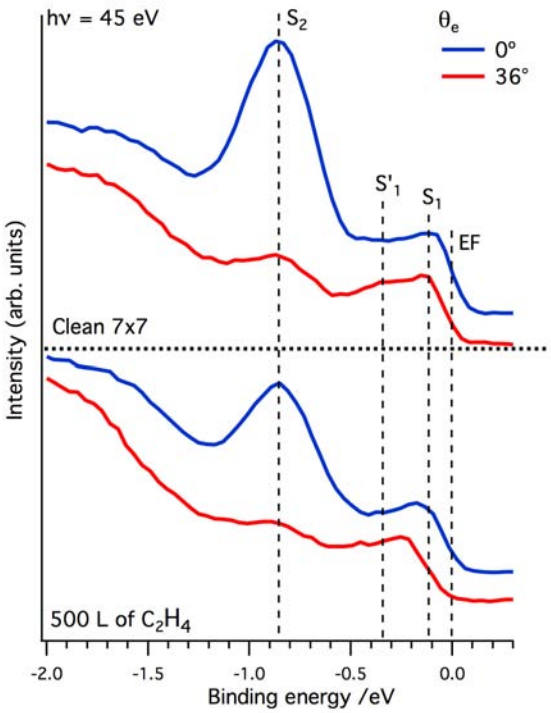

Figure 4.35: Angle-resolved valence band spectra taken at the temperature of 110 K from the clean 7×7 (top) and after 500 L of C_2H_4. At this temperature, the surface state S_1' rising from the corner adatoms is clearly resolved. These adatoms show much lower reactivity for adsorption.

Interestingly, the adsorption of ethylene has a less visible effect on the band around S_1. The 7×7 unit cell contains three (or five by separating the faulted and unfaulted halves) types of dangling bonds. In each unit cell, there are 6 dangling-bond electrons associated with the restatoms, 12 with the adatoms, and finally 1 dangling-bond electron with corner holes. We have already seen from the STM results that ethylene adsorbs preferably on the center adatoms. Therefore, the remaining population of electronic states at the Fermi level can be explained with the 2:1 ratio between the intact corner adatoms (S_1') and center adatom (S_1). In Figure 4.36, we present the evaluation of electronic structure of characteristic surface states with increasing coverage. The spectra were taken at room temperature after adding C_2H_4 sequentially to the surface and are shown for emission angles of 0° and 36°. From 2000 L, there is no more significant contribution from the S_2 state. Three adatom–restatom adsorption positions per half 7×7 unit cell are occupied by ethylene. The remaining dangling bonds located at the position of the intact adatoms are responsible for the nonzero electron density at the Fermi level.

Three sets of spectra recorded at 110 K using a photon energy of 45 eV for emission angles from 0° (up) to 60° (bottom) are shown in Figure 4.37. The first one on the left side corresponds

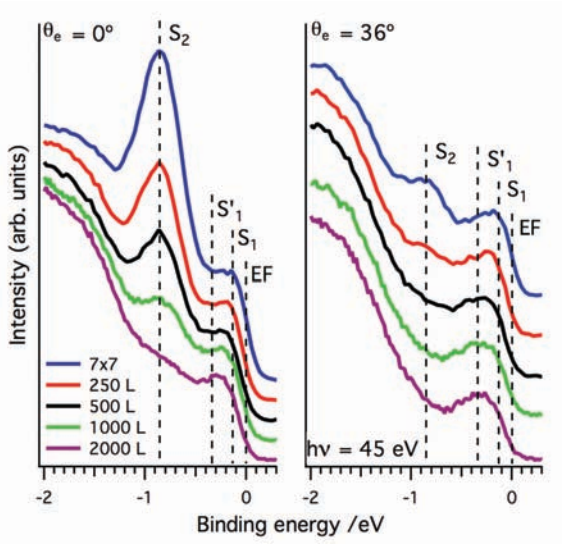

Figure 4.36: Series of valence band spectra collected from the Si(1 1 1)–7×7 surface exposed to increasing doses of C_2H_4 at RT.

to the clean Si(1 1 1)–7×7 reconstructed surface, the center one to 500 L, and the one on the right side to 2000 L adsorption of ethylene. The dashed vertical lines correspond to the positions of the adsorption-induced states as well as to the 7×7 surface states that were discussed above. The adsorption related peaks are at the following positions with respect to the Fermi level: 1.0 (A_1), 4.0 (A_2), 5.8 (A_3), and 7.5 (A_4) eV. For comparison, the clean spectra are presented as well. The corresponding calculated projected density of states for the carbon and silicon atoms (restatom, adatom) is shown in Figure 4.38.

The first state assigned (A_1) is the closest one to the Fermi level and is predicted by theoretical calculations to be a previously unreported resonant state between the upper carbon atom and, in this particular case, the center adatom. (See PDOS of the carbon atom and the adatom in Figure 4.38.) The position of peak A_1 makes its identification difficult because the broad peak, which corresponds to the restatoms (S_2) of the clean substrate, makes it impossible to clarify the validity of this prediction at any intermediate coverage. To overcome of this problem, one has to saturate all restatoms within the unit cell by increasing the dose of molecules to 2000 L (see coverage dependence in Figure 4.36). At this coverage, a clear peak appeared at 1 eV(A_1) below the Fermi level (0° spectrum of 2000 L in Figure 4.37). All remaining assignments can be clearly made from the comparison with the clean surface and from the coverage dependence between 500 and 2000 L.

For differentiation, around peaks A_2, A_3 and A_4 were also found and assigned as adsorption driven states in the work of Widdra *et al.* for C_2H_4/ Si(0 0 1) [136]. In their study, they found a

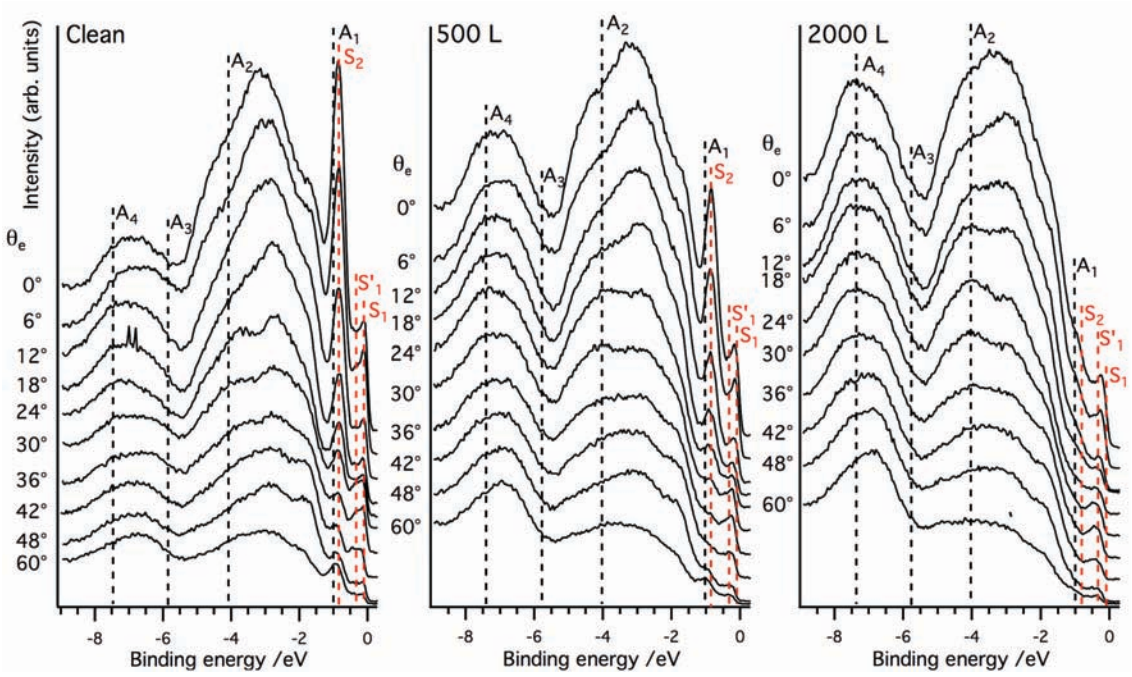

Figure 4.37: Angle-resolved photoemission spectra for clean Si(1 1 1)–7×7 (left), after 500 L (center) and after 2000 L adsorption of ethylene. Three sets of spectra shown for emission angles from 0° (top) to 60° (bottom). The spectra were recorded at 110 K using a photon energy of 45 eV. The marked positions correspond to the adsorption induced states they are present on the clean spectra as well to facilitate comparison.

quite significant dispersion (∼0.8 eV) at the position of A_4 (marked as $1b_{2g}$) due to the significant lateral interaction between the molecules and to the formation of adsorbate Bloch states. The reason for that the 7×7 is different is related to the different adsorption geometries and large intermolecular distances, even at the saturation of all adatom–restatom sites. Therefore, in the case of the adatom–restatom model, the lateral interaction between the molecules is not significant, contrary to the densely packed molecular layer on C_2H_4/ Si(0 0 1) [136].

Finally, the origin of the molecular states can be understood by using the projected density of states shown in Figure 4.38. First of all, in good agreement with the experimental data, the adsorption clearly reduces the intensity of the S_2 (restatom state). Moreover, also according to calculations, the density at the Fermi level is strongly reduced because of the cycloaddition of the π bond to the adatom dangling bonds. Turning to the molecular driven states, A_1 has the lowest BE, and according to the calculated intensities it is partially localized with an approximately 1:1.2 ratio on the C atom bonded to the adatom and on the bonded adatom itself. Beside the strong substrate contribution in this region, the delocalization makes even more difficult the identification in ARUPS. The formation of A_2 is mainly due to changes in the density of states of the restatoms.

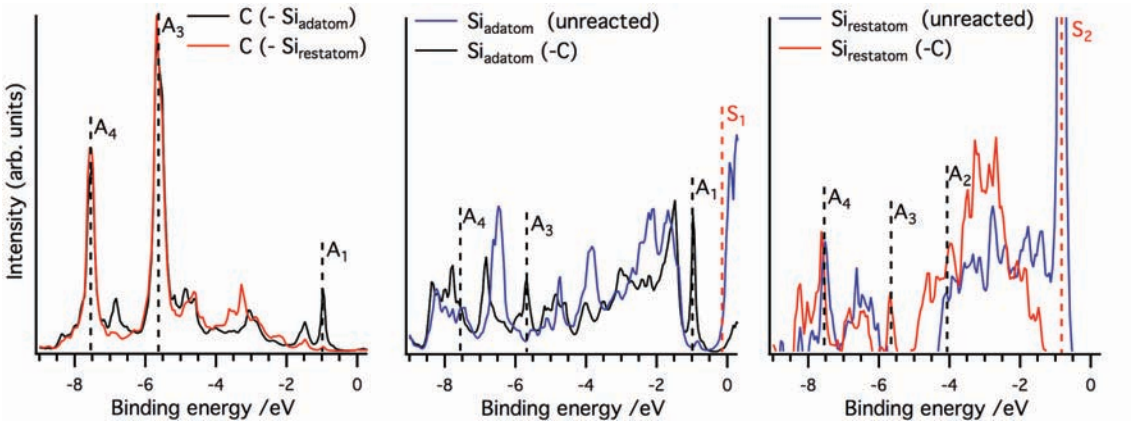

Figure 4.38: Calculated projected density of states (PDOS) for the carbon and silicon atoms. The molecule bridged one of the center adatom and restatom position (see Figure 4.29).

Both experimental and theoretical data show modification of the intensity of bands between 2 and 5 eV, but there is no strong carbon state in this region. (See C PDOS in Figure 4.38) Therefore, it can be concluded that in this regime the adsorption-induced surface state modifications (shifts) are dominant. The last two, A_3 and A_4, are strongly localized on the C atoms. Beside both states being strongly localized, A_3 is less pronounced in the measured spectrum because of the intense surface contribution on the higher binding side. As a result, it gives only a shoulder in experiment.

In summary, ARUPS (or better to say AR-SRPES) combined with DFT can produce a better understanding of the adsorption-induced electronic effects. Specifically, A_1 (instead of A_3) is related to the donation of electrons to the lowest unoccupied state of the free ethylene molecule, LUMO ($1b_{3g}$). A_3 originates from the interaction with highest occupied molecular orbital of the ethylene molecule, HOMO ($1b_{2u}$), and A_4 is derived from the interaction with the lower laying $1b_{2g}$ state; in the case of the Si(1 1 1)–7×7 substrate, both remain strongly localized states on the C atoms.

4.5.4 Core Levels

A typical C 1s spectrum with fitted curves is presented in Figure 4.39. A constant Lorentzian width of 0.2 eV and Gaussian widths of 0.58 (±0.1 eV) were used for the Voigt fitting functions, and the energies of the presented peaks are given relative to the main component at the position of 283.95 eV. The main peak is related to the formation of the Si−C bond, and the second largest component separated by 0.5 eV is attributed to the C−H vibrational loss feature. Previously on Si(1 1 1)–7×7, this loss feature was found at 0.48 eV [145], on Si(0 0 1)–2×1 at 0.43 eV [139], and for the gas phase molecule at 0.4 eV [198]. A third peak with the smallest intensity is located

around 1.1 to 1.2 eV with respect to the main component. The origin of this peak may be a small amount of contamination coming from the gas line or residual gas. Alternatively, overtones of the C−H stretch were shown to be excited for adsorbed C_2H_3 (ethylidyne) on Rh(111) [199] and were clearly observable on methyl-terminated Si(111) [200]. Unfortunately, because of the quite high level of noise (related to the low intensity of the synchrotron radiation above the carbon edge), it is not possible to determine unambiguously the origin in this work, and it needs further SXPS investigations. Lastly, a slight increase in the noise level appears on the low binding side of the main peak, suggesting that a very small portion of the molecules might undergo dissociative adsorption.

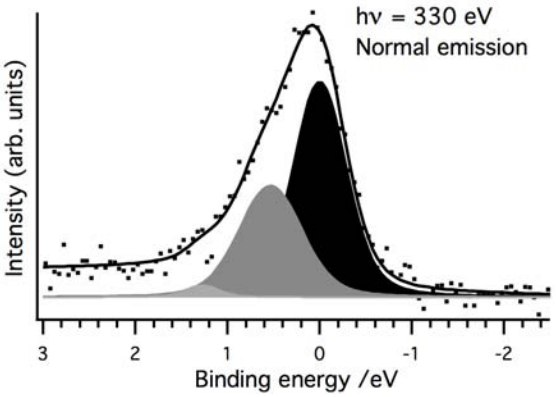

Figure 4.39: C 1s spectrum with curve fitting analysis obtained at room temperature after a 500 L dose of ethylene. The energies of the presented peaks are relative to the main component at the position of 283.95 eV.

Because of the very complex nature of the Si 2p spectrum and the relatively low surface coverage, even at the saturation of all adatom–restatom pairs (0.2 ML) it is nearly impossible to give a correct description of the adsorption-induced changes in the Si 2p core levels with only nonlinear curve fitting analysis. To make it much easier to follow the adsorption-induced changes, we subtracted the clean spectrum from spectra taken after 250, 500, 1000, and 2000 L of adsorption of C_2H_4 and presented at the top of Figure 4.40 with the reference spectrum of clean Si(1 1 1)–7×7 and its known fitted curves at the bottom. Usually the curve fitting analysis of the clean 7×7 results in a bulk (B) and five surface components (C_1–C_5) [194]. In our case, it was necessary to use two components (C_2 and C_2') for the tail at the low binding side, similarly to the fitting result presented by Le Lay *et al.* [201]. Among all major studies, there is a good agreement about the assignment of C_2 (to restatoms) and C_3 (to adatoms), which are in main interest [194, 202]. From the difference spectra, it is clear that the C_2 state is quenched with the adsorption, and after a dose of 2000 L, it has almost completely vanished giving a good agreement with our previous

assumption for the saturation coverage.

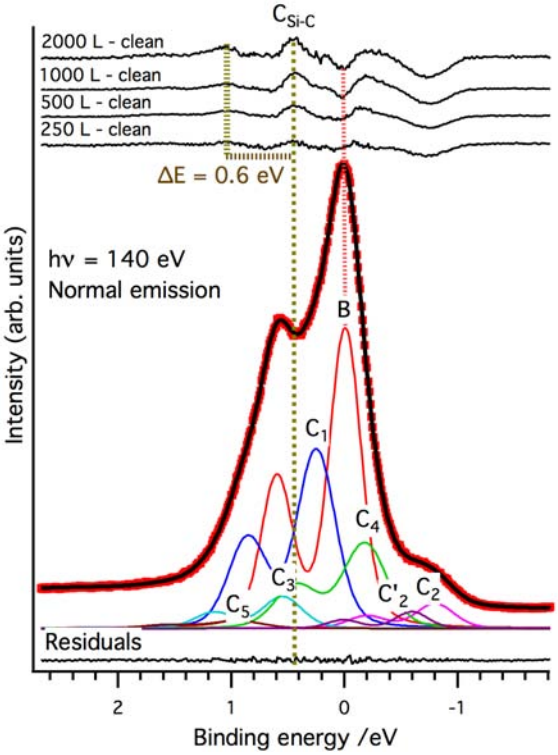

Figure 4.40: C 1s spectrum with curve fitting analysis obtained at room temperature after a 500 L dose of ethylene. The energies of the presented peaks are relative to the main component at the position of 283.95 eV.

Beside the continuous drop of the restatom peak, a new peak (C_{Si-C}) starts to appear, which is separated by 0.44 eV from the bulk component, and as the coverage increases, also the $2p_{1/2}$ part is evident. We have to note here that none of the previous Si 2p core level studies reported any peak assigned to the Si−C bond in the Si 2p band for ethylene on Si(1 1 1)–7×7 [138,144,145]. Moreover, in the work of Kim *et al.*, a slight shift was present for the surface peak related to adatoms (C_3) in their fitting analysis, and the position of this component moved to 0.51 eV BE with respect to the bulk component Si(1 1 1)–7×7 [145]. Because of the relatively small energy difference between C_3 and C_{Si-C}, the new 0.51 eV (fitted) position of the C_3 can be obtained with a doublet filling the two components in the middle with slightly higher Gaussian width. This observation can evidently represent the possible arbitrariness of the fitting-based analyses for this system with moderately low-energy resolution. From our point of view, the change in this energy region is clearly related to the formation of the Si−C bond. This interpretation can be made based on the fact that the C_{Si-C} peak grows continuously in the same position (no band bending) from very small coverage until the saturation of all adatom–restatom positions, and we

observed no adsorption-induced reconstruction with STM. For alkyl-terminated Si(1 1 1) surfaces, the chemical shift of the Si−C bond was found to be 0.25 to 0.30 eV [200, 203, 204]. Besides having in both situations an sp^3 hybridized C atom attached to the silicon substrate, the load charge differs slightly, which leads to a variation of the chemical shift. Another correlation can be made with Si(0 0 1) supporting C_2H_4, where the surface core level shift is only 0.18 eV from the bulk Si 2p [139], representing also a difference in the electronic structure between the di-σ bonded ethylene and adatom–restatom bonded on Si(1 1 1)–7×7.

4.5.5 Summary

In summary, we have investigated the reliability of the adatom–restatom bridging scheme for ethylene on Si(1 1 1)–7×7. Our STM measurements were in excellent agreement with previous findings in the sense that the reaction leads to a decrease in the number of observable adatoms on the surface [142]. With our high-resolution images, it is clear that the restatom neighbors must also be directly involved in the reaction, and the simulated STM images suggest exactly the same behavior. Furthermore the application of the combined AFM/STM mode helped us to distinguish between adatom vacancy and adsorbed molecule that sits in fact exactly in the supposed position. On one hand, in the valence band PES spectra we have also seen quenching of the corresponding surface states in good agreement with previous studies [138, 144]. On the other hand, from low-temperature, angle-resolved photo-emission spectra, it is clear that the S_1 surface components quench much faster than the S_1' component (corner adatoms), especially at low coverage. The remaining electronic states close to the Fermi level originate from unsaturated adatoms. Although there is no significant energy difference between the adsorption sites, the center adatoms preferentially react during the adsorption process because the population of the central adatom-restatom adsorption configuration is two times higher than that of the corner adatom-restatom configuration. Furthermore, there is clearly a preference for the faulted half cell despite the fact that there is no difference in BE between the faulted and unfaulted half cells. This phenomenon is not uncommon and is normally explained in terms of different site-dependent activation energy barriers for chemisorption from the mobile precursor state [190, 191].

Additionally, our core level study has shown the existence of the peak clearly correlated with the formation of the Si−C bond, and we have seen good agreement for the C−H stretching loss feature in C 1s core level with the possibility of the existence of higher harmonic modes.

"We can know only that we know nothing. And that is the highest degree of human wisdom."

Leo Tolstoy, War and Peace

5

Conclusions

In this work the main interest was directed towards the investigation of the adsorption of metals and molecules on oxide and semiconductor surfaces. Among the huge variety of suitable oxide supports, as a model material, $TiO_2(1\,1\,0)$ was choosed to investigate in detail the adsorption of metals. This topic derives from the fact that the understanding of metal/TiO_2 systems has a huge impact on development of catalysts of high performance, moreover, that of solar and hydrogen fuel cell fabrication [4].

By deposition of potassium and investigation of thermal treatments, we characterized the morphological effects of a typical alkali additive used widely in the heterogeneous catalysis. As results, it was shown that the adsorption of potassium leads to the formation of dark protrusions visible on empty state STM images. This observation can be explained by a partial charge transfer from K atoms to the substrate. Auger electron spectroscopy (AES) and thermal desorption spectroscopy (TDS) measurements have shown that the desorption energy of K decreases with the coverage via the decrease in the heat of adsorption. Interestingly, the annealing of the K covered surface to 900 K leads to the formation of the reduced 1×2 reconstruction and to the presence of terrace decoration, depending on the initial K coverage. This observation strongly suggest that potassium may create both $K-O_x$ and $K-Ti_xO_y$ compounds and leaves the surface also in this form. The phase transition is apparently fully reversible because by annealing the substrate to 1100 K the original 1×1 bulk terminated surface can be regained. The possibility of controlling the substrate properties opens further interesting ways to improve the desired behavior of a catalytic system [205].

In addition, the decoration/encapsulation process of the Rh nanoparticles supported on $TiO_2(1\,1\,0)$ surface was studied by atomic scale scanning tunneling microscopy. In this latter topic, there is an internationally strong activity for better understanding of the formation of oxide ultrathin films on noble metal nanocrystallites supported on reducible oxides (phenomena of decoration and strong metal-support interaction, SMSI) [4, 5]. We found that on the giant particles, which were grown by postgrowth of Rh on a $TiO_2(1\,1\,0)$ surface (initial deposition of a small portion of Rh followed by larger deposition at elevated temperature), mainly the quasi-ordered, "worm-like" texture was found. In another case, in which the Rh particles were grown on a $TiO_2(1\,1\,0)$–1×1 surface (without preseeding), hexagonal wheel structure was recorded. This complex wheel structure can be attributed to a moiré-like pattern formed by the slight misfit between the atomic lattice of the metal particles and the overlayer oxide. With a quite new approach, it was possible to selectively remove the "wheel-like" decoration layer by Ar^+ sputtering (0.5 keV, 3 $\mu A/cm^2$) and to subsequently restore it by a short thermal treatment at 1000 K. At $600 - 700$ K the surface of the Rh nanoparticles becomes flat but it is not yet covered by TiO_x layer. Apparently, the decoration process starts at $800 - 850$ K.

The SiC surface has a strong technological significance in production of electronic devices and catalysts [6, 7]. Ethylene can act as a source of carbon for the production of SiC. In an effort to more fully understand the ethylene/silicon system, ethylene adsorption on $Si(1\,1\,1)$–7×7 was also investigated. It was shown that the adatom-rest atom adsorption shame is the dominant (at least at low coverages). Furthermore, it is quite evident now, that adsorbed molecules can be clearly distinguished from the adatom vacancies with the help of AFM and also the adorption position is undoubtedly identifiable in the frequency shift maps. A future task is reaching further levels at, which even different molecules can be discriminated from one another.
On the other hand, from low-temperature, angle-resolved photo-emission spectra, it is clear that the S_1 surface components quench much faster than the S_1' component (corner adatoms), especially at low coverage. The remaining electronic states close to the Fermi level originate from unsaturated adatoms. Although there is no significant energy difference between the adsorption sites, the center adatoms preferentially react during the adsorption process because the population of the central adatom-restatom adsorption configuration is two times higher than that of the corner adatom-restatom configuration. Furthermore, there is clearly a preference for the faulted half cell despite the fact that there is no difference in BE between the faulted and unfaulted half cells.

Among characterizations of surface properties, proper working mechanism of the instrumenta-

tions needs to be ensured. The recent development of the qPlus AFM technique enabled simultaneous acquisition of interaction forces and tunneling current [8]. However, this setup requires special attention to avoid so-called cross-talk effect between the current signal and the deflection channels. The origin of this phenomena is related to the speed limit of the current to voltage converter used for tunneling current detection and to the stray capacitance between the internal connections of the microscope. A modification of Omicron qPlus VT system was made to avoid the crosstalk between the deflection and the tunneling current channels. In the new design of the sensor, the current to voltage converter of STM is connected directly to the tip with a gold wire. Beside separating the tunneling current signal, it was necessary to replace the original ceramic support by a metal one in order to reduce the capacitive coupling between the channels.

To prove that the microscope can work properly, site-specific force/tunneling current measurements on the Si(1 1 1)–7×7 surface was shown with an excellent agreement with the published results obtained with the optical beam deflection system. The sudden decrease of the tunneling current [175] caused by the formation of a covalent bond between the tip and the sample was clearly repeated, as in the previous work. From the analysis of the dissipation signal, it was clearly demonstrated that that the tunneling current does not induce artificial damping up to 100 nA at room temperature. The dissipation detected by the amplitude regulator is the result of mainly two contributions. The first one, which has long range characteristic, is related with the instrumentation and it can be subtracted. The second one appears only above the adatom site after the tip approach exceeds the positions of the short range attractive force maxima. The latter one can be attributed to the adhesion hysteresis.

„Az emberek jövője és a magad sorsa titok - így kell lennie; de élj úgy, hogy mindig kész légy mindenre."

Lev Tolsztoj: Háború és béke

6

Magyar nyelvű összefoglaló (Hungarian resumé)

A jelen disszertáció a technológiai szempontból fontos fémek és molekulák oxidokon és félvezető - kön lezajló adszorpciós folyamatainak a vizsgálatára irányult. A számos lehetséges oxid hordozó közül a $TiO_2(1\,1\,0)$ felületet tanulmányoztuk részletesen. Ezen felület önmagában is, de különösen a fém/TiO_2 rendszerekben, kitüntetett szerepet játszik a nagyhatékonyságú katalizátorok kifejlesztésében, továbbá napelemek és üzemanyag cellák kialakításában [4].

A kálium $TiO_2(1\,1\,0)$ felületre történő párologtatásával és az így kezelt minta hőkezelésével tanulmányoztuk annak hatását a felület morfológiai tulajdonságaira. Ezen vizsgálataink hátterét az adja, hogy az alkáli vegyületeket igen kiterjedten alkalmazzák adalékanyagként a heteroén katalízisben. Munkánk eredményeként azt kaptuk, hogy a kálium adagolásával bemélyedések keletkeznek a betöltetlen állapotsűrűséget megjelenítő STM képeken. Ez a jelenség a hordozó irányába történő elektron átmenettel magyarázható. A termikus deszorpciós spektroszkópiai (TDS) és Auger-elektron spektroszkópiai mérések azt mutatták, hogy a K-deszorpció aktiválási energiája csökken a felületi borítottsággal. Érdekes módon a káliummal borított felület 900 K-re történő felfütés hatására a kindulási K koncentráció függvényében rekonstruálódik a redukáltabb 1×2 szerkezetté vagy akár kiterjedt bemélyedések keletkeznek a hordozó terasz szerkezetében. Ezen utóbbi megfigyelés erősen azt sugallja, hogy a kálium nem csak $K-O_x$ formában hanem $K-Ti_xO_y$ formában is elhagyhatja a felületet. A K-mal dotált $TiO_2(1\,1\,0)$ felület 1100 K hőmérsékletre történő hevítés hatására visszaalakul a kiindulási 1×1 tömbi szerkezetűvé, habár a felületen kissé megnövekedett számban fordulnak elő hibahelyek. A felület ily módon történő oxidációja a tömbi oxigén felületi szegregációjával magyarázható. Azzal, hogy a hordozó felületi tulajdonságai jól definiáltan

megváltoztathatóak érdekes lehetőségek nyílnak a fém/oxid katalitikus rendszerek további finomhangolására [205].

Elsőként mutattuk ki a rendezett TiO_x réteg jelenlétét hordozott Rh nanorészecskéken, mindezt a Rh-mal borított felület 1050 K-re történt felfűtés hatására. Ez a felismerés alátámasztja, hogy a rendezett 2D oxid filmek megjelenése általánosnak mondható a redukálható oxidokon hordozott nemesfémek felületén. A nagy felbontású STM leképezésnek köszönhetően azonosítani lehetett a telítési dekorációs réteg szerkezetét: az un. „kocsikerék (wagon-wheel)" szerkezet $\sim$1.5 nm $\times$ 1.5 nm hexagonális elemi cellákból épül fel és a „kerekeket" három háromszög építi fel melyek mindegyike 5 atomot tartalmaz egymástól 0.31 nm távolságra. Ezen komplex „kocsikerék" szerkezet Moiré tipusúnak tekinthető mely két, különböző atomi rács illeszkedési hibájából adódik. Megfigyeltük a nem telített rétegek „féreg-szerű (worm-like)" szerkezetét is. Ezen felületi formák 1D nanoszerkezeteknek tekinthetőek és a szorosan pakolt Rh(1 1 1) rácsára illeszkednek. Hosszuk általában 2–3 nm és mindössze 0.5 nm szélesek. Ezt a részlegesen telített réteget a „kocsikerék" szerkezet prekurzor állapotának tekinthetjük. Egy újszerű kísérlet keretében, kis energiájú és intenzitású Ar^+ bombázással (0.5 keV, 3 $\mu A/cm^2$) sikerült szelektíven eltávolítani a magas hőmérsékleten kialakult dekorációs réteget és megfigyelni a dekorációs réteg kialakulását 1000 K-re történő fokozatos felfűtéssel. 600 - 700 K hőmérsékleten a Rh nanorészecskék felülete kisímul, de a TiO_x réteg még nem jelenik meg. A dekorációs réteg növekedését $800 - 850$ K hőmérsékleten tapasztaltuk.

A szilícium-karbid számos fontos technológiai alkalmazása ismeretes, mind a mikro és nanoelektronikában, mind heterogén katalitikus rendszerekben [6, 7]. Az etilént kiterjedten alkalmazzák szénforrásként a SiC előállítása során. Ennek megfelelően részletesen vizsgáltuk az etilen Si(1 1 1)–7×7 felületén történ őadszorpcióját. Kimutattuk, hogy a felületen található Si adatomok látszólagosan száma csökken az etilén és a Si(1 1 1)–7×7 hordozó közötti reakció hatására. Továbbá, az STM felvételek egyértelműen bizonyították, hogy az adatomok melleti alacsonyabb rétegben elhelyezkedő atomok (restatom) is résztvesznek a reakcióban és a kísérleti eredményeket kitűnően alátámasztják a szimulált STM képek (DFT) is. Tovább erősítve a javasolt mechanizmus helyességét, az atomifelbontású AFM képeken jól láthatóan a molekula a javasolt „adatom-restatom" adszorpciós pozícióban helyezkedik el. Az AFM és az STM kombinációjának révén könnyen meg lehet különböztetni az adatom hibahelyeket az adszorbeátumhoz kötődő adatomoktól. Ezt a módszert a jövőben tovább lehet fejleszteni úgy, hogy a felületen adszorbeálódott, különböző molekulák is felismerhetőek legyenek (molekuláris felismerés). Eredményeink jól illusztrálják az SPM módszerek rendkívüli hasznosságát az adszorpciós mechanizmus pontos felállítására.

PES mérések során megfigyeltük, hogy a reakció hatására csökken az „ad" és „rest" atomokhoz rendelhető csúcsok intenzitása a vegyérték (valencia) sávban. Továbbá, sikerült egyértelműen kimutatnunk a kilépő elektronok szögeloszlásából, hogy az S_1 felületi állapot, ami a centrális helyzetű adatomokhoz rendelhető, sokkal gyorsabb intenzitás csökkenést mutat a reakció előrehaladtával, mint a S_1' állapot (kűlső, „corner" adatomok), főként alacsony borítottságoknál. Annak ellenére, hogy az adszorpciós helyek között nincs energetikai különbség a centrális adatomok preferáltan reagálnak az adszorpció során mivel a rájuk vonatkozó adszorpciós helyek száma kétszer akkora mint a kűlső adatomok esetében. A Si 2p héj PES spektrumában jól kivehető a Si−C kötés megjelenése és jó egyezést találtunk az előzőleg kimutatott C−H veszteségi csúcs helyét illetően a C 1s sáv vizsgálata során.

Az adszorpciós folyamatok vizsgálata során rendkívül fontos az alkalmazott módszerek helyes működéséről meggyőződni. Manapság a piezoelektromos atomi erőmikroszkóp (AFM) szenzorok egyszerűségük révén egyre nagyobb népszerűségre tesznek szert. Továbbá, AFM és STM felvételek párhozamos felvételét teszik lehetővé mély-, szoba- vagy akár magas hőmérsékleteken. Sajnálatos módon, az alagútáramot és a rezgő konzol mozgását vivő jelcsatorna közötti elektronikus áthallás komoly kísérleti problémához vezethet. Munkámban áramkör szimulációkkal illusztrálva részletesen elemeztem az áthallás eredetét és néhány javaslatot tettünk ezen hiba elkerülésére. Rámutattam, hogy az áthallás mértékét főként az STM áram/feszültség konverterének kimeneti feszültség-ugrási sebessége („slew rate") és a mikroszkóp belső vezetékei közötti szórt kapacitás határozza meg. Ezt elkerülendően, egy lehetséges eljárást is bemutattunk, amely az Omicron qPlus mikroszkópban az áthallás mértékét a minimálisra képes csökkenteni. Ebben az elgondolásban, az alagútáram erősítője egy nagyon vékony arany vezetékkel van közvetlenül a tűhöz kötve. Továbbá, az eredetileg alkalmazott kerámia hordozót is fémre kellet cserélni a kapacitív csatolás további csökkentése érdekében Az így kialakított készülékkel a Si(1 1 1)–7×7 felületen végeztünk helyspecifikus atomi erő/alagútáram spektroszkópiát és kitűnő egyezést találtunk a már publikált spektrumokkal, amelyek még optikai elhajlás mérésével nyertek, tehát az áthallás eredendően zérus. Továbbá jól reprodukálható volt az alagútáram ugrásszerű csökkenése, amit a kovalens kötés kialakulása okoz a tű és a minta között [175].

Bibliography

[1] G. A. Somorjai and Y. Li, *Introduction to Surface Chemistry and Catalysis*, Wiley, 2, 2010.

[2] Y. Sugimoto, P. Pou, M. Abe, P. Jelinek, R. Perez, S. Morita, and O. Custance, *Nature* **446**, 64 (2007).

[3] L. Gross, F. Mohn, N. Moll, G. Meyer, R. Ebel, W. M. Abdel-Mageed, and M. Jaspars, *Nature Chemistry* **2**, 821 (2010).

[4] U. Diebold, *Surface Science Reports* **48**, 53 (2003).

[5] Q. Fu and T. Wagner, *Surface Science Reports* **62**, 431 (2007).

[6] M. B. Wijesundara and R. Azevedo, *Silicon Carbide Microsystems for Harsh Environments*, Springer-Verlag New York, 1 edition, 2011.

[7] R. M. Feenstra and C. E. C. Wood, *Porous Silicon Carbide and Gallium Nitride: Epitaxy, Catalysis, and Biotechnology Applications*, Wiley, 1 edition, 2008.

[8] F. Giessibl, *Appl Phys Lett* **74**, 4070 (1999).

[9] G. Binnig, H. Rohrer, C. Gerber, and E. Weibel, *Appl Phys Lett* **40**, 178 (1982).

[10] G. Binnig, H. Rohrer, C. Gerber, and E. Weibel, *Phys. Rev. Lett.* **49**, 57 (1982).

[11] G. Binnig and H. Rohrer, *Angewandte Chemie International Edition in English* **26**, 606 (1987).

[12] C. Chen, *Introduction to scanning tunneling microscopy*, Monographs on the physics and chemistry of materials, Oxford University Press, 2008.

[13] G. Binnig and H. Rohrer, *Surface Science* **126**, 236 (1983).

[14] M. Okano, K. Kajimura, S. Wakiyama, F. Sakai, W. Mizutani, and M. Ono, *Journal of Vacuum Science & Technology A: Vacuum, Surfaces, and Films* **5**, 3313 (1987).

[15] J. Lindahl, T. Takanen, and L. Montelius, *Journal of Vacuum Science & Technology B: Microelectronics and Nanometer Structures* **16**, 3077 (1998).

[16] F. Giessibl, F. Pielmeier, T. Eguchi, T. An, and Y. Hasegawa, *Physical Review B* **84**, 125409 (2011).

[17] A. K. Geim, *Angewandte Chemie International Edition* **50**, 2 (2010).

[18] J. Soler, A. Baro, N. Garcia, and H. Rohrer, *Phys. Rev. Lett.* **57**, 444 (1986).

[19] G. Binnig, C. Quate, and C. Gerber, *Phys. Rev. Lett.* **56**, 930 (1986).

[20] G. Meyer and N. Amer, *Appl Phys Lett* **53**, 2400 (1988).

[21] A. den Boef, *Appl Phys Lett* **55**, 439 (1989).

[22] T. Albrecht, P. Grutter, D. Horne, and D. Rugarl, *J. Appl. Phys.* **69**, 668 (1991).

[23] F. Giessibl, *Science* **267**, 68 (1995).

[24] S. Morita, R. Wiesendanger, and E. Meyer, *Noncontact Atomic Force Microscopy*, volume 1, Springer, 2002.

[25] S. Morita, F. J. Giessibl, and R. Wiesendanger, *Atomic Force Microscopy*, volume 2, Springer, 2009.

[26] F. Giessibl, *Physical Review B* **56**, 16010 (1997).

[27] F. Giessibl, *Applied Physics Letters* **78**, 123 (2001).

[28] J. Sader and S. Jarvis, *Appl Phys Lett* **84**, 1801 (2004).

[29] F. Giessibl, H. Bielefeldt, S. Hembacher, and J. Mannhart, *Appl Surf Sci* **140**, 352 (1999).

[30] R. Garcia and R. Perez, *Surf Sci Rep* **47**, 197 (2002).

[31] F. Giessibl, S. Hembacher, M. Herz, C. Schiller, and J. Mannhart, *Nanotechnology* **15**, S79 (2004).

[32] F. Giessibl, *Rev. Mod. Phys.* **75**, 949 (2003).

[33] F. Giessibl, *Appl Phys Lett* **76**, 1470 (2000).

[34] T. An, T. Eguchi, K. Akiyama, and Y. Hasegawa, *Applied Physics Letters* **87**, 133114 (2005).

[35] T. An, T. Nishio, T. Eguchi, M. Ono, A. Nomura, K. Akiyama, and Y. Hasegawa, *Rev Sci Instrum* **79**, 033703 (2008).

[36] B. Albers, M. Liebmann, T. Schwendemann, M. Baykara, M. Heyde, M. Salmeron, E. Altman, and U. Schwarz, *Review Of Scientific Instruments* **79**, 033704 (2008).

[37] J. C. Vickerman and I. Gilmore, *Surface Analysis*, The Principal Techniques, Wiley, 2011.

[38] X.-Q. Gong, A. Selloni, M. Batzill, and U. Diebold, *Nat Mater* **5**, 665 (2006).

[39] U. Diebold, N. Ruzycki, G. Herman, and A. Selloni, *Catalysis today* **85**, 93 (2003).

[40] Y. Guo, Y. Hu, W. Sigle, and J. Maier, *Advanced Materials* **19**, 2087 (2007).

[41] Z. Zhang, Q. Ge, S. Li, B. Kay, J. White, and Z. Dohnálek, *Phys. Rev. Lett.* **99**, 126105 (2007).

[42] R. Schaub, E. Wahlström, A. Rønnau, E. Lægsgaard, I. Stensgaard, and F. Besenbacher, *Science* **299**, 377 (2003).

[43] C. Sánchez-Sánchez, C. González, P. Jelinek, J. Méndez, P. de Andres, J. Martín-Gago, and M. López, *Nanotechnology* **21**, 405702 (2010).

[44] S. Wendt, R. Schaub, J. Matthiesen, E. Vestergaard, E. Wahlstrom, M. Rasmussen, P. Thostrup, L. Molina, E. Lægsgaard, and I. Stensgaard, *Surface Science* **598**, 226 (2005).

[45] O. Bikondoa, C. L. Pang, R. Ithnin, C. A. Muryn, H. Onishi, and G. Thornton, *Nature Materials 5, 189 - 192 (2006)* **5**, 189 (2006).

[46] Z. Zhang, O. Bondarchuk, B. Kay, J. White, and Z. Dohnalek, *The Journal of Physical Chemistry B* **110**, 21840 (2006).

[47] D. Matthey, J. Wang, S. Wendt, J. Matthiesen, R. Schaub, E. Lægsgaard, B. Hammer, and F. Besenbacher, *Science* **315**, 1692 (2007).

[48] E. Yagi, R. Hasiguti, and M. Aono, *Physical Review B* **54**, 7945 (1996).

[49] C. Yim, C. Pang, and G. Thornton, *Phys. Rev. Lett.* **104**, 36806 (2010).

[50] U. Diebold, J. Anderson, K. Ng, and D. Vanderbilt, *Phys. Rev. Lett.* **77**, 1322 (1996).

[51] K. Ng and D. Vanderbilt, *Physical Review B* **56**, 10544 (1997).

[52] U. Diebold, J. Lehman, T. Mahmoud, M. Kuhn, G. Leonardelli, W. Hebenstreit, M. Schmid, and P. Varga, *Surface Science* **411**, 137 (1998).

[53] O. Bikondoa, C. Pang, R. Ithnin, C. Muryn, H. Onishi, and G. Thornton, *Nat Mater* **5**, 189 (2006).

[54] R. Schaub, P. Thostrup, N. Lopez, E. Lægsgaard, I. Stensgaard, J. Nørskov, and F. Besenbacher, *Phys. Rev. Lett.* **87** (2001).

[55] G. Enevoldsen, H. Pinto, A. Foster, M. Jensen, A. Kühnle, M. Reichling, W. Hofer, J. Lauritsen, and F. Besenbacher, *Physical Review B* **78**, 045416 (2008).

[56] H. Pinto, G. Enevoldsen, F. Besenbacher, J. Lauritsen, and A. Foster, *Nanotechnology* **20**, 264020 (2009).

[57] G. Enevoldsen, H. Pinto, A. Foster, M. Jensen, W. Hofer, B. Hammer, J. Lauritsen, and F. Besenbacher, *Phys. Rev. Lett.* **102**, 136103 (2009).

[58] Y. He, O. Dulub, H. Cheng, A. Selloni, and U. Diebold, *Phys. Rev. Lett.* **102**, 106105 (2009).

[59] Y. He, A. Tilocca, O. Dulub, A. Selloni, and U. Diebold, *Nature Materials* **8**, 585 (2009).

[60] P. Møller and M. Wu, *Surface Science* **224**, 265 (1989).

[61] H. Onishi and Y. Iwasawa, *Surface science* **313**, L783 (1994).

[62] P. Murray, N. Condon, and G. Thornton, *Physical Review B* **51**, 10989 (1995).

[63] H. Onishi and Y. Iwasawa, *Phys. Rev. Lett.* **76**, 791 (1996).

[64] Q. Guo, I. Cocks, and E. Williams, *Phys. Rev. Lett.* **77**, 3851 (1996).

[65] C. Pang, S. Haycock, H. Raza, P. Murray, G. Thornton, O. Gülseren, R. James, and D. Bullett, *Phys. Rev. B* **58**, 1586 (1998).

[66] R. Bennett, P. Stone, N. Price, and M. Bowker, *Phys. Rev. Lett.* **82**, 3831 (1999).

[67] E. Asari and R. Souda, *Phys. Rev. B* **60**, 10719 (1999).

[68] C. Pang, H. Raza, S. Haycock, and G. Thornton, *Applied surface science* **157**, 233 (2000).

[69] S. Elliott and S. Bates, *Phys. Rev. B* **65**, 245415 (2002).

[70] U. Diebold, *Applied Physics A: Materials Science & Processing* **76**, 681 (2003).

[71] S. Elliott and S. Bates, *Phys. Rev. B* **67**, 035421 (2003).

[72] M. Blanco-Rey, J. Abad, C. Rogero, J. Mendez, M. Lopez, J. Martin-Gago, and P. de Andres, *Phys. Rev. Lett.* **96**, 55502 (2006).

[73] K. Park, M. Pan, V. Meunier, and E. Plummer, *Phys. Rev. Lett.* **96**, 226105 (2006).

[74] M. Blanco-Rey, J. Abad, C. Rogero, J. Méndez, M. López, E. Román, J. Martín-Gago, and P. de Andrés, *Phys. Rev. B* **75**, 081402 (2007).

[75] N. Shibata, A. Goto, S. Choi, T. Mizoguchi, S. Findlay, T. Yamamoto, and Y. Ikuhara, *Science* **322**, 570 (2008).

[76] P. Batson, N. Dellby, and O. Krivanek, *Nature* **418**, 617 (2002).

[77] S. J. Tauster, S. C. Fung, R. T. K. Baker, and J. A. Horsley, *Scinece* **211**, 1121 (1981).

[78] C. Campbell, *Surface Science Reports* **27**, 1 (1997).

[79] J. Nakamura, J. Rodriguez, and C. Campbell, *Journal of Physics-Condensed Matter* **1**, SB149 (1989).

[80] S. Tauster and S. Fung, *Journal of Catalysis* **55**, 29 (1978).

[81] A. Berkó, I. Ulrych, and K. C. Prince, *The Journal of Physical Chemistry B* **102**, 3379 (1998).

[82] M. Bowker, P. Stone, R. Bennett, and N. Perkins, *Surface Science* **497**, 155 (2002).

[83] F. Pesty, H. Steinrück, and T. Madey, *Surface Science* **339**, 83 (1995).

[84] K. Williams, M. Salmeron, A. Bell, and G. Somorjai, *Surface Science* **204**, L745 (1988).

[85] M. Bowker, P. Stone, P. Morrall, R. Smith, R. Bennett, N. Perkins, R. Kvon, C. Pang, E. Fourre, and M. Hall, *Journal of Catalysis* **234**, 172 (2005).

[86] D. Jennison, O. Dulub, W. Hebenstreit, and U. Diebold, *Surface Science* **492**, L677 (2001).

[87] O. Dulub, W. Hebenstreit, and U. Diebold, *Physical Review Letters* **84**, 3646 (2000).

[88] Y. N. Sun, Z. Qin, M. Lewandowski, E. Carrasco, M. Sterrer, S. Shaikhutdinov, and H. J. Freund, *Journal of Catalysis* **266**, 359 (2009).

[89] S. Chambers, *Surface Science Reports* **39**, 105 (2000).

[90] A. Boffa, H. Galloway, P. Jacobs, J. Benítez, J. Batteas, M. Salmeron, A. Bell, and G. Somorjai, *Surface Science* **326**, 80 (1995).

[91] G. Barcaro, F. Sedona, A. fortunelli, and G. Granozzi, *Journal of Physical Chemistry C* **111**, 6095 (2007).

[92] F. Sedona, G. Rizzi, S. Agnoli, F. i Xamena, A. Papageorgiou, D. Ostermann, M. Sambi, P. Finetti, K. Schierbaum, and G. Granozzi, *The Journal of Physical Chemistry B* **109**, 24411 (2005).

[93] P. Finetti, F. Sedona, G. A. Rizzi, U. Mick, F. Sutara, M. Svec, V. Matolin, K. Schierbaum, and G. Granozzi, *The Journal of Physical Chemistry C* **111**, 869 (2007).

[94] Y. Zhang, L. Giordano, G. Pacchioni, A. Vittadini, F. Sedona, P. Finetti, and G. Granozzi, *Surface Science* **601**, 3488 (2007).

[95] T. Orzali, M. Casarin, G. Granozzi, M. Sambi, and A. Vittadini, *Physical Review Letters* **97**, 156101 (2006).

[96] T. Matsumoto, M. Batzill, S. Hsieh, and B. Koel, *Surface Science* **572**, 127 (2004).

[97] T. Matsumoto, M. Batzill, S. Hsieh, and B. Koel, *Surface Science* **572**, 146 (2004).

[98] D. Rosenthal, I. Zizak, N. Darowski, T. Magkoev, and K. Christmann, *Surface Science* **600**, 2830 (2006).

[99] T. Maeda, Y. Kobayashi, and K. Kishi, *Surface Science* **436**, 249 (1999).

[100] T. Ashworth and G. Thornton, *Thin Solid Films* **400**, 43 (2001).

[101] T. Ashworth, C. Muryn, and G. Thornton, *Nanotechnology* **16**, 3041 (2005).

[102] Z. Chang and G. Thornton, *Surface Science* **462**, 68 (2000).

[103] A. Atrei, U. Bardi, and G. Rovida, *Surface Science* **391**, 216 (1997).

[104] J. Biener, E. Farfan-Arribas, M. Biener, C. Friend, and R. Madix, *Journal of Chemical Physics* **123**, 1 (2005).

[105] M. Chen and D. Goodman, *Science* **306**, 252 (2004).

[106] M. Chen, W. Wallace, D. Kumar, Z. Yan, K. Gath, Y. Cai, Y. Kuroda, and D. Goodman, *Surface Science* **581**, 115 (2005).

[107] W. Oh, C. Xu, D. Kim, and D. Goodman, *Journal of Vacuum Science & Technology A: Vacuum, Surfaces, and Films* **15**, 1710 (1997).

[108] Q. Guo, W. Oh, and D. Goodman, *Surface Science* **437**, 49 (1999).

[109] G. Herman, M. Gallagher, S. Joyce, and C. Peden, *Journal of Vacuum Science & Technology B: Microelectronics and Nanometer Structures* **14**, 1126 (1996).

[110] R. Bennett and N. McCavish, *Topics in Catalysis* **36**, 11 (2005).

[111] N. McCavish and R. Bennett, *Surface Science* **546**, 47 (2003).

[112] H. Freund and M. Roberts, *Surface Science Reports* **25**, 225 (1996).

[113] G. Gusmano, A. Bianco, G. Montesperelli, and E. Traversa, *Electrochimica acta* **41**, 1359 (1996).

[114] F. Bechstedt and M. Scheffler, *Surface Science Reports* **18**, 145 (1993).

[115] A. M. Kiss, M.Š vec, and A. Berkó, *Surface Science* **600**, 3352 (2006).

[116] M. Haruta, *Catalysis Today* **36**, 153 (1997).

[117] M. Schubert, S. Hackenberg, A. van Veen, M. Muhler, V. Plzak, and R. Behm, *Journal of Catalysis* **197**, 113 (2001).

[118] T. Bredow, E. Apra, M. Catti, and G. Pacchioni, *Surface Science* **418**, 150 (1998).

[119] M. A. San Miguel, C. J. Calzado, and J. F. Sanz, *The Journal of Physical Chemistry B* **105**, 1794 (2001).

[120] P. Hardman, R. Casanova, P. K, C. A. Muryn, P. Wincott, and G. Thornton, *Surface Science* **269**, 677 (1992).

[121] K. Prabhakaran, D. Purdie, R. Casanova, C. A. Muryn, P. Hardman, P. Wincott, and G. Thornton, *Physical Review B* **45**, 6969 (1992).

[122] R. Heise and R. Courths, *Surface Science* **331**, 1460 (1995).

[123] A. G. Thomas, P. J. Hardman, C. A. Muryn, H. S. Dhariwal, A. F. Prime, G. Thornton, E. Roman, and J. L. de Segovia, *J. Chem. Soc., Faraday Trans.* **91**, (1995).

[124] R. Lindsay, E. Michelangeli, B. Daniels, M. Polcik, A. Verdini, L. Floreano, A. Morgante, J. Muscat, N. Harrison, and G. Thornton, *Surface Science* **547**, L859 (2003).

[125] R. Lindsay, E. Michelangeli, B. Daniels, M. Polcik, A. Verdini, L. Floreano, A. Morgante, and G. Thornton, *Surface Science* **566**, 921 (2004).

[126] C. Pang, C. Muryn, A. Woodhead, H. Raza, S. Haycock, V. Dhanak, and G. Thornton, *Surface Science* **583**, L147 (2005).

[127] S. Krischok, J. Gunster, D. Goodman, O. Hofft, and V. Kempter, *Surface And Interface Analysis* **37**, 77 (2005).

[128] J. Muscat, N. Harrison, and G. Thornton, *Physical Review B* **59**, 15457 (1999).

[129] B. Hayden and G. Nicholson, *Surface Science* **274**, 277 (1992).

[130] A. Grant and C. Campbell, *Physical Review B* **55**, 1844 (1997).

[131] R. E. Schlier and H. E. Farnsworth, *The Journal of Chemical Physics* **30**, 917 (1959).

[132] K. Takayanagi, Y. Tanishiro, M. Takahashi, and S. Takahashi, *Journal of Vacuum Science & Technology A: Vacuum, Surfaces, and Films* **3**, 1502 (1985).

[133] K. Takayanagi, Y. Tanishiro, M. Takahashi, and S. Takahashi, *Surface Science* **164**, 367 (1985).

[134] M. Weinelt, W. Huber, P. Zebisch, H. Steinrück, B. Reichert, U. Birkenheuer, and N. Rösch, *Physical Review B* **46**, 1675 (1992).

[135] H. Steinrück, *Applied Physics A: Materials Science & Processing* **59**, 517 (1994).

[136] W. Widdra, A. Fink, S. Gokhale, P. Trischberger, D. Menzel, U. Birkenheuer, U. Gutdeutsch, and N. Rosch, *Physical Review Letters* **80**, 4269 (1998).

[137] U. Birkenheuer, U. Gutdeutsch, N. Rösch, A. Fink, S. Gokhale, D. Menzel, P. Trischberger, and W. Widdra, *The Journal of Chemical Physics* **108**, 9868 (1998).

[138] F. Rochet, F. Jolly, F. Bournel, G. Dufour, F. Sirotti, and J. Cantin, *Physical Review B* **58**, 11029 (1998).

[139] H. Yeom, S. Baek, J. Kim, H. Lee, and H. Koh, *Physical Review B* **66**, 115308 (2002).

[140] P. Klimesch, G. Meyer, and M. Henzler, *Surface Science* **137**, 79 (1984).

[141] J. Yoshinobu, D. Fukushi, M. Uda, E. Nomura, and M. Aono, *Physical review. B, Condensed matter* **46**, 9520 (1992).

[142] M. Piancastelli, N. Motta, A. Sgarlata, A. Balzarotti, and M. Crescenzi, *Physical review. B* **48**, 17892 (1993).

[143] J. Yoshinobu, H. Tsuda, M. Onchi, and M. Nishijima, *Solid state communications* **60**, 801 (1986).

[144] M. Carbone, R. Zanoni, M. Piancastelli, G. Comtet, G. Dujardin, L. Hellner, and A. Mayne, *Journal Of Electron Spectroscopy And Related Phenomena* **76**, 271 (1995).

[145] J. Kim, T. Kampen, K. Horn, and M. Jung, *Surface Science* **601**, 694 (2007).

[146] C. Sbraccia, C. Pignedoli, A. Catellani, R. Di Felice, P. Silvestrelli, F. Toigo, F. Ancilotto, and C. Bertoni, *Surface Science* **557**, 80 (2004).

[147] X. Lu, X. Wang, Q. Yuan, and Q. Zhang, *Journal of the American Chemical Society* **125**, 7923 (2003).

[148] B. L. Rogers, J. G. Shapter, W. M. Skinner, and K. Gascoigne, *Review Of Scientific Instruments* **71**, 1702 (2000).

[149] E. Wutscher and F. J. Giessibl, *Rev Sci Instrum* **82**, 093703 (2011).

[150] J. E. Sader and Y. Sugimoto, *Appl Phys Lett* **97**, 043502 (2010).

[151] *http://www.ti.com/tina-ti* .

[152] *Electronics*, General Cable, http://catalog.proemags.com/publication/cd728f6b, 2010.

[153] T. Hayes and P. Horowitz, *Student Manual for The Art of Electronics*, Cambridge University Press, 1989.

[154] L. Gross, F. Mohn, N. Moll, P. Liljeroth, and G. Meyer, *Science* **325**, 1110 (2009).

[155] M. Heyde, M. Sterrer, H. P. Rust, and H. J. Freund, *Applied Physics Letters* **87**, 083104 (2005).

[156] G. Herman and C. Peden, *Colloids and Surfaces a-Physicochemical and Engineering Aspects* **154**, 187 (1999).

[157] M. Henderson, *Surface Science* **419**, 174 (1999).

[158] A. Berkó and F. Solymosi, *Surface Science* **400**, 281 (1998).

[159] A. Berkó, J. Szökő, and F. Solymosi, *Solid state ionics* **141**, 197 (2001).

[160] A. Berkó, O. Hakkel, J. Szökő, and F. Solymosi, **643**, 643 (2002).

[161] S. Bernal, F. J. Botana, J. Calvino, C. López, J. Pérez-Omil, and J. Rodríguez-Izquierdo, *Journal of the Chemical Society - Faraday Transactions* **92**, 2799 (1996).

[162] J. He, R. K. Behera, M. W. Finnis, X. Li, E. C. Dickey, S. R. Phillpot, and S. B. Sinnott, *Acta Materialia* **55**, 4325 (2007).

[163] H. Huntington and G. Sullivan, *Physical Review Letters* **14**, 177 (1965).

[164] A. Berkó, T. Biro, T. Kecskes, and F. Solymosi, *Vacuum* **61**, 317 (2001).

[165] F. Solymosi, *Journal of Catalysis* **94**, 581 (1985).

[166] L. Zhang, J. van Ek, and U. Diebold, *Physical Review B* **59**, 5837 (1999).

[167] J. Schoiswohl, M. Sock, S. Eck, S. Surnev, M. Ramsey, F. Netzer, and G. Kresse, *Physical Review B* **69**, (2004).

[168] J. Schoiswohl, S. Surnev, M. Sock, S. Eck, M. Ramsey, F. Netzer, and G. Kresse, *Physical Review B* **71**, 165437 (2005).

[169] I. Mauch, G. Kaindl, and A. Bauer, *Surface Science* **522**, 27 (2003).

[170] A. Männig, Z. Zhao, D. Rosenthal, K. Christmann, H. Hoster, H. Rauscher, and R. J. Behm, *Surface Science* **576**, 29 (2005).

[171] R. Pérez, I.Š tich, M. Payne, and K. Terakura, *Phys. Rev. B* **58**, 10835 (1998).

[172] M. Lantz, H. Hug, R. Hoffmann, P. van Schendel, P. Kappenberger, S. Martin, A. Baratoff, and H.-J. Guntherodt, *Science* **291**, 2580 (2001).

[173] Y. Sugimoto, P. Pou, O. Custance, P. Jelinek, S. Morita, R. Perez, and M. Abe, *Phys. Rev. B* **73**, 205329 (2006).

[174] P. Jelinek, M. Ondráček, and F. Flores, *J. Cond. Matt. Phys.* (accepted).

[175] P. Jelínek, M.Š vec, P. Pou, R. Perez, and V. Cháb, *Phys. Rev. Lett.* **101**, 176101 (2008).

[176] D. Sawada, Y. Sugimoto, K.-I. Morita, M. Abe, and S. Morita, *Appl Phys Lett* **94**, 173117 (2009).

[177] M. Ternes, C. González, C. Lutz, P. Hapala, F. Giessibl, P. Jelinek, and A. Heinrich, *Phys. Rev. Lett.* **106**, 016802 (2011).

[178] C. Loppacher, M. Bammerlin, M. Guggisberg, S. Schar, R. Bennewitz, A. Baratoff, E. Meyer, and H.-J. Guntherodt, *Phys. Rev. B* **62**, 16944 (2000).

[179] R. Hoffmann, M. Lantz, H. Hug, P. van Schendel, P. Kappenberger, S. Martin, A. Baratoff, and H.-J. Guntherodt, *Phys. Rev. B* **67**, 085402 (2003).

[180] R. Garcia, C. Gómez, N. Martinez, S. Patil, C. Dietz, and R. Magerle, *Phys. Rev. Lett.* **97**, 016103 (2006).

[181] L. Kantorovich and T. Trevethan, *Phys. Rev. Lett.* **93**, 236102 (2003).

[182] S. Ghasemi, S. Goedecker, A. Baratoff, T. Lenosky, E. Meyer, and H. Hug, *Phys. Rev. Lett.* **100**, 236106 (2008).

[183] N. Oyabu, P. Pou, Y. Sugimoto, P. Jelinek, M. Abe, S. Morita, R. Perez, and O. Custance, *Phys. Rev. Lett.* **96**, 106101 (2006).

[184] W. Kaminski and R. Perez, *Tribology Letters* **3**, 295 (2010).

[185] L. Cockins, Y. Miyahara, S. Bennett, A. Clerk, S. Studenikin, P. Poole, A. Sachrajda, and P. Grutter, *PNAS* **107**, 9496 (2010).

[186] M. Kisiel, E. Gnecco, U. Gysin, L. Marot, S. Rast, and E. Meyer, *Nature Materials* **10**, 119 (2011).

[187] A. Labuda, Y. Miyahara, L. Cockins, and P. Grütter, *Physical Review B* **84**, 125433 (2011).

[188] A. Weymouth, T. Wutscher, J. Welker, T. Hofmann, and F. Giessibl, *Phys. Rev. Lett.* **106**, 226801 (2011).

[189] R. H. Miwa, A. J. Weymouth, A. B. McLean, and G. P. Srivastava, *Physical Review B* **80**, 115317 (2009).

[190] D. Brown, D. Moffatt, and R. Wolkow, *Science* **279**, 542 (1998).

[191] A. J. Weymouth, R. H. Miwa, G. P. Srivastava, and A. B. McLean, *physica status solidi (c)* **7**, 240 (2010).

[192] L. Gross, F. Mohn, N. Moll, P. Liljeroth, and G. Meyer, *Science* **325**, 1110 (2009).

[193] I. Barke, F. Zheng, A. Konicek, R. Hatch, and F. Himpsel, *Physical Review Letters* **96**, 216801 (2006).

[194] R. Uhrberg, T. Kaurila, and Y. Chao, *Physical Review B* **58**, 1730 (1998).

[195] M.Š vec, P. Mutombo, P. Shukrinov, V. Dudr, and V. Cháb, *Nanotechnology* **17**, 213 (2006).

[196] R. Hamers, R. Tromp, and J. Demuth, *Physical Review Letters* **56**, 1972 (1986).

[197] R. Wolkow and P. Avouris, *Physical Review Letters* **60**, 1049 (1988).

[198] B. Kempgens, H. Köppel, A. Kivimäki, M. Neeb, L. Cederbaum, and A. Bradshaw, *Physical Review Letters* **79**, 3617 (1997).

[199] J. Andersen, A. Beutler, S. Sorensen, R. Nyholm, B. Setlik, and D. Heskett, *Chemical Physics Letters* **269**, 371 (1997).

[200] R. Hunger, R. Fritsche, B. Jaeckel, W. Jaegermann, L. Webb, and N. Lewis, *Physical Review B* **72**, 045317 (2005).

[201] G. Le Lay, M. Göthelid, T. Grehk, M. Björkquist, U. Karlsson, and V. Aristov, *Physical Review B* **50**, 14277 (1994).

[202] C. Karlsson, E. Landemark, Y. Chao, and R. Uhrberg, *Physical review. B, Condensed matter* **50**, 5767 (1994).

[203] J. Terry, M. Linford, C. Wigren, R. Cao, P. Pianetta, and C. Chidsey, *Journal Of Applied Physics* **85**, 213 (1999).

[204] F. Yang, R. Hunger, K. Roodenko, K. Hinrichs, K. Rademann, and J. Rappich, *Langmuir* **25**, 9313 (2009).

[205] A. Berkó, N. Balázs, G. Kassab, and L. Óvári, *Journal of Catalysis* **289**, 179 (2012).